

Micromachined Devices for an Airborne Bio-Particle Analysis System

Thesis by
Amish S. Desai

In Partial Fulfillment of the Requirements
for the Degree of Doctor of Philosophy



California Institute of Technology
Pasadena, California
2000

(September 15, 1999)

© 2000

Amish Desai

All Rights Reserved

To my parents

Acknowledgements

Just to be here in Los Angeles, United States of America, writing the acknowledgements of my Caltech thesis after a morning of surfing is a dream in itself. To many this scene might not amount to much. But this moment is a reality, only because of my parents who crossed the globe to give me an opportunity to make something like this come true. I can never be thankful enough for their hard work.

I would like to thank Dr. Yu-Chong Tai who has taught me much more than just micromachining, and made me worthy of a Caltech Ph.D. This amazing career path could not have been possible were it not for Dr. Chih-Ming Ho at UCLA, who opened a young undergraduate's eyes to the world of micromachining. Thanks to Dr. Denny Miu for that first year at the Caltech Micromachining Lab, and connecting me up with one of the most intense and amazing professors at Caltech – Dr. Tai. I'm grateful to Raanan, JAWS, Ceca, Xing, Tom -- the "senior guys" who taught me how to process, saved me from fatal mistakes, and tolerated my jokes. More specifically, the various parts of my thesis could not have been done without insight and help of Dr. Dirk Bökenkamp(dive buddy for life), Dr. Stephen Mayo, Xing Yang, Dr. Terry Lee and Mike Davis at the City of Hope, and Dr. Sang-Wook Lee. I can't forget Trevor Roper, who is the only guy that I know, who knows how to fix it all – from sputtering machines to Volvos. A special thanks to XQ, "Parylene master," who made the mass spec nozzle a true success, and always had time to help and advise.

And then there those who are behind the scenes who are not mentioned in any papers, presentations, or anything tangible: Guido--for convincing me to stay with the program, Jenny, Viki, Marc B., Marc R., and Chase-- for having more confidence in me than I had in myself, Guido and Veronique – for things that words can't express, for always being there, and for the good times in our future, Wen – for keeping me "flying high," and always looking out for me. Thanks to my sister, Ratna, for being my best and worst critic, and for adding the final awarding winning touches on some of my hardest tasks. And a final "cheers" to all the "Euros" at Caltech for making memories and friendships spanning oceans and continents.

Micromachined Devices for an Airborne Bio-Particle Analysis System

Thesis by
Amish S. Desai

In Partial Fulfillment of the Requirements
For the Degree of
Doctor of Philosophy

Abstract

The goal of this thesis is to develop micromachined devices for an automated miniaturized airborne bio-particle analysis system. The realization of such a system is complex requiring a particle capture, transport, collection, sample preparation, and analysis. Accordingly, microelectromechanical systems (MEMS) teams have studied and developed micro-pumps, valves, channels as building blocks for a miniature chemical analysis system. In this thesis, novel micromachined solutions to some of these tasks are presented. Specifically, the development of:

- 1) a low voltage, air-based electrostatic particle transportation system,
- 2) an air-to-liquid interface design for transport of airborne particles into a liquid environment
- 3) a micro-chip electrospray (ES) mass spectrometer interface for small volume (nL) mass spectrometry,
- 4) and fast mixers ($<100\mu\text{s}$) for the study of chemical reaction kinetics.

The particle transport system consists of 3-phase electrode arrays covered by photoresist and Teflon. Extensive testing of this system has been done using a variety of insulation materials, thicknesses (0-12 μm), particle sizes (1-10 μm), particle materials (metal, glass, polystyrene, spores, etc.), waveforms, frequencies, and voltages. Although previous

literature claimed it impractical to electrostatically transport particles with sizes of 5-10 μm due to complex surface forces, this effort actually demonstrates 90% transportation efficiencies with the optimal combination of insulation thickness, electrode geometry, and insulation material.

As the second step, this particle transportation technology has also been integrated with an active micromachined filter and an air-to-liquid silicone rubber interface. Two methods of air to liquid particle transport were explored – moving particles across a stationary fluid meniscus and the other, moving meniscus across stationary particles.

Third, the development of a micron-sized MEMS nozzle (1-3 μm orifice diameters) is presented with successful demonstration of its application for electrospray ionization mass spectroscopy. MEMS scaling issues were verified with the flow visualization of the Taylor Cone on this nozzle.

Fourth, a 1cm x 1cm x 1mm DRIE silicon mixer capable of initiating and quenching (starting and stopping) chemical reactions in intervals as short as 100 μs was characterized by employing two carefully chosen chemical reactions with reaction time constants of 3 ms and 9 ms along with visualization techniques using dyes and acid-base indicators.

Table of Contents

Chapter 1: MEMS and Bio-Particle Detection

1.1 Introduction	1
1.2 Micro Electro Mechanical Systems (MEMS)	2
1.3 Airborne Sampling and MEMS.....	5
1.4 The Purpose and Organization of this Thesis.....	7

Chapter 2: Particle Transportation Fundamentals

2.1 Introduction	1
2.2 Particle Adhesion Forces in Air	2
2.2.1 Van der Waals Forces	3
2.2.2 Coulombic Forces	5
2.2.3 Meniscus Force	7
2.3 Dielectrophoretic Force for Particle Transportation	8
2.4 Conclusion.....	12

Chapter 3: The Particle Transportation Chip

3.1 Introduction	1
3.2 1st Generation Fabrication	1
3.3 First Generation Designs.....	3
3.4 Experimental Setup and Testing	4
3.4.1 Various Three Phase Waveforms	9
3.4.2 Surface Silanization Treatment	9
3.4.3 Substrate Heating	10
3.4.4 Surface Metallization	11
3.4.5 Mechanical Vibration.....	11
3.4.6 Plasma Roughening.....	12
3.4.7 Dielectric Cycling and Aging Effects	13

3.4.8 Photoresist as an Insulation Layer.....	14
3.5 2nd Generation Fabrication.....	15
3.6 Spin on Teflon as an Insulation Layer	16
3.7 Simulation of the DEP Force	21
3.8 Discussion	27
3.9 Conclusion.....	30

Chapter 4: Particle Collection from Air to Liquid

4.1 Introduction	1
4.2 First Generation Interface Design	2
4.3 First Generation Interface Chip Fabrication.....	5
4.4 First Generation Interface Experiments and Discussion	8
4.5 Second Generation Interface Design.....	10
4.6 Silicone Elastomer – Sylgard® 184	12
4.7 Second Generation Interface Fabrication.....	14
4.8 Second Generation Experiments	15
4.9 Conclusion.....	16

Chapter 5: Electrospray Fundamentals

5.1 Introduction	1
5.2 Mass Spectrometry Overview	2
5.3 Micro-Electrospray Ionization Fundamentals.....	5
5.4 MEMS for ESI?.....	10
5.5 Conclusion.....	12

Chapter 6: First Generation Silicon Nitride Nozzles

6.1 Introduction	1
6.2 Design Requirements	1
6.3 Fabrication.....	3
6.4 Testing and Results	7
6.5 1st Generation Problems	9

Chapter 7: Second Generation Silicon Nitride Nozzles

7.1 Introduction	1
7.2 2nd Generation Nozzle Design	1
7.3 2nd Generation Nozzle Fabrication.....	5
7.4 2nd Generation Fabrication Issues	7
7.5 3rd Generation Nozzle Design and Fabrication	11
7.6 Taylor Cone Visualization	13
7.7 Electrostatic Simulation	17
7.8 Conclusion.....	19

Chapter 8: Fast Mixers for Reaction Kinetics

8.1 Introduction	1
8.2 Past Mixers.....	2
8.3 Design, Fabrication, and Experiments	4
8.4 Chemical Calibration Method and Theory.....	8
8.4.1 Experimental Procedure - DNPA.....	10
8.4.2 DNPA Results	12
8.4.3 PCA Reaction For Faster Kinetics	13
8.4.4 Experimental Procedure - PCA.....	15
8.5 Flow Visualization	16
8.6 Further Optimization of the Mixer Chip	20
8.7 Conclusion.....	23

Chapter 9: Conclusion and Future Work

9-1

List of Figures

Chapter 1

Figure 1-1: Typical silicon anisotropic bulk etching profiles	3
Figure 1-2: Isotropic etching of silicon results in rounded features.....	3
Figure 1-3: Example of a surface micromachining fabrication sequence.....	5

Chapter 2

Figure 2-1: Method of summing interaction energy of particle	4
Figure 2-2: Image force between a charged particle near a conductor.	6
Figure 2-3: Polyvinyl chloride particles show increase in charge after	6
Figure 2-4: Model of capillary condensation of liquid between particle	7
Figure 2-5: Net force on a small dipole of strength $p=qd$ in a non-uniform field.....	8
Figure 2-6: Qualitative comparison of particle forces showing the performance.....	12

Chapter 3

Figure 3-1: Cross-sectional view of electrode chip.....	2
Figure 3-2: Key electrode process steps.....	3
Figure 3-3: Examples of radial and parallel electrode geometries.....	4
Figure 3-4: Example of three-phase waveform.....	4
Figure 3-5: Circuit for three phase rectangular waveform ($10-200V_{pp}$)	5
Figure 3-6: Particles before (left) applying waveform and then transported	6
Figure 3-7: Testing setup showing video, μ -scope, probe tips, and circuit	7
Figure 3-8: Top view of particle stuck in a pearl chain formation.....	8
Figure 3-9: Schematic of initial qualitative observations regarding relationship	8
Figure 3-10: Surface roughness effect on particle contact area.	12
Figure 3-11: Electrode structure with additional insulation to reduce image force.	14
Figure 3-12: Evidence of an optimal resist thickness	15
Figure 3-13: 2nd run of electrodes with $3\mu\text{m}$ width and different geometries	16

Figure 3-14: Transport efficiency vs. Teflon film thickness.....	18
Figure 3-15: Transport efficiency as a function of thickness and different frequencies...	19
Figure 3-16: The effect of increasing electrode spacing on transport efficiency (100V).	20
Figure 3-17: The effect of increasing electrode spacing on transport efficiency (160V).	20
Figure 3-18: DEP forces vs. particle position	22
Figure 3-19: DEP force decreases with increase in particle height from electrodes.....	23
Figure 3-20: 3-D simulation of particle DEP force.....	23
Figure 3-21: DEP force in Y-direction is reduced when electrode pitch is increased	24
Figure 3-22: DEP force in X-direction is reduced when electrode pitch is increased	25
Figure 3-23: Simulation of particle image force for various heights	26
Figure 3-24: DEP horizontal force increases with larger dielectric constant.....	27
Figure 3-25: DEP vertical force increases with larger dielectric constant.....	27
Figure 3-26: Schematic of particle forces	28
Figure 3-27: Decreasing pitch resulted in higher image force contribution.	29

Chapter 4

Figure 4-1: 1st Particle air to liquid collection scheme (L) and schematic (R)	2
Figure 4-2: Maximum meniscus pressures for water vs. interface channel radius.	4
Figure 4-3: Idealized flow rates possible for given interface channel sizes.....	5
Figure 4-4: Various glass interface channel designs.....	5
Figure 4-5: Glass interface channel fabrication steps.	6
Figure 4-6: 1cm x 1cm glass interface die bonded to a glass substrate for initial testing...	7
Figure 4-7: Glass interface die (R) bonded to a particle transportation chip (L).	8
Figure 4-8: DEP force in air not enough to cross liquid meniscus.	9
Figure 4-9: Particle collection experiment with a moving droplet.....	10
Figure 4-10: 2nd generation particle collection scheme	11
Figure 4-11: Integrated filter and particle transport layout (1cm x 1cm).....	11
Figure 4-12: PDMS crosslinking reaction.....	12
Figure 4-13: PDMS being released off the silicon wafer mold.....	13
Figure 4-14: PDMS Channel fabrication steps	13
Figure 4-15: Moving meniscus concept integrated with an active filter region.....	14

Figure 4-16: Video image of interface chip on radial transportation structure.	14
Figure 4-17: Snapshots of particles being captured from the air into the liquid meniscus	15
Figure 4-18: More particles moved near meniscus area with the radial design	15

Chapter 5

Figure 5-1: Parts of a mass spectrometry system.....	3
Figure 5-2: Typical electrospray configuration.....	5
Figure 5-3: The Taylor Cone.....	6
Figure 5-4: The liquid surface below threshold for cone generation [9].	7
Figure 5-5: At higher flow rates of spray, cone angle deviates from 49.3°.	8
Figure 5-6: Magnified view of cone region	9
Figure 5-7: Electrospray from a capillary	11
Figure 5-8: By careful manual packing, in-line filters are constructed.....	11

Chapter 6

Figure 6-1: Related work on microfabricated ESI devices	2
Figure 6-2: 1st generation nozzle design.....	3
Figure 6-3: Typical steps for micro-channel fabrication.....	4
Figure 6-4: 3-d view of ES Nozzle.....	5
Figure 6-5: Nozzle top view showing backside inlet hole and filter structures.	5
Figure 6-6: 1cm x 1cm die layout with overhanging ESI nozzles.	6
Figure 6-7: 1st generation major fabrication steps.....	6
Figure 6-8: SEM photograph.....	7
Figure 6-9: MS scan of Gramicidin S using MEMS nozzle	9
Figure 6-10: Backside inlet hole enlargement results in weak front wall.....	10
Figure 6-11: Formation of air bubble in backside inlet holes on wafer.	11
Figure 6-12: Picture of silicon nitride “tongue” at the nozzle outlet	11

Chapter 7

Figure 7-1: Polysilicon/oxide posts can be used to create flatter, stronger channel roofs..	2
Figure 7-2: Type 1- Short-slant-forward, maximum field concentration, 2×10^6 V/m	3

Figure 7-3: Type 2 – Short-slant-back, maximum field concentration, 4×10^6 V/m	4
Figure 7-4: Type 3 – Long, maximum field concentration, 5×10^6 V/m	4
Figure 7-5: 2nd generation modifications	5
Figure 7-6: Major fabrication steps for the polysilicon sacrificial layer process.....	6
Figure 7-7: 2nd generation nozzles	7
Figure 7-8: Detail of evaporated gold line over nozzle tip.	7
Figure 7-9: Same fabrication process resulted in two different	8
Figure 7-10: The “donuts” are boundaries of the post/filter structures.....	9
Figure 7-11: Flat silicon nitride channel roof achieved with ringed oxide posts.....	10
Figure 7-12: 1-2 μ m step causes discontinuity in evaporated gold line to tip.	10
Figure 7-13: 3rd generation MS nozzle with separation channel.....	11
Figure 7-14: Completed 3rd generation structure	12
Figure 7-15: Upward curling of nozzle structures due to stress gradients in silicon	12
Figure 7-16: Cracking due to stress in Si_xN_y micro-channels.....	13
Figure 7-17: Taylor Cone visualization set-up.....	14
Figure 7-18: Chip holder connected to XYZ stage for ESI visualization.	15
Figure 7-19: Video snapshots of formation of Taylor Cone.	16

Chapter 8

Figure 8-1: Mixer schematic	2
Figure 8-2: Schematic of the Berger Ball mixer developed in 1968 still used today.	3
Figure 8-3: Turbulent wake behind a sphere	3
Figure 8-4: Two mixers with delay lengths of 5.33mm (L) and 20.33mm (R).	5
Figure 8-5: Cleaved chip showing the seamless glass-Si anodic bond.....	6
Figure 8-6: Biologic machine with 1cm x 1cm mixer chip before clamping.	6
Figure 8-7: 3-D view of fabricated mixer chip	7
Figure 8-8: Mixer interface to Biologic machine (left) and close-up of chip	7
Figure 8-9: DNPA hydrolysis reaction	8
Figure 8-10: BioLogic and chip connection schematic.....	11
Figure 8-11: DNPA Absorbance vs. Time Plot.....	12
Figure 8-12: Linearized DNPA data	13

Figure 8-13: The new PCA hydrolysis reaction with 2.5ms time constant.....	14
Figure 8-14: Plot of silicon mixers with PCA reaction.....	15
Figure 8-15: Plot of commercial mixers with PCA reaction.....	16
Figure 8-16: Flow visualization jig, cross-sectional view right.....	17
Figure 8-17: Dyes, 100 μ L/s (left) and 1000 μ L/s (right).....	18
Figure 8-18: Comparison of mixing quality with different flow regimes.	19
Figure 8-19: Visual estimation of mixing time is 50 to 100 μ s	20
Figure 8-20: Mixer designed with sharp wedges and a convex trapezoid	21
Figure 8-21: Comparison of two mixer chips with identical reaction lengths	22

List of Tables

Chapter 1

Table 1-1: Mass spectrometer has superior sensitivity	7
---	---

Chapter 2

Table 2-1: Factors Affecting Particle Adhesion.....	1
Table 2-2: Breakdown of various particle forces and equations	11

Chapter 3

Table 3-1: Description of 1st generation designs.....	3
Table 3-2: Particle types and sizes	5
Table 3-3: Relaxation times of particles	13
Table 3-4: AZ P4400 resist spin chart.....	14
Table 3-5: Properties of Dupont Teflon® AF1601S.....	17
Table 3-6: A1601S Spin chart.....	17
Table 3-7: Linear electrodes 8 μ m spacing structure, 8 μ m glass particles	18
Table 3-8: Simulation parameters	22

Chapter 4

Table 4-1: DEP electrical requirements for different media.	3
Table 4-2: Properties of Sylgard® 184	12
Table 4-3: Sylgard® 184 spin chart	13

Chapter 5

Table 5-1: Mass spectrometer has superior sensitivity	1
Table 5-2: Comparison of MS ionization methods	4

Chapter 6 (no tables)**Chapter 7**

Table 7-1: Electric field concentration at the nozzle tip for various overhang profiles..... 2

Table 7-2: Electric field concentration at the nozzle tip for various overhang profiles.... 17

Chapter 8

Table 8-1: Brief overview of liquid mixers..... 4

Table 8-2: Fabricated mixer delay lengths and their respective volumes 5

Table 8-3: Syringe sequence steps for the Biologic quenched flow machine..... 11

Table 8-4: Absorbance procedure 12

Chapter 1

MEMS and Bio-Particle Detection

1.1 Introduction

The emerging area of micro electro mechanical systems (MEMS) has had a long history. The precursor to this technology, the integrated circuit, was developed in the '60's by Jack Kirby [1] and Robert Noyce [2]. Prior to their invention (actually in 1958) all the components of a computing circuit had to be individually soldered taking up vast amounts of room, adding to manufacturing complexity, and often prone to failure. The miniaturization and integration revolution started by Kilby and Noyce has resulted in modern mainframe computers capable of processing billions of instructions per second [3].

During the semiconductor revolution, where emphasis was on the electronic properties of semiconductor materials (such as polysilicon, silicon nitride, thermal oxide, and aluminum), a few researchers began to study the mechanical properties of these thin films [4] [5]. As early as 1966, engineers had started to use selective silicon bulk etching technology to fabricate three-dimensional microsensors [6]. By the 1970's, such etching techniques had been labeled "micromachining" and were used creating neural probes [7], pressure sensors [8], gas chromatograph columns [9], and other devices. By the 1980's, surface micromachined technology [10] developed at the University of California, Berkeley gave rise to new types of microsensors and actuators [11] such as gyroscopes [12], microgrippers [13], micro-optics [14], digital micromirrors [15] and accelerometers [16]. The hope of these scientists was to do the same for mechanical systems as the IC had done for the electronic circuit, namely, to integrate large numbers of mechanical sensors with electronic circuitry to be able to develop smaller, faster, cheaper, and more complex microsystems. Just as the integrated circuit revolutionized the transport of current, MEMS researchers today are creating microdevices to revolutionize the transport of fluids for bio-analysis. MEMS technology has made it possible to make miniaturized

pumps [17] [18] [19] [20], valves [21] [22] [23] [24], channels [25] [26], reservoirs [27], reactors [28] [29] [30], mixers [31] [32] [33] [34], filters [35] [36] [37], and detection systems [38] [39] [40] [41] [42]. One of the important applications of this technology is in the area portable environmental monitoring for toxins, chemicals, and other bio-particles.

The ability to fabricate microdevices for such applications offers many advantages. MEMS devices can be made smaller and cheaper resulting in low cost portable devices. Reductions of scale also promise faster analyses times and the creation of new on-chip detection chemistries. Furthermore, common manual operations such as pipetting, incubating, and mixing can be automated eliminating human error and increasing throughput. Unfortunately, very few microsystems capable of complete bio-particle analysis exist because of the diversity and complexity of the components that are required. For example, a micromachined automated analytical system would require pumps, valves, channels, reservoirs, mixers, physical filters, chemical filters, electronics, flow meters, external connectors, detectors, etc. [43] [44] [45] [46] [47].

While the emerging area of MEMS has spanned well over four decades, the current state of MEMS technology and research is giving value to the idea of conceiving traditional semiconductor fabrication concepts and applying them to innovative devices for biochemical analysis. With a unique multidisciplinary approach, this thesis examines specific aspects of the current MEMS demands for this bio-particle analysis problem - namely, airborne transport, collection into liquid, liquid sample analysis and fluidic mixing. The following sections in this chapter review MEMS fabrication techniques, MEMS bio-analysis systems, and conclude with the goal and layout of this thesis.

1.2 Micro Electro Mechanical Systems (MEMS)

It may be referred to as “micromachining,” “mechatronics,” “micro system technology (MST)” or MEMS, but the definition still remains the same. After Kurt Peterson’s review paper [48] on “Silicon as a Mechanical Material,” the field was broadly defined as

the method of mass fabricating three-dimensional structures ranging from a few millimeters to submicrometers. Micromachinists tend to divide the micromachining field into two distinct fabrication methods: bulk micromachining and surface micromachining. [49]

Bulk micromachining refers to the selective etching of the substrate to create three-dimensional structures from the remaining material. A silicon substrate is typically associated with this technique which can be etched either isotropically or anisotropically with a variety of chemistries. Anisotropic etchants such as potassium hydroxide (KOH) [50], tetramethylammonium hydroxide (TMAH) [51] and ethylene diamine pyrochatechol (EDP) [52] have etch rates which etch the (111) crystallographic plane in the single crystal silicon wafer at a much slower rate than the other planes. Figure 1-1 illustrates anisotropic etching on two different Si orientations, (100) and (110). Out of the three, KOH has the highest selectivity between $\langle 100 \rangle / \langle 111 \rangle$, TMAH is aluminum selective, and EDP is the most toxic. However, for boron etch stop applications, EDP remains the best performer.

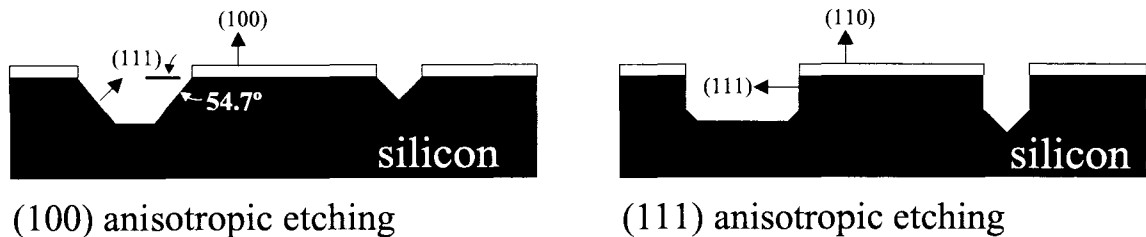


Figure 1-1: Typical silicon anisotropic bulk etching profiles

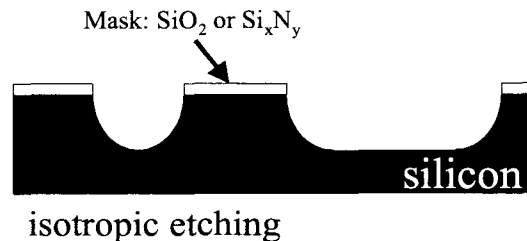


Figure 1-2: Isotropic etching of silicon results in rounded features

Isotropic etching of the silicon substrate with HNA (hydrofluoric acid, nitric acid, and acetic acid) [53] results in rounded features due to equal etch rate in all directions (Figure 1-2). In addition to these wet (liquid based) etchants, the silicon substrate can also be etched isotropically with bromine trifluoride (BrF_3) [54] and xenon difluoride (XeF_2) [55]. The advantage of these vapor based processes is three-fold: 1) extremely high etch selectivity to silicon dioxide, silicon nitride, and metal, 2) room temperature process, and 3) elimination of surface tension stiction effects on free standing structures [56].

Lastly, another widely popular deep etching technology is deep reactive ion etching (DRIE) which allows very high aspect ratio ($>20:1$) etching of silicon independent of crystallographic orientation. This plasma based process relies on a high density inductively coupled plasma source and an alternating process [57] [58] of etching and protective polymer deposition to achieve the almost 90° wall angles. Photoresist and silicon dioxide can be used as a masking layer with selectivities of 80:1 and 120:1, respectively.

Unlike bulk machining, surface micromachining, technology was originally characterized by the fabrication of structures from deposited thin films such as polysilicon [59] [60], silicon nitride [61], and various silicon dioxides [62] [63]. The technique employs the sequential deposition and selective removal of thin films as the structural layer or the sacrificial layer. The substrate (silicon, quartz, glass, alumina, or even plastic) plays a passive role in this technique and only provides mechanical support. An example of a sequence of surface micromachining steps is illustrated in Figure 1-3. First, a sacrificial layer is deposited and patterned. Next, the structural layer is laid down and patterned. Finally, the sacrificial layer is etched away releasing the structural layer except where it is retained by an attachment to the silicon surface.

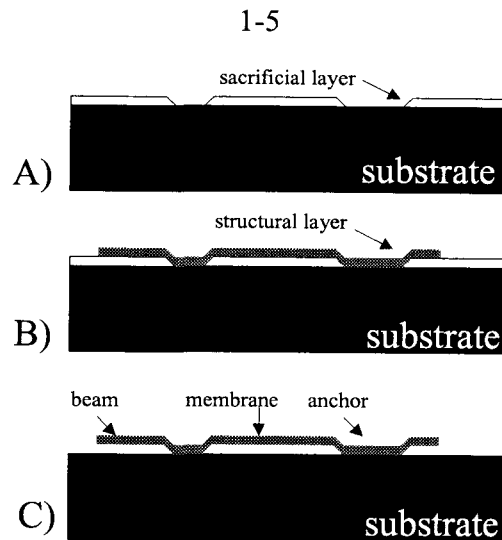


Figure 1-3: Example of a surface micromachining fabrication sequence

Polysilicon pin joints and motors [64], succeeded by electrostatic comb-drive actuators [65] and complex fold out structures [66] [67] were the direct result of this type of process. In 1991, Analog Devices Inc., developed surface micromachined accelerometers [68] integrated with CMOS circuits which are now commercially available. Today, the realm of surface micromachining materials have expanded to include such as silicon nitride/PSG [69], aluminum/polyimide [70], Parylene/photoresist [71], polysilicon/silicon nitride [72], and polysilicon/copper [73]. Surface micromachining offers submicron control over features, but also is susceptible to film stress which causes out-of-plane bending, grain size which affects the Young's Modulus [74] [75], and stiction problems during the release etch [76] [77] [78] [79].

Other micromachining technologies include LIGA [80], silicon carbide MEMS [81], silicon-silicon fusion bonding [82], electrical discharge machining [83], polymer hot embossing [84], and plastic injection molding [85].

1.3 Airborne Sampling and MEMS

In the past decade, researchers have demonstrated feasibility for microsystems for biochemical analyses such as PCR-on-a-chip [86], immunoassays [87], antibody detection [88], and chemical warfare gas detection [47], but for bio-particle airborne

sampling, almost no microsystems exist. As Poruthoor and Dasgupta [89] point out, automated measurement techniques for gaseous and chemical components of ambient have been extensively developed [90], but no commercial instruments exist for rapid in situ measurement of the biochemical composition of aerosol particles. Typically, chemical analysis of bio-particles has largely been conducted offline in separate batch processes – collection and analysis. Particle collection is normally accomplished by inertial techniques such as gravitational settling, centrifuging, filtration, electrostatic, or thermal precipitation [91]. For bio-particles it is imperative that the detection instrument be based on wet chemistry because of the many accepted biochemical analytical protocols available. Furthermore, wet chemistry has the potential to be fast, sensitive, and affordable, provided there are easy methods for continuous collection and transfer of aerosols to such analyzers.

However, easy methods are not available for automated particle collection. Most MEMS detection systems forego the sample collection step and focus purely on detection. Collection and transport of airborne particles becomes a difficult task because of the complex surface adhesion forces acting on the particles [92] [93]. Extensive amount of research has been done for manipulating particles in liquid [94][95][96] but the transport of particles from an air medium to the liquid medium is not a simple task. Large automated systems typically resort to manual intervention at this step in the system or others have shown wetted screen type diffusion denuders. These denuders are typically 30cm wetted parallel screens which trap particles traveling in an adjacent air stream [97]. Devices as large as this are obviously unsuitable for the microfluidic components that have already been developed for chip based bio-analyses.

Another area that is needed for sensitive analysis is the mass spectrometer. There has been significant advancement in MEMS based chemical separation systems, but on-chip detection can be performed mainly by methods such as UV absorbance and electrochemi-luminescence [98]. These optical methods are not viable for most biomolecule (protein and peptide) detection; they are no match for the femtomole sensitivity,

selectivity, and versatility (minimal liquid sample preparation) provided by a mass spectrometer (MS) (Table 1-1).

Table 1-1: Mass spectrometer has superior sensitivity

Detection Method	Approximate Detection Limits
UV/visible absorbance	10^{-13} - 10^{-16} Moles
Fluorescence	10^{-15} - 10^{-17} Moles
Mass spectrometry	10^{-16}-10^{-17} Moles

Furthermore, because of this tremendous advantage in sensitivity, mass spectrometry is ideally suited for detection from on-chip small sample volumes [99] [100]. This femtomolar sensitivity then can be crucial for MEMS environmental monitoring systems where permissible concentrations are extremely low.

1.4 The Purpose and Organization of this Thesis

The aim of this work is to develop micromachined devices for the area of bio-particle analysis. Much of the research here has been funded by DARPA to develop a handheld system for airborne virus and toxin detection in chemical/biological warfare environments. As noted, although MEMS technology promises many innovations, the diversity and complexity of components that are required for such a micro-analysis system are daunting. As a result, this project has involved fluid dynamists, electrical engineers from the UCLA, several biology groups, and members of the Caltech Micromachining Lab to research issues such as air flow in microfilters, micropumps, microvalves, check-valves, detection protocols, and low powered detection electronics. Accordingly, the work here focuses on new key components that are required to realize this bioaerosol detection system.

This thesis is organized as follows:

- Chapter 2 discusses the fundamental forces governing typical airborne particles and illustrates the performance envelope of past particle transportation devices.

- Chapter 3 details the development design, fabrication, and testing of MEMS transportation chip over several generations. Experimental trends are compared to electrostatic simulations to verify the improved performance with dielectric insulators such as photoresist and Teflon.
- Chapter 4 attacks the difficult problem which has plagued the design of bio-particle detector – particle transport from air into a liquid system. To further demonstrate more applications of this transportation technology, a prototype combining an active filter, transportation electrodes, and the air liquid interface was fabricated and tested.
- In Chapter 5, the motivation for on-chip electrospray ionization is explained together with the importance of the mass spectrometer as a bio-analytical tool.
- Chapter 6 outlines the development of the first surface micromachined electrospray nozzle.
- Chapter 7 concludes this topic with more nozzle generations/thin film problems and flow visualization of an electrospray fluid cone from the micromachined chip.
- In Chapter 8, the area of fast mixing for liquid chemical reaction studies is explored. Chemical calibration with a novel fast reaction and extensive flow visualization authenticate the mixing chip's ability to conduct quenched flow 100 μ s quenched flow experiments.
- Finally, Chapter 9 concludes with a synopsis and some future trends in the area of MEMS bio-analytical systems.

References

1. Texas Instruments, Inc., <http://www.ti.com/corp/docs/kilbyctr/jackbuilt.shtml>.
2. Fairchild Semiconductor Corp., <http://www.fairchildsemi.com/company/history.html>.
3. CNEWS website, http://www.canoe.ca/TechNews9905/03_ibm.html, May 3, 1999.
4. H.C. Nathanson, W.E. Newell, R.A. Wickstrom, and J.R. Davis, Jr., "The resonant gate transistor," *IEEE Transactions on Electron Devices*, Vol. ED-14, pp. 117-133, 1967.
5. R.W. Hoffman, "Stresses in thin Films: The Relevance of Grain Boundaries and Impurities," *Thin Solid Films*, 34, 185-90, 1975.
6. H. Robbins and B. Schwartz, "Chemical Etching of Silicon, II. The System HF, HNO₃, H₂O and HC₂H₃O₂," *Journal of Electrochemical Society*, Vol. 107, pp. 108-111, 1960.
7. J. A. Wright, S Tatic-Lucic, Y-C Tai, M. P. Maher, H. D. and J.. Pine, "Towards a Functional MEMS Neurowell by Physiological Experimentation," *Technical Digest: ASME 1996 International Mechanical Engineering Congress and Exposition, DSC-Vol. 59, Atlanta, GA, pp. 333-338, Nov. 1996.*
8. S. Sugiyama, T. Suzuki, K. Kawahata, K. Shimaoka, M. Takigawa, and I. Igarashi, "Micro-Diaphragm Pressure Sensor," *Proceedings of IEEE International Electron Devices Meeting*, pp. 184-187, Los Angeles, USA, Dec. 1986.
9. S.C. Terry, J.H. Jerman, and A.J.B., "A Gas Chromatographic Air Analyzer Fabricated on a Silicon Wafer," *IEEE Trans. Electron Devices*, ED-26, 1880-6, 1979.
10. L. S. Fan, Y. C. Tai, and R. S. Muller, "Integrated Movable Micromechanical Structures for Sensors and Actuators," *IEEE Transactions on Electron Devices*, Vol. ED-35 (6), pp. 724-730, June 1988.
11. P. Barth, C. C. Beatty, L. A. Field, J. W. Baker, and G. B. Gordon, "A Robust Normally Closed Silicon Microvalve," *Technical Digest, Solid-State Sensor and Actuator Workshop*, pp. 248-250, Hilton Head Island, South Carolina, USA, June 1994.

12. C. Song, "Commercial Vision of silicon based inertial sensors," Technical Digest 9th International Conference on Solid State Sensors and Actuators (Transducer's '97), Chicago, IL, June 1997, pp.839-842.
13. C. J. Kim, A. P. Pisano, R. S. Muller, and M. G. Lim, "Polysilicon Microgripper," Technical Digest, IEEE Solid-State Sensors and Actuators Workshop, pp. 48-51, Hilton Head Island, South Carolina, USA, June 1990.
14. L.Y. Lin, S.S. Lee, M.C. Wu, and K.S. J. Pister, "Micromachined integrated optics for free space interconnection," in Proc. IEEE MEMS Workshop, Amsterdam, Netherlands, 1995.
15. L.Hornbeck, "Current status of the digital micromirror device (DMD) for projection television applications," Proc. IEEE Int. Electron Devices Meeting, Washington D.C., Dec. 1993.
16. L. Spangler and C.J. Kemp, "ISAAC – Integrated Silicon automotive accelerometer," Tech. Dig. 8th Int. Conf. Solid-State Sensors and Actuators (Transducers '95), Stockholm, Sweden, June 1995, pp. 585-588.
17. A. Olsson, P. Enoksson, G. Stemme, and E. Stemme, "Micromachined Flat-Walled Valveless Diffuser Pumps," Journal of Microelectromechanical Systems, Vol. 6 (2), pp.161-166, 1997.
18. S. Miyazaki, T. Kawai, and M. Araragi, "A Piezo-Electric Pump Driven by A Flexural Progressive Wave," IEEE Micro Electro Mechanical Systems, (MEMS '91), Nara, Japan, p. 283-288, 1991.
19. A. Richter, A. Plettner, K. Hoffman, and H. Sandmaier, "Electrohydrodynamic Pumping and Flow Measurement," IEEE MEMS '91, Nara, Japan, 1991, p. 271.
20. H.T. van Lintel, F.C. M. van der Pol, and S. Bouwstra, "A Piezoelectric Micropump Based on Micromachining of Silicon," Sensors & Actuators, 15, 153-167, 1988.
21. M. J. Zdeblick, *A Planar Process for an Electric-to-Fluidic Valve*, Ph.D. Thesis, Stanford University, 1988.
22. H. Jerman, "Electrically-Activated, Micromachined Diaphragm Valve," Technical Digest, IEEE Solid-State Sensor and Actuator Workshop, pp. 65-69, Hilton Head Island, South Carolina, USA, June 1990.

23. J. D. Busch and A. D. Johnson, "Prototype Microvalve Actuator," Proceedings of IEEE Workshop on Micro Electro Mechanical Systems (MEMS'90), pp. 40-41, Napa Valley, USA, Feb.1990.
24. Xing Yang, Charles Grosjean, and Yu-Chong Tai, "A Low Power MEMS Silicone/Parylene Valve," Hilton Head'98, Hilton Head Island, SC, USA, June, 1998.
25. E. B. Arkilic, M. A. Schmidt, and K. S. Breuer, "Gaseous Slip-Flow in Long Microchannels," Journal of Microelectromechanical Systems, Vol. 6 (2), pp.167-178, 1997.
26. S. Wu, J. Mai, Y. Zohar, Y.C. Tai, and C.M. Ho, "A Suspended Microchannel with Integrated Temperature Sensors for High Pressure Flow Studies," Proceedings of International Workshop on Micro Electro Mechanical Systems (MEMS '98), pp. 87-92, Heidelberg, Germany, Jan.1998.
27. M. Jansson, A. Emmer, J. Roerade, U. Lindberg, and B Hok, "Micro vials on a silicon wafer for sample introduction in capillary electrophoresis," Journal of Chromatography, Vol. 626, 1992, 310-4.
28. J.Harrison, K. fluri, N. Chiem, T. Tang, and Z. Fan, "Micromachining Chemical and Biochemical Analysis and Reaction Systems on Glass Substrates," IEEE Conference, Transducers '95.
29. Kämper, W. Ehrfeld, J. Döpfer, V. Hessel, H. Lehr, H. Lowe, Th. Richter, and A. Wolf, "Microfluidic Components for Biological and Chemical Microreactors," MEMS '97.
30. H. Mobius, W. Ehrfeld, V. Hessel, and Th. Richter, "Sensor Controlled Processes in Chemical Microreactors," Transducers '95.
31. R. Miyake, T.S. Lammerink, M. Elwenspoek, and J. Fluitman, "Micro Mixer with Fast Diffusion," MEMS 1993.
32. N. Schwesinger, and T. Frank, "A static micromixer built up in silicon," SPIE Vol. 2642.
33. A. Yotsumoto, R. Nakamura, S. Shoji, and T.Wada, "Fabrication of an Integrated Mixing/Reaction Micro Flow Cell For μ TAS," Proc. Micro TAS Workshop, Banff, Canada, Oct. 1998.
34. T. Fujii, K. Hosokawa, S. Shoji, A. Yotsumoto, T. Nojima, and I. Endo, "Development of a Microfabricated Biochemical Workbench – Improving Mixing Efficiency," Proc. Micro TAS Workshop, Banff, Canada, Oct. 1998.

35. G. Kittilsland, G. Stemme, and B. Norden, "A Sub-Micron Particle Filter in Silicon," *Sensors and Actuators (A: Physical)*, Vol. 23, pp. 904-907, 1990.
36. C. J. M. van Rijin and M. C. Elwenspoek, "Micro Filtration Membrane Sieve with Silicon Micro Machining for Industrial and Biomedical Applications," *Proceedings of IEEE Workshop on Micro Electro Mechanical Systems (MEMS'95)*, pp. 83-87, Amsterdam, The Netherlands, January 1995.
37. O. Bakajin, R. Carlson, C.F. Chou, S.S. Chan, C. Gabel, J. Knight, T. Cox, and R.H. Austin, "Sizing, Fractionation and Mixing of Biological Objects Via Microfabricated Devices," *Proc. Micro TAS Workshop, Banff, Canada*, Oct. 1998.
38. M. A. Burns, C. H. Mastrangelo, T. s. Sammarco, P.F. Man, J.R. Webster, B.N. Johnson, B. Foerster, D.K. Jones, Y. Fields, A. R. Kaiser, and D. T. Burke, "Microfabricated Structures for integrated DNA Analysis," *Proc. National Academy of Sciences, USA*, Vol. 93, pp.5556-5561, 1996.
39. R A. Mathies, P. C. Simpson, and A. T. Wooley, "DNA Analysis with Capillary Array Electrophoresis Microplates," *Proc. Micro TAS Workshop, Banff, Canada*, Oct. 1998.
40. A.E. Bruno, E. Baer, R. Volkel, and C.S. Effenhauser, "Microoptical Fluorescence Detection for Chip-Based Multiplexed Analysis Systems," *Proc. Micro TAS Workshop, Banff, Canada*, Oct. 1998.
41. M. Madou, "Compatibility and Incompatibility of Chemical Sensors and Analytical Equipment with Micromachining," *Technical Digest Solid State Sensor & Actuator Workshop, Hilton Head Island, SC*, 1994, p.164-171.
42. F.S. Ligler, C A. Rowe, S. Balderson, M. Feldstein, and J.P. Golden, "Fluorescence Array Biosensor – Biochemistry and Application," *Proc. Micro TAS Workshop, Banff, Canada*, Oct. 1998.
43. M. Elwenspoek, T.S. Lammerink, R. Miyake, and J. H. J. Fluitman, "Towards integrated microliquid handling systems," *J. Micromech. Microeng.*, Vol. 4, 1994, p. 227-245.
44. E. Verpoorte, A. Manz, H. M. Widmer, B. van der Schoot, and N.F. de Rooij, "A Three-Dimensional Micro Flow System for a Multi-step Chemical Analysis," *7th Int. Conf. Sensors & Actuators*, 1994.

45. A. Manz, D. J. Harrison, E. Verpoorte, J.C. Fettinger, H. Ludi, and H. M. Widmer, "Miniaturization of Chemical Analysis Systems – A Look into Next Century's Technology of Just a Fashionable Craze?" *Chimia*, Vol. 45, 1991, 103-105.
46. S. Attiya, X. C. Qiu, G. Ocvirk, N. Chiem, W. E. Lee, and D. J. Harrison, "Integrated Microsystem for Sample Introduction, Mixing, Reaction, Separation, and Self Calibration of Immunoassays," *Proc. Micro TAS Workshop, Banff, Canada*, Oct. 1998.
47. G.C. Frye-Mason, R. J. Kottenstette, E.J. Heller, C. M. Matzke, S. A. Casalnuovo, P. R. Lewis, R. P. Manginell, W. K. Schubert, V. M. Hietala, and R. J. Shul, "Integrated Chemical Analysis Systems for Gas Phase CW Agent Detection," *Proc. Micro TAS Workshop, Banff, Canada*, Oct. 1998.
48. K. E. Peterson, "Silicon as a Mechanical Material," *Proceedings of IEEE*, Vol. 70 (5), pp. 420-457, May 1982.
49. M. Madou, *Fundamentals of Microfabrication*, CRC Press, Boca Raton, 1997.
50. J. B. Price, "Anisotropic etching of silicon with KOH-H₂O-isopropyl alcohol," *Semiconductor Silicon*, NJ: Electrochemical Society, 1973, p.339.
51. Bassous, E. and C.-Y. Liu, "Polycrystalline Silicon Etching with Tetramethylammonium hydroxide, in US Patent 4,113,551, 1978.
52. A. Reisman, M. Berkenblit, S.A. Chan, F.B. Kaufman, and D.C. Green, "The Controlled Etching of Silicon in Catalyzed Ethylenediamine-Pyrocatechol-Water Solutions," *Journal of Electrochemical Society*, Vol. 126 (8), pp. 1406-1415, 1979.
53. H.R. Robbins and B. Schwartz, "Chemical Etching of Silicon-I. The System HF, HNO₃, and H₂O," *J. Electrochem. Soc.*, Vol. 106, p.505-508, 1959.
54. X. Q. Wang, X. Yang, K. Walsh, and Y.C. Tai, "Gas Phase Silicon Etching with Bromine Trifluoride," *Technical Digest, International Conference on Solid-State Sensors and Actuators (Transducers'97)*, Vol. 2, pp. 1046-1415, Chicago, USA, June 1997.
55. P. B. Chu, J. T. Chen, R. Yeh, G. Lin, J. C. P. Huang, B. A. Warneke, and K. S. J. Pister, "Controlled Pulsed Etching with Xenon Difluoride," *Technical Digest, International Conference on Solid-State Sensors and Actuators (Transducers'97)*, Vol. 1, pp. 665-668, Chicago, USA, June 1997.

56. R.L. Alley, G.J. Cuan, R.T. Howe, and K. Komvopoulos, "the Effect of Release Etch Processing on Surface Microstructure Stiction," Technical Digest of the 1988 Sensor and Actuator Workshop, Hilton Head Island, S.C.
57. F. Larmer and P. Schilp, "Method of anisotropically etching silicon," German Patent DE 4,241, 045, 1994.
58. M. Esashi, M. Takinami, Y. Wakabayashi, and K. Minami, "High-rate directional deep dry etching for bulk silicon micromachining," *J. Micromech. Microeng.*, Vol. 5, no. 1, pp. 5-10, Mar. 1995.
59. Y. C. Tai, *IC-Processed Polysilicon Micromechanics: Technology, Materials and Devices*, Ph.D. Thesis, University of California, Berkeley, 1989.
60. A. C. Adams, "Dielectric and Polysilicon Film Deposition," *VLSI Technology*, Sze, S.M., McGraw Hill, 1988, p. 233-271.
61. M. Sakimoto, H. Yoshihara, and T. Ohkubo, "Silicon Nitride Single-Layer X-Ray Mask," *Journal of Vacuum Science & Technology*, Vol. 21, 1017-1021, 1982.
62. T.H. Wu and R. S. Rosler, "Stress in PSG and Nitride Films as Related to Film Properties and Annealing," *Solid State Technology*, May 1992, pp. 65-71.
63. R. A. Levy, "Viscous Behavior of Phosphosilicate and Borophosphosilicate Glasses in VLSI Processing," *Solid State Technology*, Oct. 1986, pp. 123-130.
64. Y.-C. Tai and R. S. Muller, "IC-Processed electrostatic synchronous micromotors," *Sensors and Actuators*, Vol. 20, pp. 48-56, 1989.
65. W. C. Tang, T.-C. H. Nguyen, and R. T. Howe, "Laterally driven polysilicon resonant microstructures," *Sensors Actuators*, Vol. 20, pp. 25-32, 1989.
66. K. S. J. Pister, M. W. Judy, S. R. Burgett, and R. S. Fearing, "Microfabricated Hinges," *Proc. 6th Intl. Conf. Solid State Sensors & Actuators (Transducers '91)*, San Francisco, CA, June 1991.
67. H. Toshiyoshi and H. Fujita, "Electrostatic micro-torsional mirrors for an optical switch matrix," *J. Microelectromechanical Systems*, Vol. 5, pp. 231-237, 1996.
68. T. A. Core, W. K. Tsang, and S. J. Sherman, "Fabricated Technology for an Integrated Surface Micromachined Sensor," *Solid State Technology*, Vol. 36, pp. 39-47, 1993.

69. J. Q. Liu, Y. C. Tai, J. Lee, K. C. Pong, Y. Zohar, and C. M. Ho, "*In Situ* Monitoring and Universal Modeling of Sacrificial PSG Etching Using Hydrofluoric Acid," Proceedings of IEEE Workshop on Micro Electro Mechanical Systems (MEMS '93), pp. 71-76, Fort Lauderdale, USA, Feb. 1993.
70. C. Storment, D. Borkholder, V. Westerlind, J. Suh, N. Maluf, and G. Kovacs, "Dry-Released Process for Aluminum Electrostatic Actuators," Technical Digest, Solid-state Sensor and Actuator Workshop, pp. 95-98, Hilton Head Island, South Carolina, USA, June 1994.
71. P. Man, D. Jones, and C. Mastrangelo, "Microfluidic Plastic Capillaries on Silicon Substrates: A New Inexpensive Technology for Bio Analysis Chips," Proceedings of IEEE Workshop on Micro Electro Mechanical Systems Workshop (MEMS '97), pp. 311-316, Nagoya, Japan, Jan. 1997.
72. O. Tabata, H. Funabashi, K. Shimaoka, R. Asahi, and S. Sugiyama, "Surface Micromachining Using Polysilicon Sacrificial Layer," Proceedings of International Symposium on Micromachine and Human Science, pp.163-172, Nagoya, Japan, Oct. 1991.
73. T. R. Tsao, T. Y. Hsu, and Y. C. Tai, "Copper Sacrificial Layer Technology for Use in Surface Micromachining," Micromachining Workshop III, Southern California Chapter of American Vacuum Society, Anaheim, CA, Sep. 1996.
74. Y.-C. Tai and R. S. Muller, "Measurement of Young's Modulus on microfabricated structures using a surface profiler," Proc. IEEE MEMS Workshop, Napa Valley, CA, Feb. 11-14, 1990.
75. X. Yang, F. M. Siu, and Y. C. Tai, "Strength of Surface Micromachined Diaphragms," MRS Spring Meeting, Symposium N: Microelectromechanical Structures for Material Research, San Francisco, CA, April 1998.
76. C. H. Mastrangelo and C. H. Hsu, "Mechanical Stability and Adhesion of Microstructures under Capillary Forces – Part I, II," Journal of Microelectromechanical Systems, Vol. 2, pp. 30-55, 1993.
77. P.F. Man, B.P. Gogoi, and C.H. Mastrangelo, "Elimination of post release adhesion in micro-structures using conformal fluorocarbon coatings," IEEE/ASME J. Microelectromechal Systems, Vol. 6, pp. 25-34, 1997.
78. M. R. Houston, R. Maboudian, and R. T. Howe, "Self assembled monlayer films as durable anti-stiction coatings for polysilicon microstructures," Proc. IEEE Solid State Sensor and Actuator Workshop, Hilton Head Island, SC, June 3-6, 1996, pp. 42-47.

79. S. Tatic-Lucic, P. Jaramillo, J. Bustillo, S. Cunningham, L. Starr, "Application of statistical analysis on the evaluation of anti-stiction methods for micromechanical devices," Proc. 11th Eur. Conf. Solid State Transducers, Eurosensors XI, Warsaw, Poland, Sep., 1997, pp. 297-300.
80. A. Rogner, W. Ehrfeld, D. Münchmeyer, P. Bley, C. Burbaum, and J. Mohr, "LIGA-Based Flexible Microstructures for Fiber-Chip Coupling," Journal of Micromechanics and Microengineering, Vol. 1 (3), pp. 167-170, 1991.
81. A. J. Fleischman, S. Roy, C. A. Zorman, and M. Mehregany, "Polycrystalline silicon carbide for surface micromachining," MEMS '96, San Diego, CA, Feb. 11-15, 1996, pp. 234-238.
82. K. Peterson, P. Barth, J. Poydock, J. Brown, J. Mallon Jr., and J. Bryzek, "Silicon Fusion Bonding for Pressure Sensors," Technical Digest, IEEE Solid-State-Sensors and Actuators Workshop, pp. 144-147, Hilton Head Island, South Carolina, USA, June 1988.
83. T. Masaki, K. Kawata, and T. Masuzawa, "Micro Electro-Discharge Machining and Its Applications," Proceedings of IEEE Workshop on Micro Electro Mechanical Systems (MEMS'90), pp. 21-26, Napa Valley, USA, Feb. 1990.
84. H. Becker, W. Dietz, P. Dannberg, "Microfluidic Manifolds by Polymer Hot Embossing For μ -TAS Applications," Proc. Micro TAS Workshop, Banff, Canada, Oct. 1998.
85. R. C. Anderson, G. J. Bogdan, and R. J. Lipshutz, "Miniaturized Genetic-Analysis System," Technical Digest, Solid-State-Sensors and Actuators Workshop, pp. 258-261, Hilton Head Island, South Carolina, USA, June 1996.
86. M.U. Kopp, M.B. Luechinger, and A. Manz, "Continuous Flow PCR on a Chip," Proc. Micro TAS Workshop, Banff, Canada, Oct. 1998.
87. W.E. Lee, D. E. Bader, D.J. Harrison, T. Tang, N. Chiem, *et al.*, "Automated Microchip Platform for Biochemical Analysis," Proc. Micro TAS Workshop, Banff, Canada, Oct. 1998.
88. M.J. Feldstein, J.P. Golden, and F. S. Liger, "Fluorescence Array Biosensor Part 1: Optics and Fluidics," Proc. Micro TAS Workshop, Banff, Canada, Oct. 1998.
89. S.K. Poruthoor, and P.K. Dasgupta, "An automated instrument for the measurement of atmospheric aerosol composition," American Laboratory, Feb. 1997.

90. K. Ito, C. Chasteen, H-K Chung, S. K. Poruthoor, Z. Genfa, and P.K. Dasgupta, "A Continuous Monitoring System for Strong Acidity in Aerosols," *Anal. Chem.* Vol. 70, pp. 2839-2847, 1998.
91. C.S. Cox and C.M. Wathes, *Bioaerosols Handbook*, Lewis Publishers, Boca Raton, 1995.
92. D.W. Cooper, H.L. Wolfe, J.T.C. Yeh, and R.J. Miller, "Surface Cleaning by Electrostatic Removal of Particles," *Aerosol Science and Technology*, Vol. 13, 116-123, 1990.
93. A.D. Zimon, "Adhesion of Dust and Powder," Consultants Bureau, New York, 1982.
94. Ashkin A and Dziedzic Jm, "Internal Cell Manipulation Using Infrared-Laser Traps Proceedings Of The National Academy Of Sciences Of The United States Of America, Vol. 86: (20) 7914-7918 Oct. 1989.
95. Ashkin A, "Forces of a single-beam gradient laser trap on a dielectric sphere in the ray optics regime," *Methods In Cell Biology*, Vol. 55 pp.55: 1-27 1998.
96. Fuhr G, Fiedler S, Muller T, Schnelle T, Glasser H, Lisec T, Wagner B, "Particle Micromanipulator Consisting Of 2 Orthogonal Channels With Traveling-Wave Electrode Structures" *Sensors And Actuators A-Physical* 41: (1-3) 230-239 April 1, 1994.
97. P.K. Dasgupta, L. Ni, S.K. Poruthoor, and D. C. Hinds, "A Multiple Parallel Plate Wetted Screen Diffusion Denuder for High Flow Air Sampling Applications," *Anal. Chem.* Vol. 69, pp. 5018-5023, 1997.
98. L. J. Nelstrop, G. M. Greenway, and S.N. Port, "Investigation of Chemiluminescent Microanalytical Systems," *Proc. Micro TAS Workshop, Banff, Canada, Oct. 1998.*
99. F. Foret, H. Liu, B. Zhang, C. Felten, and B.L. Karger, "Microdevices for Electrospray Mass Spectrometry," *Proc. Micro TAS Workshop, Banff, Canada, Oct. 1998.*
100. N. H. Bings, C. D. Skinner, C.Wang, C. L. Colyer, D.J. Harrison, J. Li, and P. Thiebault, "Coupling Electrospray Mass Spectrometry to Microfluidic Devices with Low Dead Volume Connections," *Proc. Micro TAS Workshop, Banff, Canada, Oct. 1998.*

Chapter 2

Particle Transportation Fundamentals

2.1 Introduction

The ability to transport and manipulate particles in air is desirable in many instruments such as airborne particle samplers [1], particle sorters, and electrostatic particle-cleaning apparatuses [2]. There are many different ways to transport particles larger than 10 μm such as forced air jets [1], centrifuges, and other mechanical means [1]. However for particles ranging from 1 to 10 μm , there is still no efficient way to transport them because complex surface forces, instead of gravitational force, dominate. Current particle conveyance methods are cumbersome, often requiring manual rinsing and pipetting [1]. These surface forces acting on these sizes of particles can be separated into three parts: London-Van der Waals force, coulombic force, and meniscus force. Though only three in number, these forces are easily affected by many parameters which are very difficult to control [3]. The table below is a brief list of possible factors affecting particle adhesion to a surface.

Table 2-1: Factors Affecting Particle Adhesion

Surface contamination	Particle to surface distance	Net charge
Polarization	Humidity	Contact Area
Surface roughness	Time of contact	Particle shape
Meniscus radius	Dielectric constant	Homogeneity of particle
Interaction between particles		

Consequently, these factors have added complexity to the development and study of particle transportation systems. In the past, successful transportation of *sub* 10 μm particles has been accomplished in the liquid medium [14], but not on a solid surface in air. In air, Moesner and Higuchi [4] and Balachandran et al. [5] have demonstrated motion of larger particles with voltages up to a few kV. Unfortunately, in the sub 10 μm regime, the electrostatic forces that can be exerted on the particle are of the same magnitude as the adhesive forces between the particle and the solid surface. Numerous researchers have noted this size range cut-off. For example, Novick et al. [3] have noted that the sub 10 μm range presents a different regime where surface adhesive forces and particle charging hinder the successful engineering of a robust particle transport system.

The goal of this work, then, is to reexamine this difficult task and design a dielectrophoretic (DEP) particle transportation system [4-6] capable of moving particles below 10 μm in air with low voltages. The following sections review some of the basic forces governing particles in this size domain and discuss the fundamentals of the DEP force.

2.2 Particle Adhesion Forces in Air

The adhesion forces between a μm -sized particle and a surface are mostly Van der Waals forces, electrostatic forces (image force), meniscus forces, and also gravitational forces [6,7]. It is impossible to calculate the exact contribution of these various forces that govern the adhesion of particles in this size range. Since, the calculation of these forces on micro-particles, even in vacuum, is approximate (order of magnitude) at best [7], in air, these theoretical formulas become more inaccurate because of irregularities of surfaces, molecular adsorption, and stray electronic charging. Nevertheless, we use these formulas to gain an understanding of the magnitude of the forces involved. Many scientists have experimentally studied these phenomena, and have come up with estimates for adhesive forces [3,7]. Because of the irregularity of particle and surface contact areas, experimental results for this range of particles are often denoted in percentages of particles that are removed vs. adhered. Large variation is common with these percentages due to the statistical nature of the phenomena.

2.2.1 Van der Waals Forces

The Van der Waals force stems from close range intermolecular interactions. These forces are often termed dispersion forces, which include London forces, charge-fluctuation forces, electrodynamic forces, and induced-dipole interactions. Much work has been conducted in this area, namely London (1937), Hirschfelder *et al.* (1954), Moelwyn-Hughes (1961), Margenau and Kestner (1971), Israelachvili (1974) and Mahanty and Ninham (1976) [6]. These dispersion forces govern adhesion, surface tension, physical adsorption, wetting, and other key properties of gases, liquids and thin films. This intermolecular force comes into play from distances of 10nm down to 0.2nm. Typically, we can assume that the pair potential between two atoms or small molecules is purely attractive and additive (molecule and other surface are composed of similar molecules and interactions superimpose). With this assumption the pair potential is of the form [8]

$$w(r) = -C/r^n \quad (2-1)$$

where C is the London dispersion force coefficient, r is the distance between the molecules or atoms, and n = 6 for Van der Waals force. By integrating Equation (2-1) for the case of a molecule distance D away from the surface, we arrive at,

$$w(D) = \frac{-2\pi C\rho}{(n-2)(n-3)D^{n-3}} \quad (2-2)$$

where ρ is number density of molecules in the solid. To calculate this interaction energy, $W(d)$, between a sphere and a surface, we have to integrate Equation (2-2) about a sphere of radius R and distance D from the surface (Figure 2-1) [8].

$$W(D) = \frac{-2\pi^2 C\rho^2}{(n-2)(n-3)} \int_{z=0}^{z=2R} \frac{(2R-z)zdz}{(D+z)^{n-3}} \quad (2-3)$$

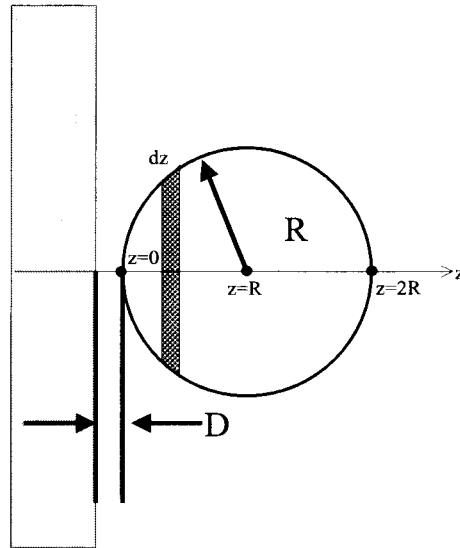


Figure 2-1: Method of summing interaction energy of particle near surface, $D \ll R$ [8].

Assuming $D \ll R$ and $n=6$, we can obtain the Van der Waal interaction energy for a particle on a surface, Equation 2-4.

$$W(D) = -\frac{\pi^2 C \rho^2 R}{6D} \quad (2-4)$$

The corresponding expression for force can be derived by differentiation with respect to D .

$$F(D) = -\frac{\pi^2 C \rho^2 R}{12D^2} \quad (2-5)$$

Typically Equation (2-5) is simplified by coalescing the constants, $\pi^2 C \rho^2 / 12$, into a larger constant called the Hamaker constant. Assessing this dispersion force is difficult because the Hamaker constant can vary from $(0.01 \text{ to } 200) \cdot 10^{-19} \text{J}$ and the particle distance from the surface, D , can also vary from 0.1 to 20nm [2,3,8]. Furthermore, the Van der Waals forces are highly dependent on particle shape, and consequently, quantitative calculations are difficult for irregularly shaped particles.

2.2.2 Coulombic Forces

Coulombic forces on particle arise when a particle develops a net charge. Not much is understood about how particles become charged, but this charge drastically alters the adhesion force between the particle and the substrate. For instance, researchers have shown this charging can increase adhesive forces by a factor of 2 [7]. Others groups have noted that any sliding, rubbing, or rolling contact or normal contact without lateral motion can affect the charge on the particle surface. A detailed hypothesis of the contact potential differences in the energy band gaps can be found in Zimon [7]. Various theories exist to account for particle charging. Kunkel concluded that it is not the friction that causes charging but the making and breaking of contacts [6]. Another fact that complicates this study is that particles tend to interact physically with other particles. This contact also brings about localized surface charging and transportation of charge [6].

A charged particle can experience two types of electrostatic forces (relevant to this work): a) electrostatic attraction, commonly referred to as the Coulomb force and b) an image force. From basic electromagnetic theory, the Coulomb force is generated due to the interaction between an electric field and a charged body (or between charges) and can be described by the following equation:

$$F = qE \quad (2-6)$$

where q is the total charge on a particle and E is the external e-field.

For the case of the image force, the presence of charged particle near a conductor generates an attractive force (Figure 2-2). From electrostatic theory, we see that the force is a strong function of the net particle charge and the distance, Equation (2-7).

$$F(D) = \frac{q q'}{16\pi\epsilon_1 D^2} \quad (2-7)$$

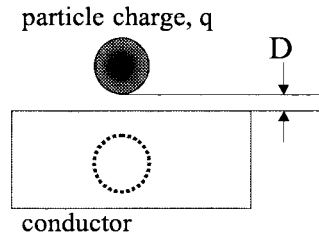


Figure 2-2: Image force between a charged particle near a conductor.

Similar to the difficulty in determining the particle to substrate contact distance for dispersion forces, particle charge, q , is also a quantity that is difficult to judge and control. It has been shown that non-conductive ($>10^3\Omega$) particles (depending on humidity, temperature, and presence of adsorbed layers) tend to retain their charge for long periods of time if no other means of charge leakage are available [7]. Experimental data from [7] shows that this accumulation of charge increases as the particle diameter decreases. More importantly, this charge increase results in an increase in the adhesion force. Another trend discovered is that the repeated detachment of the particle from the substrate results in an order of magnitude increase in q . An example of this trend is shown in the graph below. Data is taken from polyvinyl chloride particles when detached from a metal surface [7]. As will be discussed later, this phenomenon is one of the first roadblocks uncovered in our preliminary particle transportation experiments.

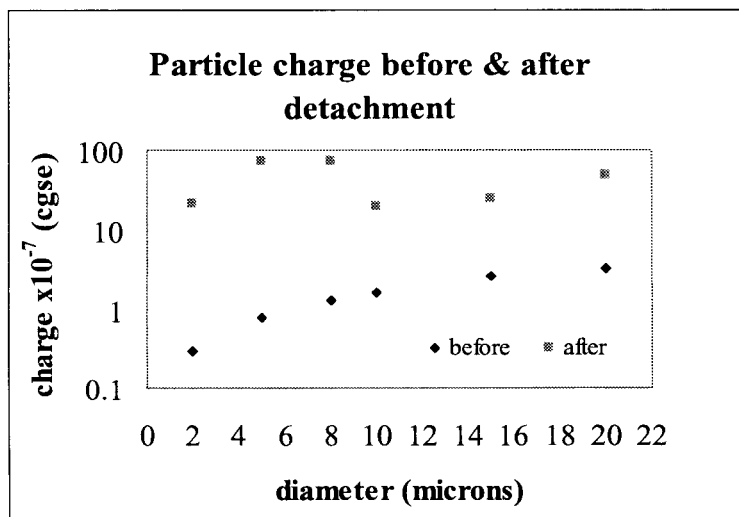


Figure 2-3: Polyvinyl chloride particles show increase in charge after detachment [7].

2.2.3 Meniscus Force

Meniscus forces result from surface tension of adsorbed films at the particle-surface interface. Adhesion in air usually increases when the relative humidity is increased. This meniscus force is created when a film of liquid exists between the particle and the contact surface. If the radius of the film at the contact point is small relative to the radius of the sphere, r , (Figure 2-4) we can derive a simple model between the liquid surface energy and the meniscus force.

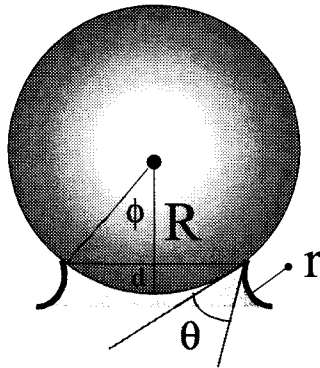


Figure 2-4: Model of capillary condensation of liquid between particle and surface.

The Laplace pressure relationship states that the pressure P between the surface and the particle is given by [8]:

$$P = \gamma_L \left(\frac{1}{r} + \frac{1}{R} \right) \approx \frac{\gamma_L}{r} \quad (2-8)$$

where γ_L is the surface energy of the liquid, r , and R are the radii shown in the figure. When R is much greater than r and when ϕ is small, we can multiply this pressure by the area between the two surfaces and obtain an equation for the meniscus force (Equation 2-2). Also, note that d is approximated to be $2r\cos(\theta)$ when ϕ is small.

$$F \approx 4\pi\gamma_L R \cos\theta \quad (2-9)$$

The angle θ represents the contact angle between the sphere and the liquid. This contact angle depends on the surface properties such as hydrophobicity and surface asperities. The meniscus force model assumes a perfectly smooth surface, and typically adhesion

force values are much lower than predicted maximum except in cases where the relative humidity is close to 100% [8].

2.3 Dielectrophoretic Force for Particle Transportation

Although other types of particle transport schemes can be utilized, the dielectrophoretic (DEP) force [9] is one of the few solutions available for a MEMS system. Without any moving parts, and without high power consumption, the DEP technique offers many advantages in comparison with other transport schemes such as ultrasonic manipulation, liquid washing, and mechanical cilia-type structures [10]. Due to the character of the adhesive forces in this particle size range, DEP forces have been utilized for particle transport in this work. Researchers have designed micromachined manipulators for transport in a dry medium such as air [4,5] but have been limited by high voltage and low transportation efficiencies.

Although much work has been done in investigating the DEP force on particles ranging from dust to biological cells [6,9,11], exact calculation of the DEP forces becomes extremely difficult. The following brief derivation (from [5,9]) of a simple form of the DEP equation demonstrates this complexity and also the specific constraints associated with it.

We can begin with the simplest case by analyzing the force on an infinitesimal dipole (Figure 2-5).

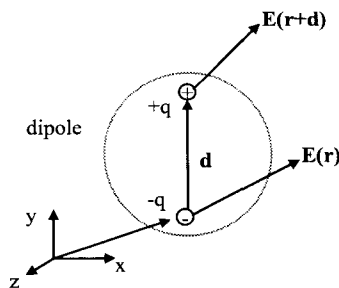


Figure 2-5: Net force on a small dipole of strength $p=qd$ in a non-uniform electric field.

Since the electric field is non-uniform, the force on each charge will be different, and can be expressed as:

$$\mathbf{F} = q\mathbf{E}(\mathbf{r} + \mathbf{d}) - q\mathbf{E}(\mathbf{r}) \quad (2-10)$$

If we assume that \mathbf{d} is small compared to the non-uniformity of the electric field, then the e-field can be expanded about position \mathbf{r} using a Taylor's series expansion. Furthermore, when higher order terms of \mathbf{d} such as d^2 , d^3 are neglected and the limit \mathbf{d} is taken to zero, we arrive at the force equation for a dipole:

$$\mathbf{F}_{dipole} = q\mathbf{d} \cdot \nabla \mathbf{E} \quad (2-11)$$

Equation (2-11) can also be written as

$$\mathbf{F} = \frac{1}{2} \alpha v \nabla |\mathbf{E}|^2 \quad (2-12)$$

where α is the (tensor) polarizability or dipole moment per unit volume in unit field, v is the volume of the body, and \mathbf{E} is the external field. This equation holds true if the dielectric body is linearly, homogeneously, and isotropically polarizable. In other words, the form of Equation (2-12) above can be thought of as $\mathbf{F} = (\text{volume}) \times (\text{polarizability}) \times (\text{local field}) \times (\text{field gradient})$. In place of αv in Equation (2-12), we can substitute the commonly derived expression for the induced moment of a polarizable sphere with radius R , permittivity ϵ_2 , and volume v , in an infinite medium of permittivity ϵ_1 . [12]

$$\alpha v = 4\pi R^3 \epsilon_1 \left(\frac{\epsilon_2 - \epsilon_1}{\epsilon_2 + 2\epsilon_1} \right) \quad (2-13)$$

Finally, a simplified expression results for the special case for a lossless dielectric sphere.

$$F_{DEP} = 2\pi \epsilon_1 R^3 K \nabla |E_0|^2 \quad (2-14)$$

The DEP force is a function of ϵ_1 , the permittivity of the surrounding medium, R , particle radius, and E_0 , the electric field. The constant K is defined as

$$K = \frac{\epsilon_2 - \epsilon_1}{\epsilon_2 + 2\epsilon_1} \quad (2-15)$$

where ϵ_2 is the permittivity of the sphere. The important factor to note is that the DEP force is a strong function of the particle volume (R^3) and the gradient of the electric field squared (∇E_0^2). The latter term makes Equation (2-14) difficult to compute in closed form for spherical particles. If there is no field gradient or if the permittivities of the particle and medium is the same, there is no DEP force. The sign of the K term determines if it is a positive or negative DEP force. When K is positive (or $\epsilon_2 > \epsilon_1$), particles are attracted to the electric field maxima and repelled from the minima. When K is negative (or $\epsilon_2 < \epsilon_1$), particles are attracted to the field minima and repelled from the maxima. Detailed derivations for other DEP cases with conductive and semi-conductive mediums can be found in Jones [6]. Although this simplified form of the DEP equation becomes inexact for some of the experiments in this thesis, it helps us gain a good understanding of the fundamentals behind this electronic force.

It is important to reiterate the numerous assumptions and the limitations of this DEP force equation. For instance, the DEP equation assumes that the electrodes creating the e-field have dimensions much larger than the particles. Derivation of this equation has neglected the case of multiple particles. Multiple particles in close vicinity invalidate this simple model by causing non-uniformities in the e-field which are comparable to the particle size [6]. Particles are assumed to be perfect spheres, and to be electrically neutral. The Table 2-2 below summarizes many of the assumptions inherent in the DEP force equation. Because of these caveats, the DEP structures presented in this work have been analyzed using finite element simulation software, MAXWELL [13].

Table 2-2: Breakdown of various particle forces and equations

Force Type and Reference	Equation	Parameter	Assumptions
DEP force [6]	$F^D = 2\pi\epsilon_1 R^3 K \nabla E_0^2$ $K = \frac{\epsilon_2 - \epsilon_1}{\epsilon_2 + 2\epsilon_1}$	ϵ_1 permittivity of the surrounding medium E_0 electric field	<ol style="list-style-type: none"> 1. homogeneous dielectric sphere 2. lossless dielectric medium 3. slightly non-uniform e-field
Image force [6]	$F^I = \frac{qq'}{16\pi\epsilon_1 R^2}$ $q' = \frac{\kappa_s - \kappa_1}{\kappa_s + \kappa_1} q$ $\kappa_s = \frac{\epsilon_s}{\epsilon_0}$ $\kappa_1 = \frac{\epsilon_1}{\epsilon_0}$	R particle radius q magnitude of particle charge q' magnitude of image charge ϵ_s permittivity of the surrounding medium	<ol style="list-style-type: none"> 1. uniformly distributed charge 2. particle dielectric constant = dielectric constant of surrounding medium 3. particle is a perfect insulator 4. uniform E_0 oriented \perp substrate 5. single particle
Friction force [7]	$F_f = \mu N$	μ friction coefficient N total downward force on particle due to F^D and F^I	<ol style="list-style-type: none"> 1. can be static or kinetic coefficient of friction
F^{st} , stiction forces			
London-Van der Waals [11]	$F = \frac{AR}{d^2}$	A empirical constant $(0.01 - 200) \times 10^{19} \text{J}$ d distance from particle to surface typically 0.1 to 20 nm	
Meniscus [11]	$F = 4\pi\gamma R$	γ surface tension of fluid R particle radius	<ol style="list-style-type: none"> 1. ideal sphere to surface contact
Coulombic [6]	$F = qE$	E electric field q magnitude of particle charge	<ol style="list-style-type: none"> 1. uniform charge distribution 2. uniform electric field

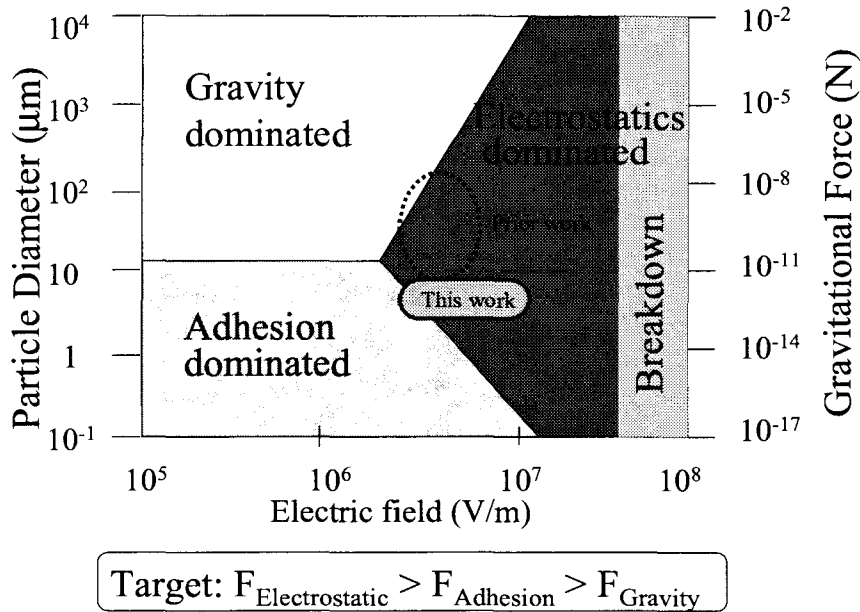


Figure 2-6: Qualitative comparison of particle forces showing the performance regime of operation

2.4 Conclusion

We have discussed in depth the dominant forces and the difficulty in determining the particle adhesive and dielectrophoretic force. A rough calculation from various sources will reveal that adhesive forces on the particle can differ by a few orders of magnitude! However, to gain a better understanding of the regime under which each type of force dominates, a qualitative graphical comparison of forces is illustrated in the graph above. This graph represents (order of magnitude forces) on silica glass particles vs. electric field in a standard room temperature environment with 0% relative humidity. Each region represents the type of force that dominates particles in that particular size range. The boundary line between the regions defines where the magnitude of these forces is approximately equal. For example, the horizontal line between the “gravity dominated” and the “adhesion dominated” regime represents where the adhesion or stiction force is equal to the weight of the particle. Also note that as the particle size decreases below $\sim 10\mu\text{m}$, the adhesive forces dominate the body forces (i.e., gravity). As one travels to the right (increasing electric field), the adhesion and gravitational forces can be defeated with a strong enough DEP force. The electrostatic limitation is breakdown of the e-field in air

as shown at the far right. Therefore, a successful particle transportation device must operate where the electrostatic force is greater than adhesion and gravity. The operational region of the MEMS particle transport system developed here is marked on the graph (Figure 2-6). Above it is the operational regime of some of the prior work in this field [2,3,4].

References

1. C. S. Cox and C.M. Wathes, *Bioaerosols Handbook*, CRC Press LLC, 1995.
2. D.W. Cooper, H.L. Wolfe, J.T.C. Yeh, and R.J. Miller, "Surface Cleaning by Electrostatic Removal of Particles," *Aerosol Science and Technology*, Vol. 13, 116-123, 1990.
3. V.J. Novick, C.R. Hummer, and P.F. Dunn, "Minimum dc electric field requirements for removing powder layers from a conductive surface," *Journal of Applied Physics*, Vol. 65, 3242-3247, 1989.
4. F.M. Moesner, and T. Higuchi, "Devices for Particle Handling by an AC Electric Field," *IEEE Conference Proc. MEMS 1995*.
5. W. Machowski, W. Balachandran, SMIEEE, and D. Hu, "Influence of Electrode Geometry on Transport and Separation Efficiency of Powders Using Traveling Wave Field Techniques," *IEEE*, 1995.
6. T.B. Jones, "Electromechanics of Particles," Cambridge University Press, New York, 1995.
7. A.D. Zimon, *Adhesion of Dust and Powder*, Consultants Bureau, New York, 1982.
8. J. Israelachvili, *Intermolecular & Surface Forces*, Academic Press, London, 1992.
9. H. A. Pohl, *Dielectrophoresis*, Cambridge University Press, Cambridge, 1978.
10. M. Ataka, A. Omodaka, N. Takeshima, and H. Fujita, "Polyimide biomorph actuators for a ciliary motion system," *IEEE/ASME J. Microelectromechanical Systems* Vol. 2, No. 4, pp. 146-150, 1991.
11. C.N. Davies, *Aerosol Science*, Academic Press, London and New York, 1966.
12. A. Von Hippel, *Dielectric and Waves*, Wiley, New York, 1954, p. 39.
13. Maxwell Field Simulator Version 1.7.66, Ansoft Corporation, Four Station Square, Suite 660, Pittsburgh, PA 15219.
14. M. Washizu, T. Nanba, and S. Masuda, "Handling Biological Cells Using a Fluid Integrated Circuit," *IEEE Transactions on Industry Applications*, Vol. 26, No. 2, March 1990.

Chapter 3

The Particle Transportation Chip

3.1 Introduction

To create a practical particle transportation scheme to work in the region illustrated in the previous chapter, various electrode designs and multiple experiments were performed on microfabricated electrode panels. Initially, 1st generation electrode chips were fabricated with an assortment of electrode geometries to test out the DEP concept and investigate the primary adhesion factors for this sub-10 μm particle regime. Hundreds of particle transportation experiments were performed under varying conditions such as voltage waveforms, surface modification, substrate heating, dielectric cycling, and different insulating films. Although many adhesion factors remained ambiguous, particle charging was postulated to be the primary cause of particle stiction, and a subsequent generation of particle transportation chips was designed to maximize particle transportation performance even further. Finally, experimental trends were validated through finite element simulation of the DEP force field. The fundamental engineering of the first low voltage, high efficiency MEMS particle transportation scheme has been advanced in this work.

3.2 1st Generation Fabrication

The particle transportation chip was developed in using standard microfabrication techniques. The fabrication process consisted of depositing two insulation layers and two conductive layers for a three-phase network of electrodes. A cross-sectional view of a finished electrode panel is shown below (Figure 3-1).

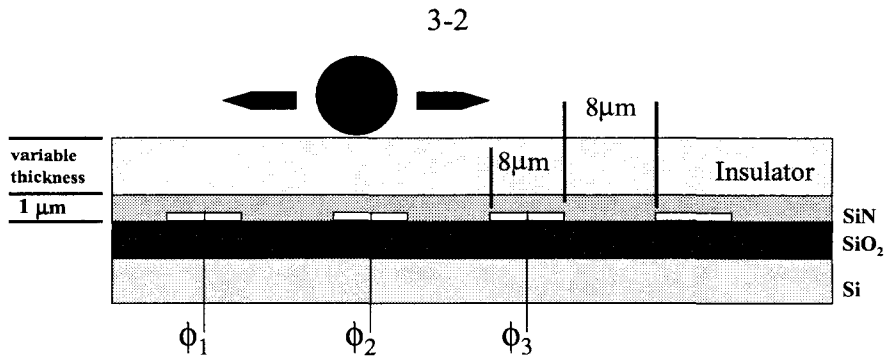


Figure 3-1: Cross-sectional view of electrode chip

The fabrication sequence began with a silicon substrate coated with 1-2 μm of thermal oxide to insulate the electrodes from the n-type silicon substrate. Next, 3000 \AA of aluminum was thermally evaporated and patterned to form the electrodes. Plasma-enhanced chemical vapor deposition (PECVD) silicon nitride was deposited to form a 1 μm insulation layer between the 1st and 2nd metal layers. Vias were etched into this silicon nitride layer for connection of the 2nd Al layer to the 1st. Next, the 2nd Al layer was deposited and patterned. During the first process run, deposition of LTO on the 1st aluminum layer resulted in hillock type formations in the metal layer. Therefore, PECVD silicon nitride was used because of its low temperature deposition (175°C compared to 400°C for LTO). The aluminum hillocks were roughly 2 μm in size and created sharp 1-2 μm protrusions through the LTO layer effectively shorting out the three phase structures. Because of the non-uniform properties of the PECVD nitride and the hillock formation with aluminum and LTO, a similar process using gold instead of aluminum, and (LTO) and photoresist instead of PECVD silicon nitride, were also developed. Cross-sectional views of the process steps are shown in Figure 3-2. With the above process, many electrode designs were fabricated to investigate the feasibility of particle transportation in normal atmosphere.

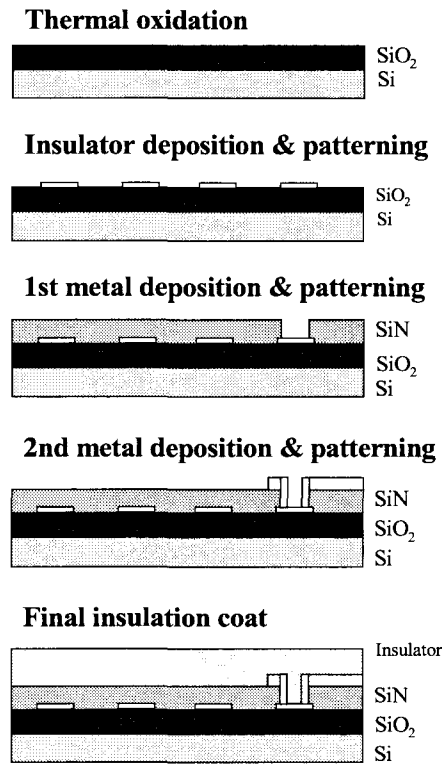


Figure 3-2: Key electrode process steps

3.3 First Generation Designs

In order to understand the optimal type and size of electrodes for DEP transportation of $10\mu\text{m}$ particles, numerous designs were fabricated in the first generation. Linear arrays of parallel electrodes were fabricated for unidirectional transportation. Radial arrays were also designed to attempt to transport particles in circles at high speed. Furthermore, the radial geometry shows the spacing between electrodes which allows motion because of the pitch increase from the center to the outer periphery of the structure. The dimensions of the various structures are displayed in Table 3-1.

Table 3-1: Description of 1st generation designs

Structure type	Electrode width	Spacing	Total size
Linear	$5\mu\text{m}$, $8\mu\text{m}$	$5\mu\text{m}$, $8\mu\text{m}$	$2.5\text{mm} \times 3\text{mm}$
Radial	$5\mu\text{m}$, $8\mu\text{m}$	$>8\mu\text{m}$	1mm (diameter)

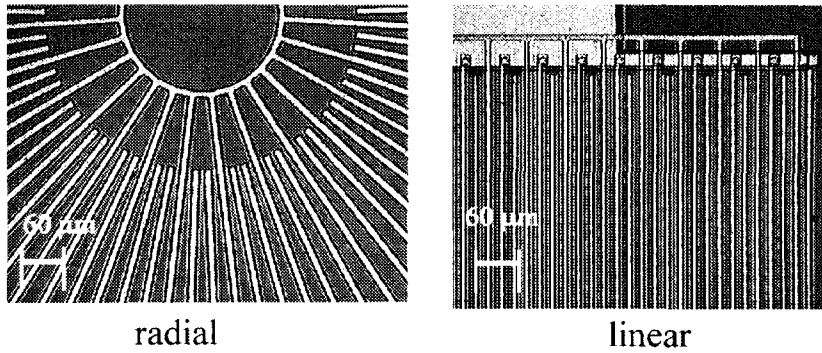


Figure 3-3: Examples of radial and parallel electrode geometries.

3.4 Experimental Setup and Testing

The electrode structures were operated with a 3-phase circuit capable of waveforms from typically 20 to 200V_{pp} with frequencies from 0.1Hz to 10kHz. An example of the voltage patterns required for each phase is illustrated in the schematic (Figure 3-4). The corresponding circuit schematic is shown in Figure 3-5. Experiments were also conducted with other voltage patterns such as sinusoidal waves, triangular waves, bipolar traveling waves, and the inverse of the waveforms shown in Figure 3-4. The effects of these waveforms are discussed below.

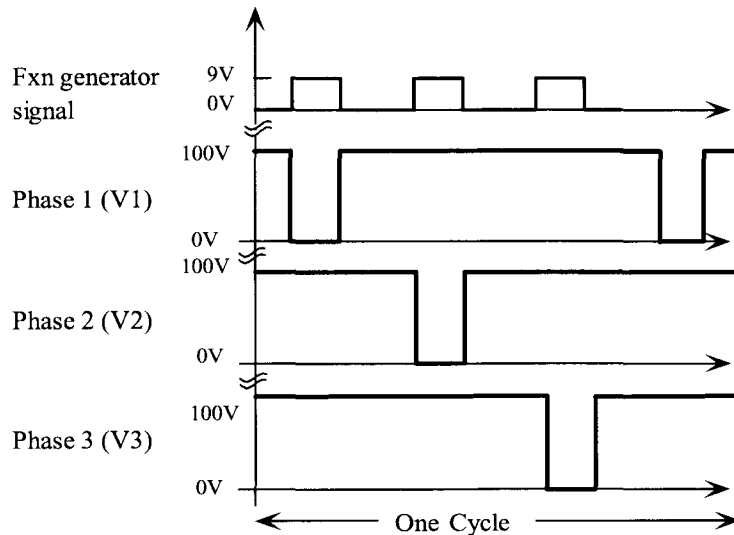


Figure 3-4: Example of three-phase waveform

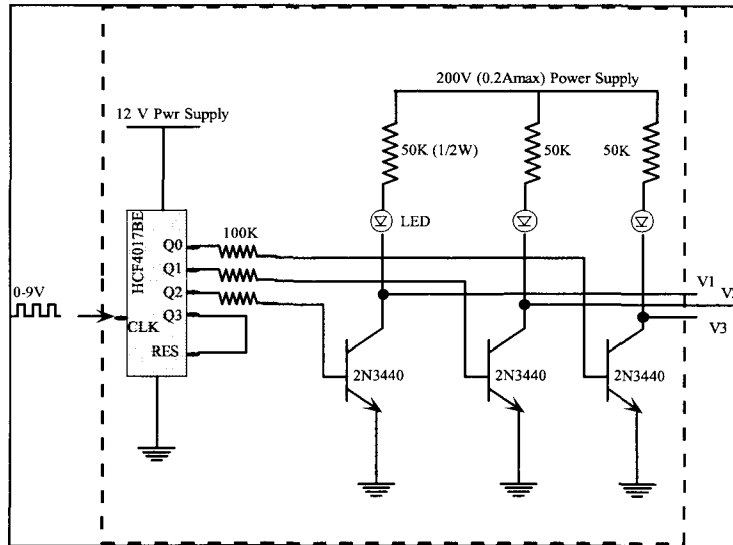


Figure 3-5: Circuit for three phase rectangular waveform (10-200V_{pp})

A variety of particle sizes and materials were tested with this particle transportation chip. Most of the experiments were performed on linear electrode and spacing widths of 5 μ m and 8 μ m (pitch and width spacing is identical). Table 3-2 summarizes the types of particles tested.

Table 3-2: Particle types and sizes

Microspheres	ϵ	Mean diameter(μ m)
Borosilicate Glass	5.8	5, 8, 11, 15.4
Polystyrene DVB	2.5	5, 8.7
Paper Mulberry Pollen*	-	11.1 - 15.6
Bermuda Grass Smut Spores*	-	5.8 - 8.2

*refers to hydrated size, and ϵ , relative permittivity

Testing was conducted as the following: First, the electrode panel was “turned on” and then particles were released on the electrode panel with the aid of a micromanipulator probe tip. As the probe tip neared the electrode panel surface, the traveling electric field force was sufficient to detach particles from the probe tip onto the surface of the transport chip. Multiple sets of experiments for each parameter (particle type, size, insulation,

electrode spacing) were performed in this fashion. Particle efficiency data was gathered by noting the ratio of particles transported to the edge of the linear electrode array vs. the total number of particles on the structure. The snapshots in 3-6 are pictures showing the start and end of one particle transportation trial. Hundreds of trials were performed to generate efficiency data. For the experiments, the laboratory environment was standard room temperature, 22°C and 30-60% relative humidity.

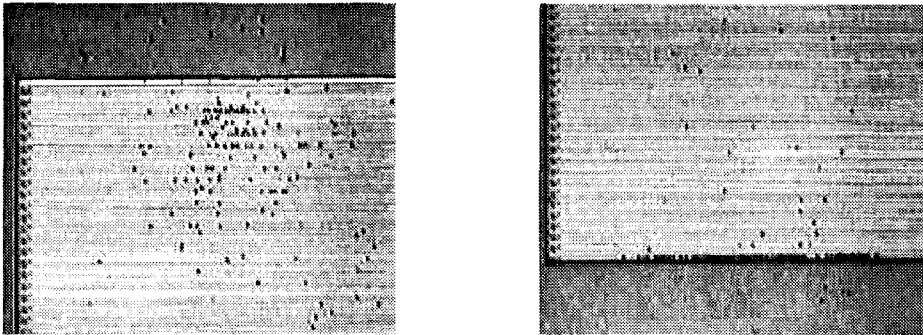


Figure 3-6: Particles before(left) applying waveform and then transported to the bottom edge of the electrodes.

Because of the irregularity of particles and surface contact areas, experimental results for this range of particles are often denoted in percentages of particles that are removed vs. adhered throughout the prior work in this field. It is very important to understand that large variation in these percentages was common due to the statistical nature of the phenomena. One drawback with this method of measurement is with device designs that work so poorly that no particles make it down to the other edge. In this case, it becomes hard to compare two electrode panels, both of which generate particle motion but result in zero efficiency. Ideally, mapping each particle's position, and then calculating weighted averaged length, would certainly be more accurate, but this would be extremely time consuming (1+ hour per trial).

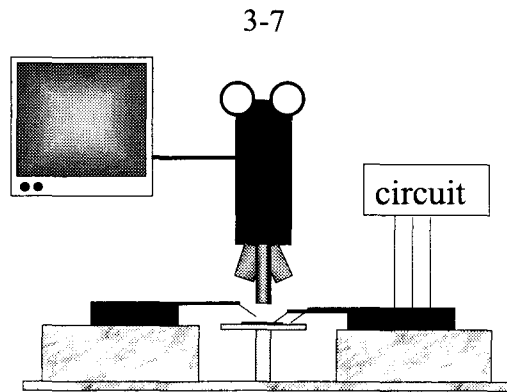


Figure 3-7: Testing setup showing video, μ -scope, probe tips, and circuit

The goal of the first generation of particle transportation chips was twofold – to see how well the DEP technique worked, and to see which electrode designs were suitable for our particle sizes. Initial experiments using the rectangular waveform (Figure 3-4) were conducted on dies with the particles listed in Table 3-2. What quickly became apparent was that DEP motion was clearly not sustainable with the current devices. For the first trials, insulated (PECVD silicon nitride) electrodes as well as bare electrodes were tested. Bare electrode chips could easily be fabricated by modifying the last mask in process Figure 3-2. Regardless of the type of structure or electrode insulation, large threshold voltages (the minimum voltage required to generate any particle movement) were needed, and particles, would exhibit motion for a few seconds and then stop moving. Motion would resume only when the voltage level was increased further. This was observed for voltage levels as high as 250V. Any further increase in voltage larger than 250V resulted in breakdown of the (PECVD Si_xN_y) insulation layer between the 1st and 2nd metal layers on the chip. Dielectric strengths for the nitride and LTO films ranged from $2\text{-}5 \times 10^6$ V/cm. Particles when stopped, generally adhered close to the electrodes and not between them. Figure 3-8 shows a typical pearl chain formation of particles, which could not be moved. The electric field significantly changes for particles in such formation and the DEP forces are greatly reduced [1].

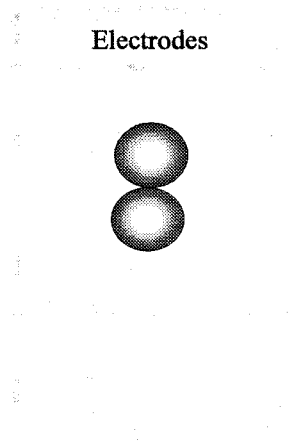


Figure 3-8: Top view of particle stuck in a pearl chain formation.

In conclusion, although the transportation characteristics of these devices were far from ideal, valuable information was gained from these initial tests. The first observation was that the relationship between the particle size and the electrode spacing was non-trivial. For instance, if particles were smaller than the electrode width, no amount of voltage would move the particle. Similar failure would also occur, if the particle size was large enough that the particle spanned more than two electrodes. This size dependency will be explained in the DEP finite element simulation section later in this chapter. Secondly, the frequency range of motion was below 20Hz for the silicon nitride insulated devices. Higher frequencies did not exhibit any movement. Another failure mode that was also observed were particles in a pearl chain formation (Figure 3-8).

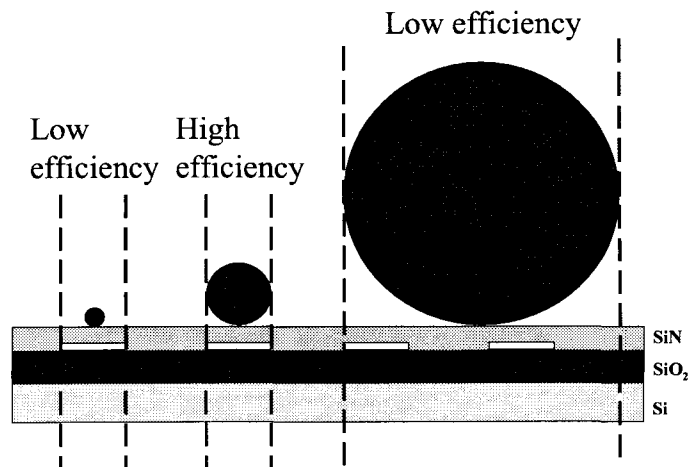


Figure 3-9: Schematic of initial qualitative observations regarding relationship of particle size to electrode widths and spacing

Consequently, a systematic series of experiments was undertaken to ascertain the primary cause of this “stopping problem.” From our discussion of particle forces in Chapter 2, there were mainly Van der Waals forces, meniscus forces, and the electrostatic forces acting on the particles in this size range. Therefore, numerous particle transportation experiments were methodically devised to affect each of these forces. Isolating the different adhesion mechanisms individually was difficult and often each modification affected other forces. For example, a thin 50Å coating of gold was deposited on the electrodes to alleviate particle charging, but this step also shielded the particles from the applied traveling waveform. The following sections detail each specific experiment, its purpose, the specific experimental procedure, the set-up, and the outcome.

3.4.1 Various Three Phase Waveforms

To solve the “stopping problem,” one of the first things that was done was to change the travelling waveform circuit and experiment with other voltages, waveforms, and frequencies. Experiments with triangular waveforms, bi-polar waveforms, grounded waves, and positive waves showed no improvement. A sinusoidal three-phase circuit was also designed, but without any success. The transportation efficiency in the best case was noted to be 10% with a threshold voltage of 80V.

3.4.2 Surface Silanization Treatment

The phenomenon of particles initially moving on the substrate and then stopping seemed unlikely to be caused by meniscus forces. Capillary forces normally would be present at the start of particle motion and not have an increasing effect as previously observed. However, to verify that this problem was not due to capillary forces between the particle and the substrate, the electrode chips were silanized using trimethylchlorosilane (TMCS). TMCS is one of many silanizing agents that can be used for transforming hydrophilic surfaces into more hydrophobic ones [2]. Although most studies indicate that meniscus forces generally do not dominate unless the relative humidity is above 50%, we wanted to

confirm if this trend was indeed true of our microfabricated surfaces. The TMCS coating would increase the contact angle of the liquid film (if present) and reduce the adhesion force in accordance with Equation 2-9 and Figure 2-4.

The coating process was liquid based. The dies were cleaned using acetone, alcohol, and DI water. After immersion for 20 minutes in 4% solution of TMCS in toluene, the dies were rinsed with 100% toluene, and then DI water. The interaction of the solution with exposed aluminum on the die caused large bubbles to form, but no structures were damaged. A DI water rinse showed that the chip surface was very hydrophobic. As expected, the subsequent testing of the silanized chips showed no quantifiable improvement in particle motion characteristics. The particles still moved a little bit and then stopped requiring more and more voltage to move again.

3.4.3 Substrate Heating

Another way to reduce meniscus forces was to perform particle transportation experiments with the chip heated from 90-200°C. From the literature, the effect of the temperature has been shown to both increase and decrease adhesive forces. One hypothesis is that the increase is due to the “softening” of the contact zone between the particles and the surface. This work claimed that adhesive force increased 25 times as the temperature was raised from 100°C to 400°C. Another source confirms the opposite trend; a six-fold decrease when the temperature was decreased from 400°C to 20°C [3]. In any case, these opposing results show the difficulty and variance in measuring adhesion phenomena. The substrate heating experiment was done in the following fashion. The chip was affixed with heat sink compound on a temperature controlled hot chuck, and placed under the microscope. As a last step in proving that meniscus forces were not the source of adhesion in our devices, the silicon nitride coated chips were annealed at 400°C for 3 hrs in order to remove surface moisture. No significant improvement was noted with the in-situ heating experiment or the annealing step.

3.4.4 Surface Metallization

With the failure of the capillary force experiments previously mentioned, the next attempt to improve the device performance was to experiment with thin (50Å) gold coatings on the silicon nitride insulated electrodes. If the particles were charged, this thin conductive coating might dissipate this surface charge on the particle. The gold layer was thermally evaporated on to the processed dies on which the bond pads were physically masked so that each of the three phases would still be electrically independent. Because of such a thin coating of gold, no chrome was pre-deposited for adhesion. This reduced the bond between the silicon nitride and the gold but was sufficient for this application. Next, transportation experiments were performed using frequencies from 1-10 kHz and voltages from 20-200V. The new metal layer was grounded for some experiments and set floating for others. However, the results were worse than before. Almost no movement at any voltage and frequency was noted. The low frequency electrical fields at which the particles did exhibit movement in prior experiments were shielded by the gold coating.

3.4.5 Mechanical Vibration

The particle chip was also tested on a piezoelectric stack in an attempt to understand if body forces could reduce the stiction force between the particle and chip surface. Previous work by Zimon shows that body forces created by gravity or centripetal acceleration can overcome adhesive forces for large particles. Although this mechanical method is difficult to incorporate into our type of device, it would aid in understanding of the nature of the particle to surface bond. Nevertheless, the chips were attached to a piezotransducer and vibrated at frequencies from 10 Hz to 20 kHz. The maximum detachment force can be calculated from Equation 3-1 where m is the mass of the particle, f represent the oscillation frequency, y the displacement, and g the gravitational acceleration. The displacement of the transducer was measured to be $\sim 2\mu\text{m}$ and the forces exerted on the $8\mu\text{m}$ silica particles were approximately calculated to be in 10^{-9}N range.

$$F_{\text{det}} = m (4 \pi f^2 y + g) \quad (3-1)$$

Testing was done for 5-15 μm particles with no improvement. From visual observation under a microscope, no detachment or horizontal motion of the particle from the surface was noted. These mechanical vibration experiments confirmed that the adhesive forces were greater in magnitude as in agreement with references [3,4].

3.4.6 Plasma Roughening

Increase in surface roughness has also been known to reduce particle adhesion [3]. Depending on the size of the asperities, adhesion can be increased or decreased. Figure 3-10 exaggerates the two possible scenarios: a) reduction of particle to surface contact area when the height of the asperities is less than the particle size, and b) increase in contact area when the particle is smaller than the height of the asperities.



Figure 3-10: Surface roughness effect on particle contact area.

Consequently, the resist surface was roughened with oxygen plasma (300W, 8min, 150mtorr) which changed the characteristics of the motion. The particles did not only move in the same direction of the traveling wave, but rather, in a random fashion. This effect was due to the large amount of negative charge implanted in the resist surface from the plasma, not the increase in surface roughness.

3.4.7 Dielectric Cycling and Aging Effects

To rule out time dependent polarization effects on both the particle and the silicon nitride surface, dielectric cycling experiments were performed. For the insulation layer, particle transportation experiments were performed with new dies where the nitride layer had not been exposed to the electrical fields beforehand. The motion characteristics were observed and then the three-phase circuit was turned on (200V, 20 – 10,000 Hz) and left connected the electrodes for 3 hours. Following this electrical cycling, fresh silica and polystyrene particles were dropped on the electrodes, and observed. No change in motion was observed. The particles exhibited the same pattern of initial movement and then stopping until voltage could not be increased further.

Experiments were also undertaken to ensure that the particles were given sufficient times to discharge if contact charging was taking place. Experiments were done until voltage could not be increased further. Then, the chip was left for 5 hours with the circuit turned off to give enough time for the particles to discharge. In our case, this waiting period with the circuit turned off proved ineffective, and particles that were stopped could not be moved again. This characteristic remained the same for both silica and glass particles although the relaxation time constants differed by orders of magnitude. From Jones [1] we can calculate the dielectric relaxation time constant of the particles. The formula is given below and the appropriate relaxation times are shown for silica and polystyrene particles.

$$t = \frac{\epsilon_2}{\sigma_2} = \frac{2 \cdot \epsilon_1}{2 \cdot \sigma_1} \quad (3-x)$$

Table 3-3: Relaxation times of particles

Particle type	Conductivity(S/m)	Dielectric constant	Relaxation time(s)
Silica glass	2.5×10^{-14}	5.8	0.069
Polystyrene	1×10^{-15}	2.5	780

The failure of this experiment did not, however, rule out the possibility of contact charging. Other research in the nature of particle charging points out that, in many cases,

particle discharge may take on the order of days [3]. Furthermore, as mentioned in Chapter 2, charged particles would create an image force between the charged particle and the electrodes. Consequently, if this were the case, how to eliminate or reduce this image force?

3.4.8 Photoresist as an Insulation Layer

One way to mitigate the effect of this image force (due to particle charging) was to increase the distance between the particle and the conductor. We saw from Equation 2-7 that the image force was inversely proportional to the square of the distance between the particle and the conductor. An easy way to increase this distance was to coat the electrode structures with different thicknesses of photoresist. To test this hypothesis, various thicknesses of AZ P4400 resist (Hoechst Celanese Corp.) were spun on and a series of experiments was performed for each thickness. The table below shows the spin speeds and the corresponding thicknesses (Table 3-4).

Table 3-4: AZ P4400 resist spin chart

Spin Speed (rpm)	Thickness(μm)
1000	9.0
2000	6.1
3000	5.2
4000	4.0

The final cross-sectional view of one of the complete electrode structures is shown in Figure 3-11.

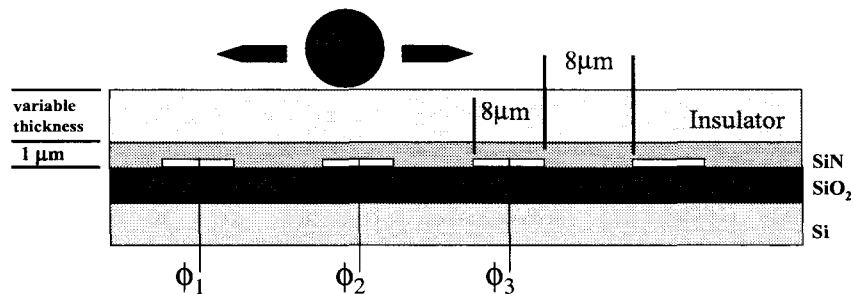


Figure 3-11: Electrode structure with additional insulation to reduce image force.

With the addition of a thicker insulation coating, particle transportation improved remarkably. Before, particles would stop after a few seconds of initial movement, but now, particles repeatably moved across the entire 3mm structure to the opposite side. Transportation efficiency for the photoresist insulated structures improved from 10% (for Si_xN_y) to 45%, and the threshold voltage decreased to 50V. Figure 3-12 below demonstrates that there was a distinct optimal thickness of insulation to maximize transportation efficiency.

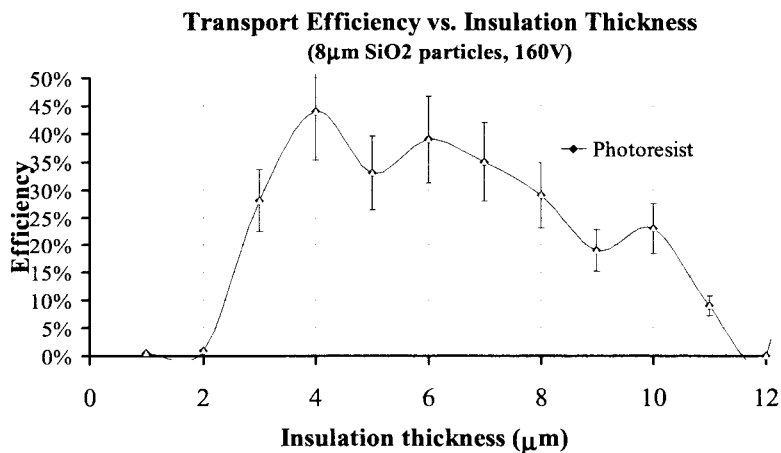


Figure 3-12: Evidence of an optimal resist thickness which maximized transportation efficiency.

This remarkable result was interesting considering the fact that the DEP driving force is greater the closer the particle is to the electrode panel and decreases if electrode to particle distance is increased. However, the DEP force also pulls the particle downward toward the substrate, increasing the adhesion. At some point the downward forces minimized but the horizontal component is sufficient to translate the particle across the electrodes.

3.5 2nd Generation Fabrication

Now, since the primary cause of the particle adhesion force had been identified, the next step was to further study electrode geometries and other insulators. The process for the second generation of electrodes was exactly similar to what is described previously. In this run, however, low temperature thermal oxide (LTO) and evaporated gold were used as the insulation and conductive layers, respectively. Various types of electrode

geometries were added into this second run. Parallel electrode structures were designed with $3\mu\text{m}$ electrode widths and spacings of 2, 4, 6, 8, 10, 15, and $30\mu\text{m}$. In addition, zig-zag and hexagonal electrode geometries were also fabricated (Figure 3-13).

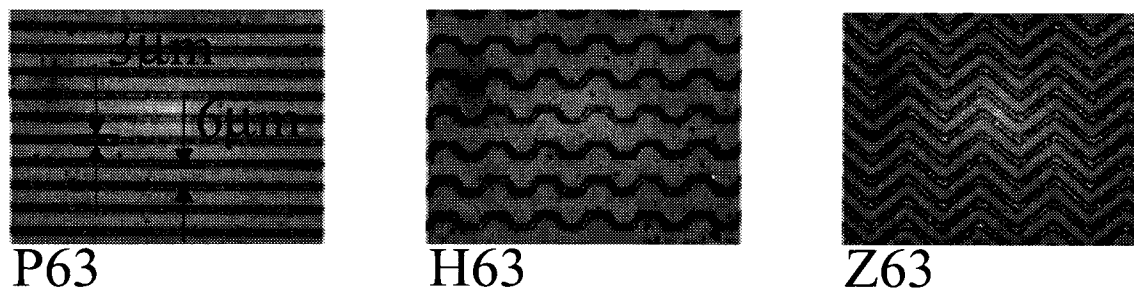


Figure 3-13: 2nd run of electrodes with $3\mu\text{m}$ width and different geometries

The reduction of electrode widths and tighter spacings (less than $3\mu\text{m}$) resulted in serious yield problems. About 80% of the structures were electrically shorted. This poor yield was the result of the following problems: a) dust particles during lithography, b) pinholes in the LTO insulation layer, c) undercut of the chrome-gold layer during the wet etch step, and d) the imperfections in the acetate films used to make the 10x chrome mask.

3.6 Spin on Teflon as an Insulation Layer

Because of the remarkable improvement by using an additional insulation layer, new experiments were done using the Dupont spin-on Teflon[®] film, AF1601. Discovered in 1938, Teflon films have been utilized since the 1960's as chemically inert non-stick layers and lubricative films. However, until recently, Teflon[®] had never been used in the fabrication of MEMS. Hsu et al. [5] demonstrated AF1601S qualities as a charge implantable thin film for MEMS applications. In our case, with its low coefficient of friction (.001), this Teflon film appeared an obvious substitute for the photoresist insulation layer. Available as a liquid amorphous copolymer of 2,2-bis(trifluoromethyl)-4,5-difluoro-1,3-dioxole (PDD) dissolved in tetrafluoroethylene (TFE), AF1601S is spun on just like photoresist. Because of their perfluorinated structure, this film, like other PTFE based materials, has excellent chemical resistance, low water absorption, and low surface energy. However, unlike PTFE, Teflon AF is amorphous, soluble at room temperature in several solvents, and is optically transparent. Table 3-6 shows the

thickness vs. spin speed after the 200°C, 3 hour hard-bake process in a vacuum oven. For thicker coats, a second spin step was performed after a 20 minute 100°C soft-bake. Some of the prominent properties are described in Table 3-5 below.

Table 3-5: Properties of Dupont Teflon® AF1601S

Thermal Stability	<360°C
Glass Transition Temperature	160°C
Dielectric Constant	1.93
Tensile Modulus	1.55 Gpa
Thermal Expansion Coefficient	74 x 10 ⁻⁶ /°C
Resistivity	10 ¹⁵ Ω cm

Table 3-6: A1601S Spin chart

Spin Speed (rpm)	Thickness (μm)
2000	0.78-0.80
3000	0.57-0.60
5000	0.44

Particle transportation experiments with Teflon® coated chips showed the highest particle efficiency. Maximum efficiency was as high as 90% using 8μm borosilicate glass particles with 8μm width and 8μm spaced electrodes. Like the photoresist insulated chips, the Teflon coated electrodes exhibited a similar optimal relationship between efficiency vs. film thickness. Table 3-7 summarizes the efficiencies and the threshold voltages associated with the different dielectric films. Specifically, for the Teflon, optimal thickness range was between 1-2 μm as shown in the Figure 3-14. For thicker Teflon coats, the efficiency begins to drop. The trend is seen at a height of 3μm, but data for 3+μm thicknesses is not shown.

Table 3-7: Linear electrodes $8\mu\text{m}$ spacing structure, $8\mu\text{m}$ glass particles

Surface Coating	Frequency Range (Hz)	Max Efficiency	Threshold Voltage (V)
PECVD silicon nitride	0.9 – 10	10%	80
AZ 4400	0.1 – 1000	45%	50
Teflon (AF 1601S)	1– 20,000	90%	40

Note: data has +/- 30% variation

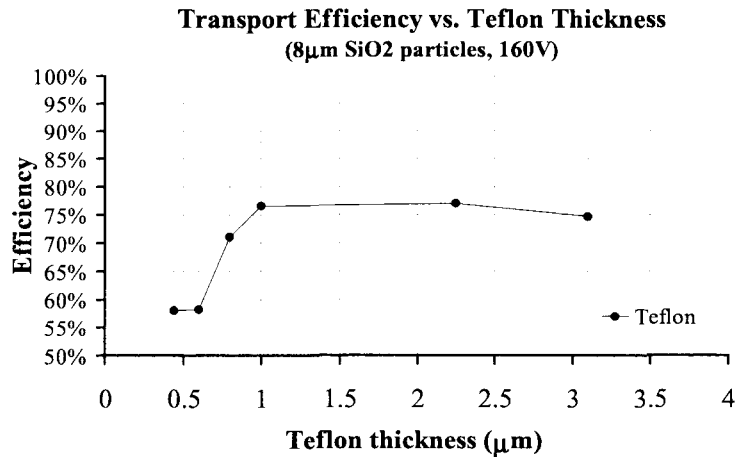


Figure 3-14: Transport efficiency vs. Teflon film thickness

In addition, as frequency increased the efficiency improved and then saturated. For photoresist, motion cut off at $\sim 1\text{kHz}$, and for Teflon motion was observed up to 20kHz . This frequency window could be explained due to the dynamics of particle movement. There was a finite time associated with particle stepping from one electrode to another. This time involved particle acceleration and deceleration from one electrode to the next. At the cut-off frequency, the particle was unable to keep up with the traveling wave.

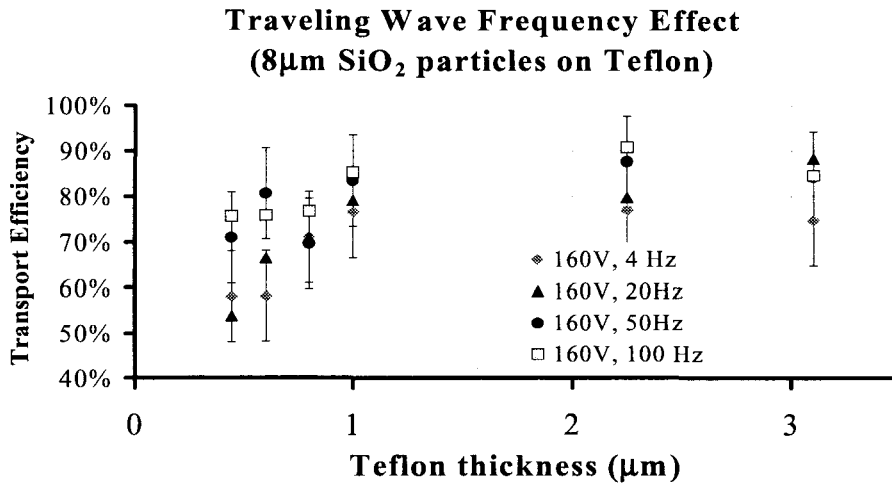


Figure 3-15: Transport efficiency as a function of thickness and different frequencies.

The electrode width and spacing was also optimized to increase transportation efficiency. In contrast to previous experiments performed with electrode width and spacing of 8 μm , Figure 3-16 shows the improvements resulting from decreasing the electrode width to 3 μm and the effect of varying electrode spacing. For the experiments in Figures 3-16 and 3-17, the frequency was kept constant at 10 Hz and two sets of experiments were conducted. One set of data was recorded at 100V (Figure 3-16) and the other recorded at 160V (Figure 3-17). The trials in this case were not done at the optimum frequency, but rather at 10Hz because it was easier to take accurate data. At higher frequencies, the particles moved so fast across the electrodes that over 70% got “thrown off” the chip. Figure 3-16 shows that 70% transportation efficiencies were achieved with only 100V and 10Hz. This performance improvement is solely due to the higher e-field gradients generated by the narrower electrode widths. In addition, as foreseen, both graphs revealed the decline of efficiency as the spacing between the electrodes was increased (for this size range of particles). This fact was also demonstrated in experiments with the radial electrode structures in which the particles only rotated at the innermost radius. At this radius, the electrode and spacing was 8 μm , and as the radius increased the spacing increased linearly to 30+ μm . Particle rotation speeds on the order of 60rpm were recorded. In short, the Teflon surface qualities coupled with the determination of an

optimal thickness resulted in the highest particle transport efficiencies for these microfabricated structures.

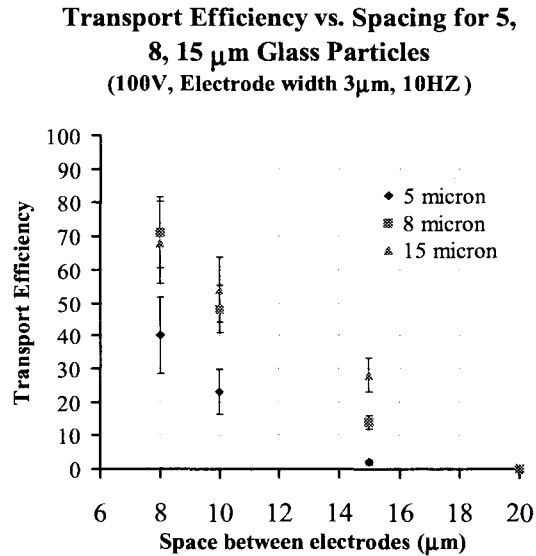


Figure 3-16: The effect of increasing electrode spacing on transport efficiency (100V)

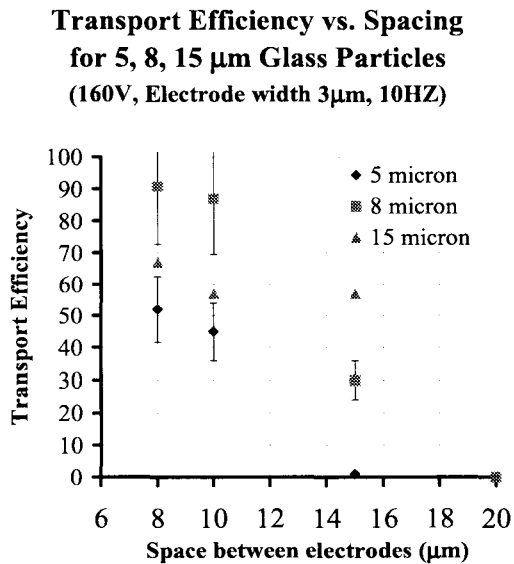


Figure 3-17: The effect of increasing electrode spacing on transport efficiency (160V)

3.7 Simulation of the DEP Force

In order to understand some of the trends in the experiments and to further optimize the electrode geometry, simulation of the dielectrophoretic force on the particle was performed using MAXWELL (Ansoft Corp.), a finite element (FEM) electrostatic simulation software. Due to the complexity of the DEP force equation, investigation of this phenomena has been primarily done using approximate methods such as the substitute charge method by Masuda *et al.* [6] and various levitational modes in which the particle is charged [7]. Many others have investigated DEP forces on biological cells in liquid media [8] [9]. Machowski *et al.* [10] have studied DEP separation efficiency on dry powders, but the electrode pitch and diameter were an order of magnitude larger than the our MEMS electrode panel.

Although one can easily compute complex geometries and their corresponding electric fields with adequate FEM software, the results are limited because of the difficulties in deriving adequate simulation parameters. For example, it has been explained in section 2.2.2 that particles do have surface charge distributions, but the magnitude may vary depending on a whole array of conditions. Also, because of the computational complexity and time required for 3-D simulations, most of the simulation results were generated with 2-D models where the position of the particle was stepped across the electrode panel while keeping the particle to electrode distance (height) constant. The DEP forces in the horizontal direction and vertical direction, F_x^D and F_y^D respectively, were calculated for each step. Furthermore, the simulation was performed using a single *uncharged* particle on the electrode panel without nearby particles so that trends could be discerned. Note that the number of electrodes in the model were between 15-20 because it was iteratively determined that electrodes further away had negligible effect on the particle force. Parameters for the materials are given in Table 3-8 .

Table 3-8: Simulation parameters

Material type	Conductivity (S/m)	Relative Permittivity ϵ_r
Air	0	1
Aluminum	3.7×10^7	1
Borosilicate glass	-	5.8
Si_doped	66	12
Photoresist	-	4
Silicon nitride	10^{-14}	7

Using the 2-D Maxwell solver, DEP x and y forces on a single, uncharged $8\mu\text{m}$ glass particle (at zero height) have been plotted with respect to electrode position (Figure 3-18). The circles represent the x-component of the force and triangles represent the y-component. $8\mu\text{m}$ electrodes (and $8\mu\text{m}$ spacing) with their corresponding voltages have been drawn on the x-axis. The force is shown on the vertical axis in N/m since this is a 2-D model. For the most part the 2-D model is sufficient in depicting trends such as variation of force with electrode spacing, width, etc. This simulation showed that the DEP driving force not only generates the horizontal force, which moves the particle, but a much larger downward force as well. The simulation also confirmed the periodic characteristic of the forces due to the three-phase electrode scheme.

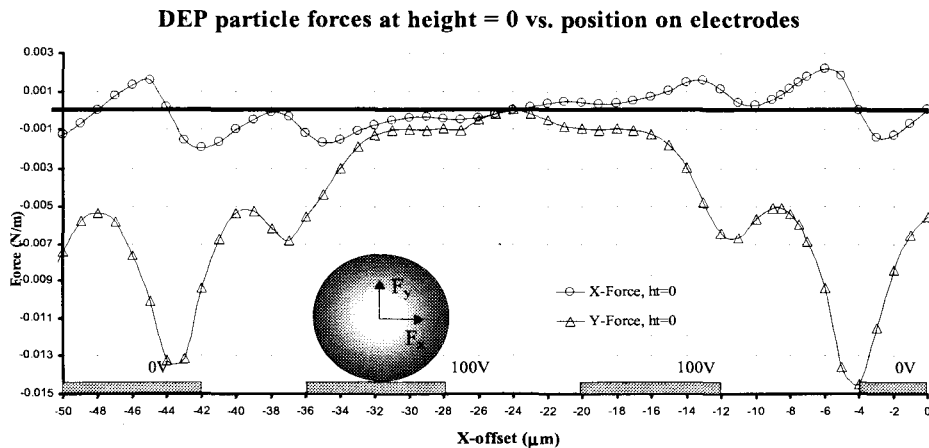


Figure 3-18: DEP forces vs. particle position

For the same 2-D model above, simulations were conducted for various particle heights above the electrodes. Figure 3-19 verified the expected reduction of both x and y components of the DEP force as the particle was moved further above the electrodes. The darkened simulation points are for particle to substrate (electrode) distance of $1\mu\text{m}$ and the clear points represent the particle $2\mu\text{m}$ above.

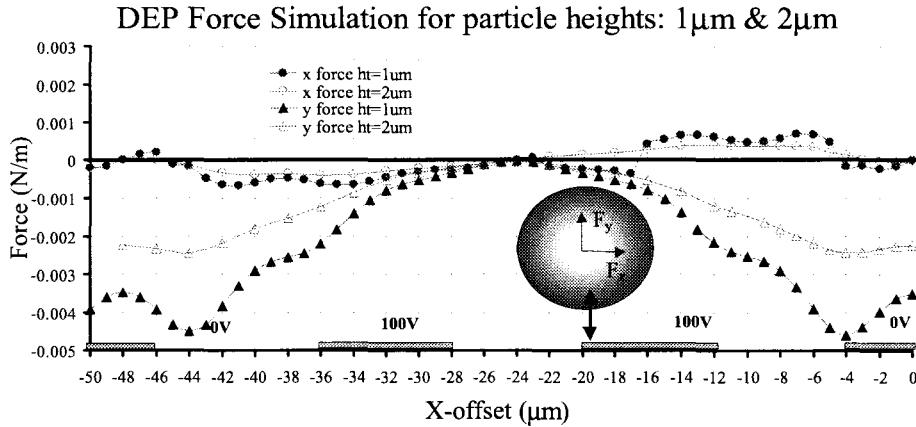


Figure 3-19: DEP force decreases with increase in particle height from electrodes

A 3-D simulation confirmed the same force trend as for the previous 2-D case. In this case, the particle is located at a height of $3\mu\text{m}$ above the electrodes. The irregularity of the curve in the graph stems from the discreteness of the simulation mesh.

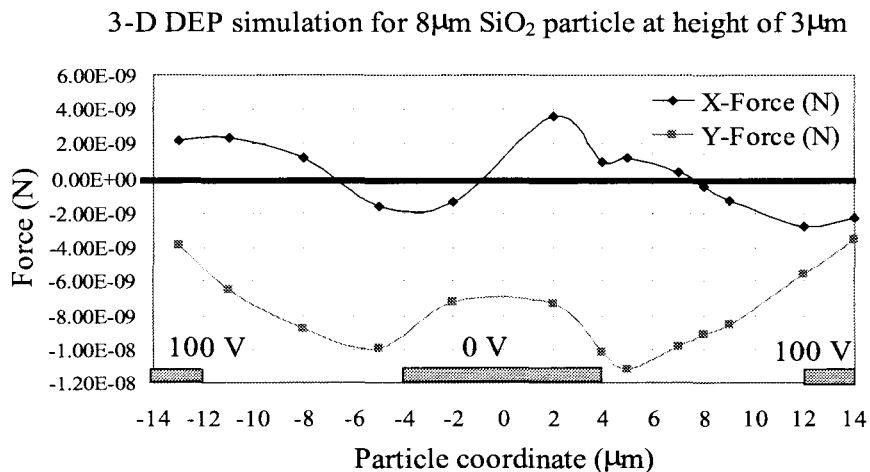


Figure 3-20: 3-D simulation of particle DEP force

The effect of changing electrode pitch and width was also analyzed. Figure 3-21 and Figure 3-22 below show that as electrode pitch was increased, the available DEP force in both x and y directions reduced. For this simulation, the electrode width and the test particle were kept constant at $8\mu\text{m}$.

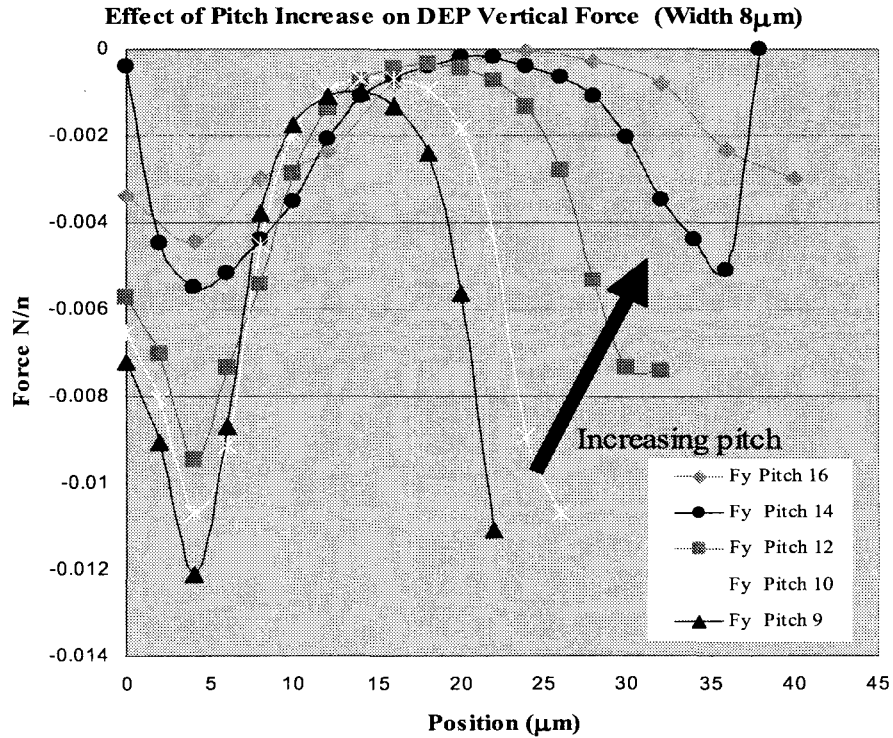


Figure 3-21: DEP force in Y-direction is reduced when electrode pitch is increased

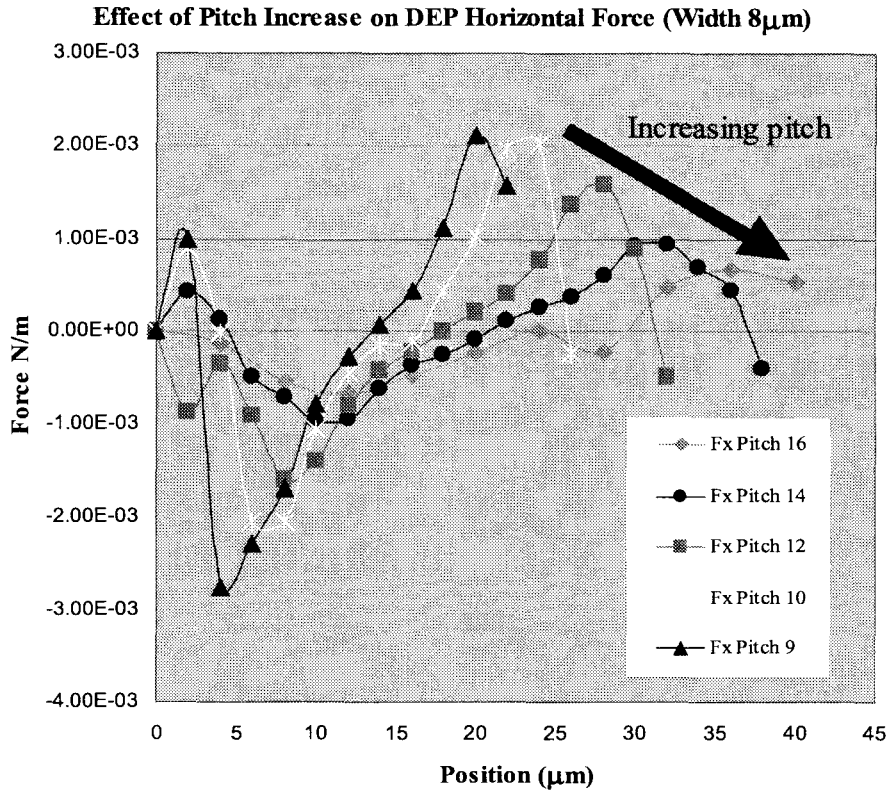


Figure 3-22: DEP force in X-direction is reduced when electrode pitch is increased

In addition to simulating various electrode geometries, the effect of the image force and various insulation permittivities were also investigated. In simulating the interaction of a charged particle with the unpowered electrodes, a charge of 9×10^{-7} C/m which corresponds to 10^{-16} C per particle was assumed because of the large variance reported in literature. Nonetheless, the FEM simulation enabled confirmation of the hypothesis. Figure 3-23 clearly showed that the vertical component was greater when the particle was directly above the electrodes (with no driving voltage in this case), and also shown was the reduction of image force as the particle height is increased. The electrodes were located between 0 and $-4\mu\text{m}$, and -12 and $-16\mu\text{m}$ which completed a full period (for the unpowered electrode case).

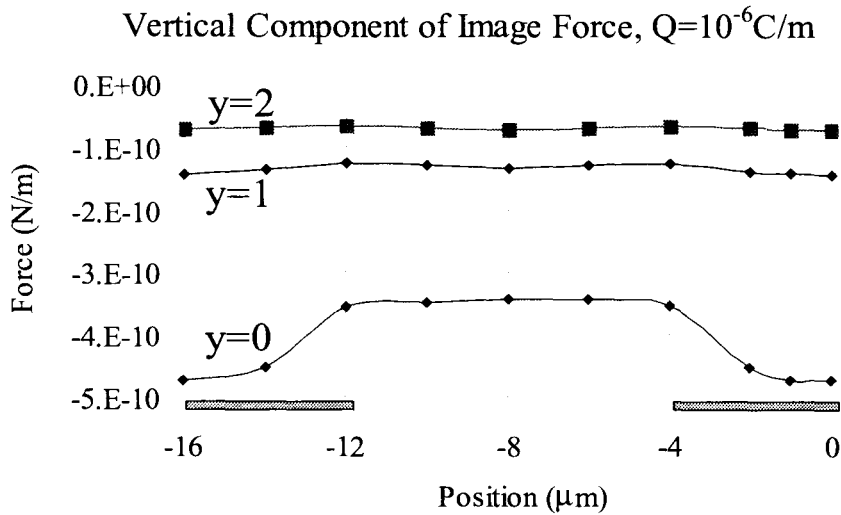


Figure 3-23: Simulation of particle image force for various heights above the electrodes.

For a given particle position, simulations were performed for insulation films with different dielectric constants for a fixed particle position (x and y fixed). Figures 3-24 and 3-25 show that the x and y components of force increased with increasing dielectric constant initially, and then begin to saturate as the relative dielectric constant of the film approached 8. The graphic inside the figure shows the 3-y axes and the position of the $8\mu\text{m}$ particle on the electrodes at $x=-7\mu\text{m}$. This result explains the benefits of utilizing insulative films with the same surface qualities (low stiction) like AF Teflon ($\epsilon=1.93$) and AZ photoresist ($\epsilon=4.00$), but with larger dielectric constants.

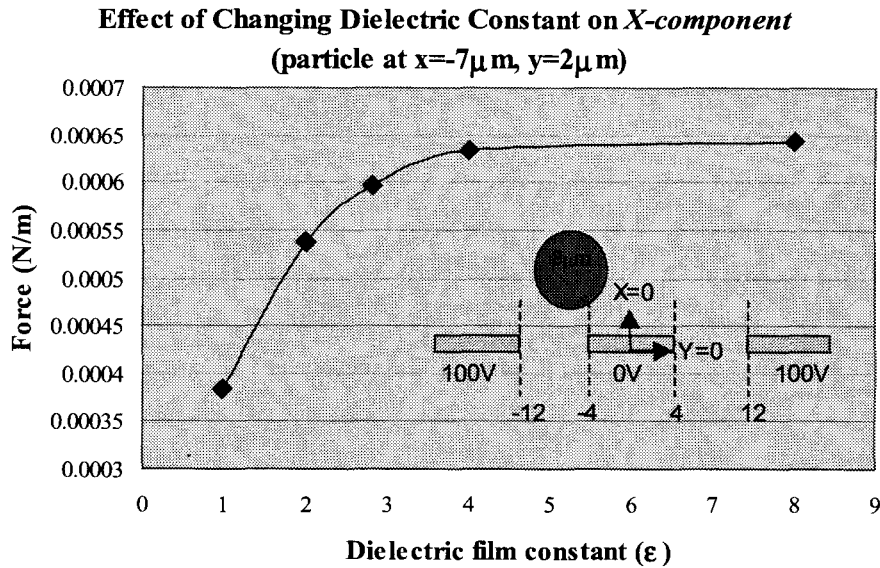


Figure 3-24: DEP horizontal force increases with larger dielectric constant

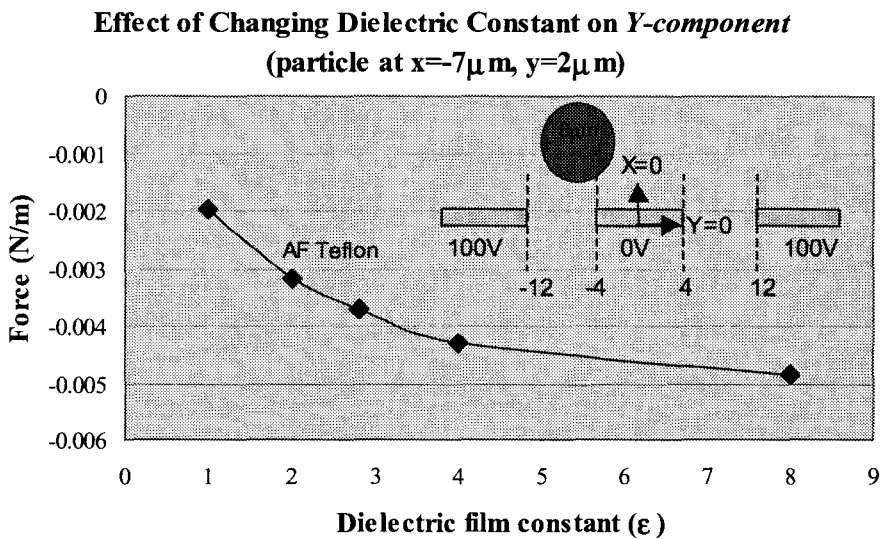


Figure 3-25: DEP vertical force increases with larger dielectric constant

3.8 Discussion

Understanding the interaction between the DEP forces and adhesive forces on the particle is the key to interpretation of the experimental observations. From the experimental

observations, the image force contribution appears to be the dominant adhesive force; consequently, decreasing this image force, F^I , leads to higher transportation efficiency. As stated in Chapter 2, the image force arises when particles are charged and are in close proximity to a conductor. In fact, the presence of an optimal thickness with the insulative films supports this hypothesis, because F^I is reduced when the distance from the particle to the electrodes is increased. To simplify this discussion of the various forces, 3-26 accounts for each type of force, acting on the particle. The quantities in parentheses represent what the force is dependent on. For the MEMS structures presented here, analytical expressions for the forces and their respective x and y components are difficult. Nevertheless, a list of equations for simple particle to surface interactions and references is provided in the Appendix.

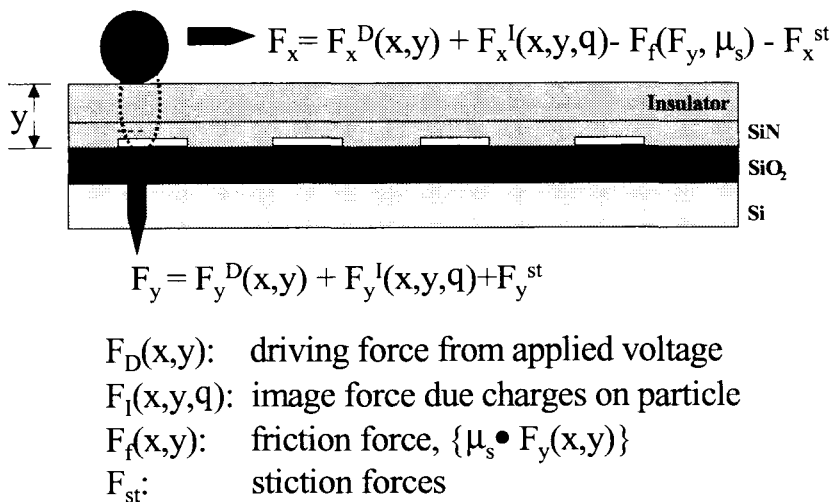


Figure 3-26: Schematic of particle forces

The downward force on the particle, F_Y , arises from three sources: the image force, F_y^I , the stiction force, F_y^{st} , and also the y-component of the DEP force, F_y^D . The horizontal force, F_X , can be separated into four parts: 1) the DEP force, F_x^D , 2) F_x^I , the 3-component of the image force, 3) the frictional force, F_f , and 4) F_x^{st} . However, F_f is inherently related to F_Y through the frictional coefficient, μ_s . Because of this relationship, any change in insulation thickness also has an effect on the net horizontal force on the particle.

Proof of these downward forces on the particle, F_y^D and F_y^I were computed using Maxwell in Figure 3-19 and Figure 3-23, respectively. From Figure 3-19, we saw that although the horizontal or X-component of the DEP force, F_x^D , due to the voltage waveform was responsible for particle transport, the DEP y-component, F_y^D , acted downward thus adding to the frictional force. In other words, the DEP force not only exerted a horizontal force but a downward force as well. Likewise in agreement with electrostatic theory, Figure 3-23 showed that F_y^I diminished as the particle height from the electrodes was increased, and it was greatest when the particle was directly above the electrode. Superposition of these forces (image, DEP, and stiction) then gives us total downward force.

The FEM results corroborate the phenomena observed in experiment. In our experiments variation of this distance (between the particle and the electrode), which was controlled by the thickness of the insulation film, clearly affected the performance. If the insulation was too thin, the downward forces dominated and efficiency dropped. If the insulation film was too thick, the driving force was not sufficient enough to overcome the adhesive forces. Therefore, at a specific thickness, F_x was maximized and thus gave the highest transportation efficiency. However, each insulation film had its own optimal thickness (Figures 3-12 and 3-14) because Van der Waals, meniscus forces, and frictional coefficients between the particle and the insulation surface differ from film to film. In addition to this complexity, the FEM simulations of varying pitch point to the fact that as electrode pitch was increased, the DEP force dropped (Figure 3-22). However, if pitch was decreased too much, then the image force became greater and greater because the electrodes looked more like a solid sheet (as shown below) (Figure 3-27).

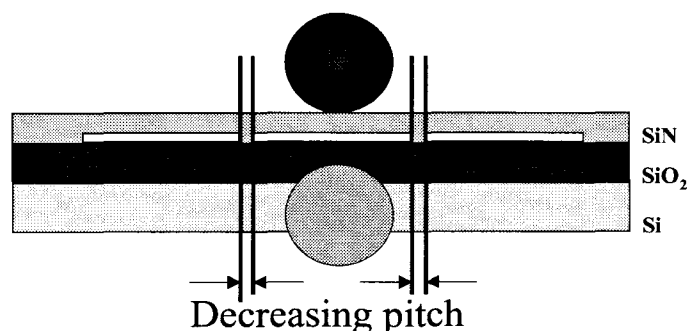


Figure 3-27: Decreasing pitch resulted in higher image force contribution.

3.9 Conclusion

In contrast to the work done in the past in this field, this work shows that it is possible to move μm -sized particles in air. It has been shown that particles of 5-10 μm size range can be manipulated electrostatically with voltages below 200V in a standard room environment. Because of the interrelationship of the image force, the DEP force, friction, electrode geometry, and particle charge, we see that simulation of all the particle forces is complex. Thus, many of these critical parameters are difficult to measure, and other researchers have substantiated the large variability in adhesion characteristics. In our case, by performing a multitude of experiments designed to isolate and investigate the different types of particle to surface forces, we have determined that particle charging is a significant cause of adhesion on our MEMS transportation system. More importantly, we have discovered a simple way to reduce its negative effect on particle transportation performance, and have demonstrated an effective means (90% efficiencies) of transporting particles on a substrate in a standard dry environment. With this knowledge of the transportation characteristics, we propose to demonstrate applications, such as active filters and liquid interfaces, with which this MEMS transportation system can be combined. The next chapter illustrates this application.

References

1. T.B. Jones, *Electromechanics of Particles*, Cambridge University Press, New York, 1995.
2. Anderson, R., Larson, G.L., and Smith C., *Silicon Compounds: Register and Review*, 5th edition, Huls America, New Jersey, 1991.
3. A.D. Zimon, *Adhesion of Dust and Powder*, Consultants Bureau, New York, 1982.
4. C.N. Davies, *Aerosol Science*, Academic Press, London and New York, 1966.
5. T. Hsu, W.H. Hsieh, K.Furutani, and Y.C. Tai, "A Thin Film Teflon Electret Technology for Microphone Applications." Hilton Head 1996 Solid-State Sensor & Actuator Workshop.
6. Masuda, S. and T. Kamimura, "Approximate Methods for Calculating A Non-Uniform Traveling Field," 1975 *Journal of Electrostatics*, Vol. 1, pp. 351-370.
7. Gan-Mor, S. and Law, E.S., "Frequency and Phase-Lag Effects on Transport of Particulates by an ac Electric Field," 1992 *IEEE Transactions on Industry Applications*, Vol.28, No. 2, pp. 317-323.
8. Hughes, M.P., Pethig, R., and Wang, 3-B, "Dielectrophoretic forces on particles in travelling electric fields," 1996 *J. Phys. D: App. Phys.*, Vol. 29, pp. 474-482.
9. Morgan, H., Green, N. G., Hughes, M. P., Monaghan, W., and Tan, T.C., "Large Area travelling-wave dielectrophoresis particle separator," 1997 *J. Micromech. Microeng.* Vol. 7, pp. 65-70.
10. Machowski, W., Balachandran, W., SMIEEE, and Hu, D., "Influence of Electrode Geometry on Transport and Separation Efficiency of Powders Using Travelling Wave Field Techniques," *IEEE*, pp. 1508-1513.
11. A. Desai, S. W. Lee, and Y.C.Tai. "A MEMS Electrostatic Particle Transportation System." *The Eleventh Annual International Workshop on Micro Electro Mechanical Systems (MEMS '98)*, Jan 1998.
12. A. Desai, S.W. Lee, Y.C. Tai. "A MEMS electrostatic particle transportation system." *Elsevier. Sensors & Actuators A-Physical*, Vol. A73, no.1-2, pp. 37-44. Switzerland, 9 March 1999.

Chapter 4

Particle Collection from Air to Liquid

4.1 Introduction

As pointed out in the introduction of this thesis, currently there is a growing need for a hand-held automated environmental detection system for detection of bio-aerosols such as toxins, viruses, and spores. Successful detection of these types of particles requires three steps - collection, transport, and analysis. For airborne particles, collection and transport typically occur in the air environment, but the third step, analysis, becomes a problem because many of the sensitive bio-analytical techniques (such as fluorescence, DNA analysis, etc.) only work in the liquid medium. Consequently, engineering of an air-liquid interface is required to transport the collected particles from air to into liquid. In the past, the transport of particle into a liquid medium has been done primarily by manual pipetting and washing. Other large-sized automated systems have employed liquid wash steps where the collected particles of washed off a denuder [1], or a cyclone chamber. However, these types of traditional techniques become impractical for such a hand-held system with microliter fluid volumes and without conventional mechanical valves and pumps.

In this chapter, a solution to this interface problem was engineered and integrated with the MEMS particle transportation technology developed in Chapter 3. The first generation design consisted of a glass chip with channels bonded to the electrodes. The focus here was to design hydrophobic channels small enough so that the surface tension forces would prohibit liquid leakage outward, but allow particles to be transported across the air-liquid interface. After discovering problems with this first scheme, the interface problem was tackled with a different approach. In this second approach, instead of moving particles and a stationary interface, we demonstrated a working particle-to-liquid collection mechanism with a *moving meniscus and stationary particles*. The feasibility

of this technique was applied together with a micromachined active membrane filter fabricated by Lee *et al.* [2]. Although particle transport efficiency decreased greatly on the filter surface, the feasibility for an airborne particle sampling system was demonstrated. Some of the issues explored in this chapter are the following:

- 1) Stability of the air-liquid interface
- 2) Control of the fluid meniscus
- 3) Performance of the transportation scheme in liquid
- 4) Integration of particle transportation technology with a fluidic interface chip and an active micromachined membrane filter.

4.2 First Generation Interface Design

The concept for the particle interface design is shown below in Figure 4-1. The glass chip (shown on top in the Figure 4-1) contains etched channels which simulate a liquid system in which the particles could be distributed and analyzed. The three “T” channels (shown as dashed lines) containing the liquid meniscus interfaces are connected to a larger central channel in which liquid is flowing. Using the DEP force, the particles would be transported from the electrode across the interface into the bulk liquid.

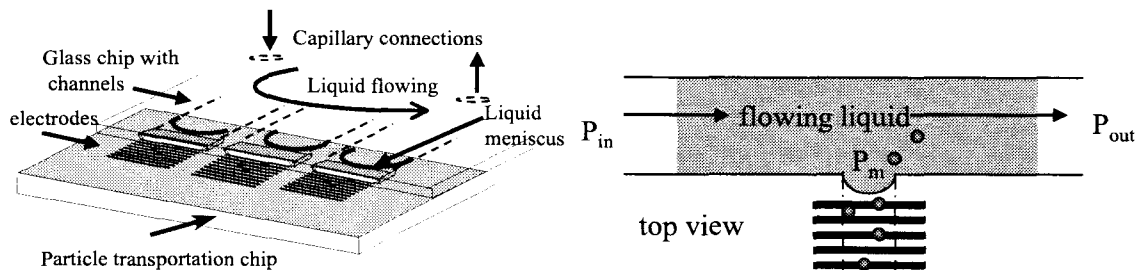


Figure 4-1: 1st Particle air to liquid collection scheme (L) and schematic (R)

DEP control of particles in liquid has been demonstrated by [2] [3] [4] who have shown that in contrast to the high voltage low frequencies required in air, low voltages and high frequencies are required for particle transport in liquid. In fact, particle motion in liquid has been shown to be much more robust and efficient than in air. Table 4-1 illustrates the different regimes demonstrated by various groups. In our case, two circuits were connected to the electrodes so that when the particles entered the liquid, the proper waveform (circuit) would be activated.

Table 4-1: DEP electrical requirements for different media.

Reference	Voltage	Frequency	Medium
This work	100-200V	5 – 100 Hz	Air
Fuhr <i>et al.</i> [3]	1-5 V _{pp}	1 Mhz	Conductive liquid (10mS/m)
Lee <i>et al.</i> [4]	120-140V	1-1000Hz	Corn oil (10 ⁻¹¹ S/m)
Morgan <i>et al.</i> [5]	10V _{pp}	500kHz	Conductive liquid (150mS/m)

To work, this scheme requires that the midstream pressure, P_m , of the flow at the interface be less than the capillary pressure, P_c . The governing aspects of this design are the Young-Laplace and the Hagen-Poiseuille equations [6]. From the Young-Laplace equation we are able to predict the maximum pressure that can be present near the opening. Similarly, the Poiseuille equation helps us predict the pressure drop in the central channel for a given flow rate. The Young-Laplace equation, Equation 4-1, is a function of the surface tension of the fluid, σ , the capillary radius, r , and the meniscus contact angle, θ . Assuming the meniscus is a section of a spherical surface that intersects the capillary at a finite contact angle, we have the static case [7],

$$P = (2\sigma/r) \cos(\theta). \quad (4-1)$$

Though Equation 4-1 is valid only for circular openings, it is sufficient to demonstrate the features of this design. The elaborate closed form solution for our case, a rectangular slit has been derived by Kagen and Pinczewski [8] in a lengthy derivation. They show that closed form solution for the pressure, P , for the rectangular slit falls below that for the circular channels. Consequently, the Young-Laplace equation represents the “best case” solution. To better understand the maximum possible interface pressures, Equation 4-1 has been plotted in Figure 4-2 for pure water and a highly hydrophobic capillary wall ($\theta \sim 180^\circ$).

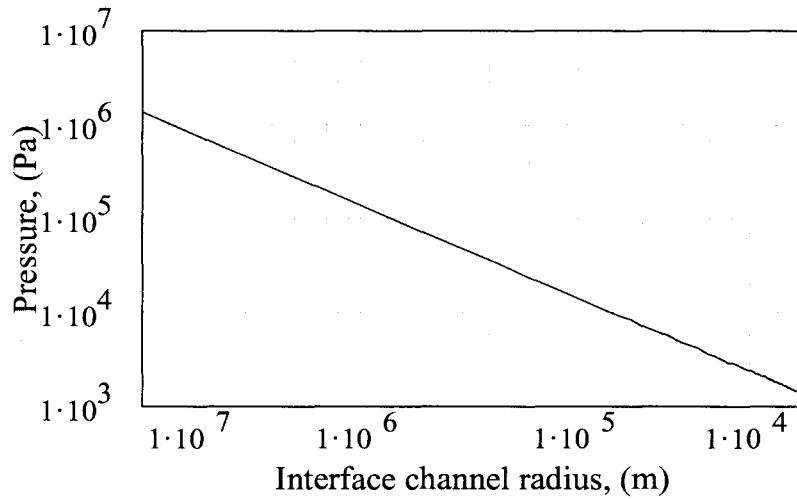


Figure 4-2: Maximum meniscus pressures for water vs. interface channel radius.

The Poiseuille flow equation relates flow rate, Q , to the pressure drop, ΔP , the pipe radius, r , viscosity, μ , and the distance from the interface to the exit, L .

$$Q = \Delta P \pi r^4 / (8 \mu L) \quad (4-2)$$

Substituting Equation 4-1 for ΔP in Equation 4-2 and making the following assumptions, we can estimate the best case flow rates possible for given interface channel sizes. The following values, 5mm and 50 μ m, were chosen for L and r , respectively. Note that Figure 4-2 represents an ideal case, where the contact angle is 180°, the interface channel surface is perfectly smooth and clean, and the interface channel is circular. In our case, the channels are rectangular slits. Furthermore, the exit pressure due to external piping and constrictions due to the connection is probably much greater than estimated. Therefore, we expect the order of the allowable flow rates to be correct, but certainly two to three times lower than these idealize flow rates shown in Figure 4-3.

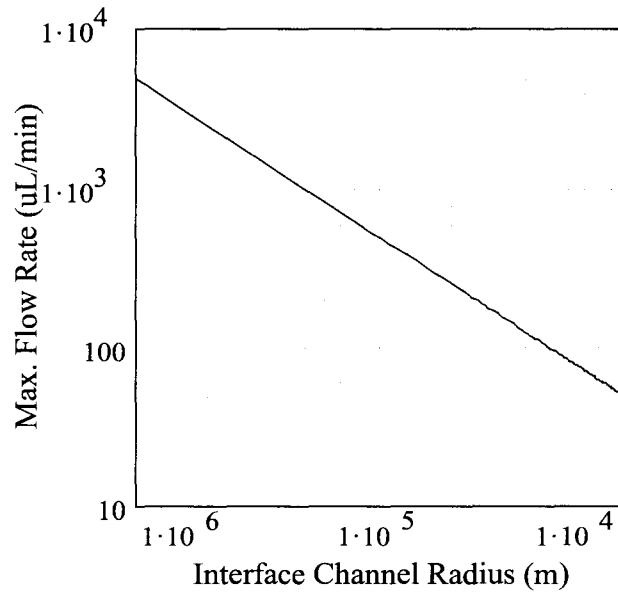


Figure 4-3: Idealized flow rates possible for given interface channel sizes

4.3 First Generation Interface Chip Fabrication

Fabrication of the interface chip requires two glass etching steps to create the deeper central flow channel and the shallower interface “T” channels. Evaporated gold acts as the masking layer and buffered hydrofluoric acid (BHF), as the etchant. Photographs of various designs are shown in Figure 4-4. The designs have curved, tapered, and widened channel entrances to study which types can sustain the fluid meniscus and which types capture more particles.

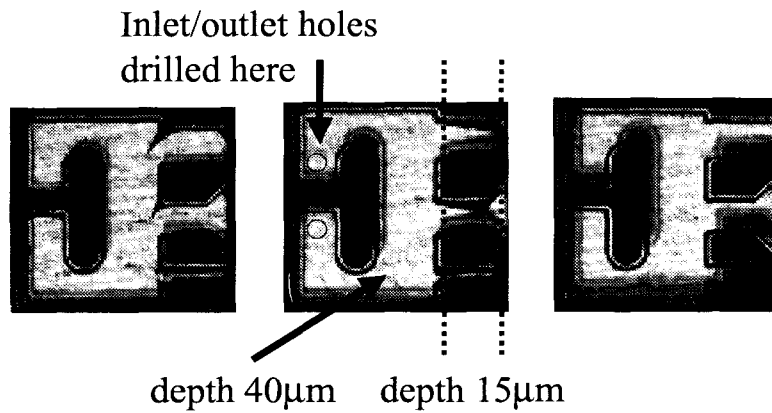


Figure 4-4: Various glass interface channel designs

The process steps are shown in Figure 4-5. First, 800Å of Au is thermally evaporated onto the wafer which is already patterned with photoresist. Next, the resist is “lifted-off” with acetone leaving behind the gold masking layer. More photoresist is spun and patterned to mask the interface channel while the other areas are etched to 15µm. The resist is removed with acetone and etching is continued to the desire depth. The etch rate of the glass in BHF is roughly 1µm/min. Inlet and outlet holes are drilled mechanically with a 700µm diameter drill bit.

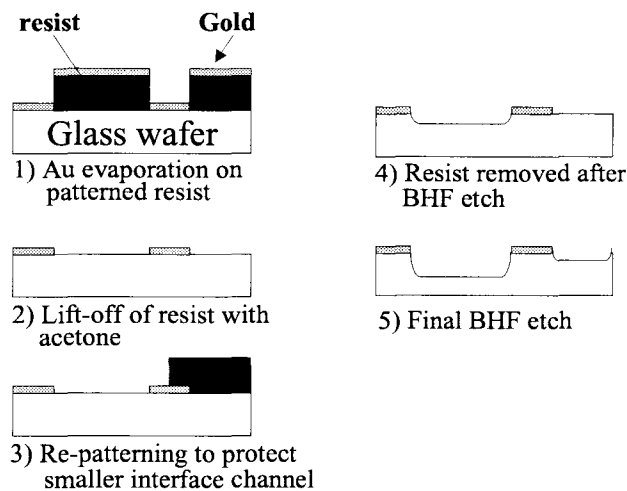


Figure 4-5: Glass interface channel fabrication steps.

To make the interface channels hydrophobic, a Teflon-like polymer film was plasma deposited as the final step. In the past, flourine-based gases have been utilized in plasma processing for their ability to selectively etch silicon. But, under certain conditions these gases can be polymerized to form thin films on a substrate. For the interface chip, the fluorocarbon gas, CHF_3 , was polymerized in the plasma at the following conditions: 170W 300mTorr, 2.7µm/hr [9]. Resistant to acetone, hydroflouric acid, and alcohol, this “plasma teflon” coating is stable. However, special care had to be taken to pre-clean the surface before deposition because of the weak plasma teflon adhesion to the substrate. In addition to the CHF_3 film, hexamethyldisilazane (HMDS) vapor treatment was also used to make the glass surface hydrophobic. Selective deposition of the hydrophobic films only in the interface channel area was done with a physical mask because any type of

photoresist processing such as developer and acetone rinsing destroyed the hydrophobicity of the polymer film surface (AZ4400 and AZ developer).

After correct priming of the channel surfaces, the interface chip was bonded to a glass slide for the initial experiments (Figure 4-6). The inlet pipe was connected to a digitally controlled syringe to simulate a micromachined liquid pumping system. The interface chips were bonded to a particle transportation chip, Figure 4-7, after suitable control of the meniscus was achieved. In addition, the particle transportation chip had to be redesigned to include large 5 x 3 mm electrode arrays, and adjacent dies on either side were left blank to leave room for bonding the liquid channel chip.

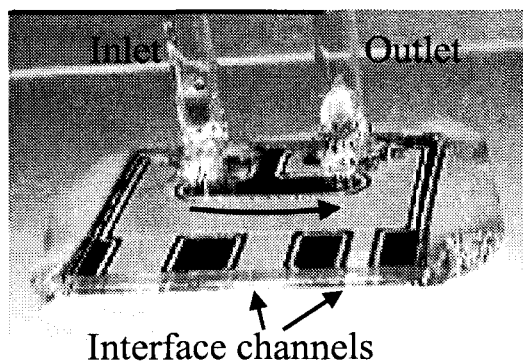


Figure 4-6: 1 cm x 1 cm glass interface die bonded to a glass substrate for initial testing.

The glass die was bonded onto a particle transport chip using the spin on the Dupont AF1601 for two purposes - as the bonding material, as well as the optimized dielectric spacer in one step. No modification to coating procedure was necessary. Both the pieces were aligned and clamped together before the 200°C hard-bake. Some devices were prone to cracking due to the thermal mismatch of the spin-on Teflon and the glass; in effect, proving the efficacy of the bond.

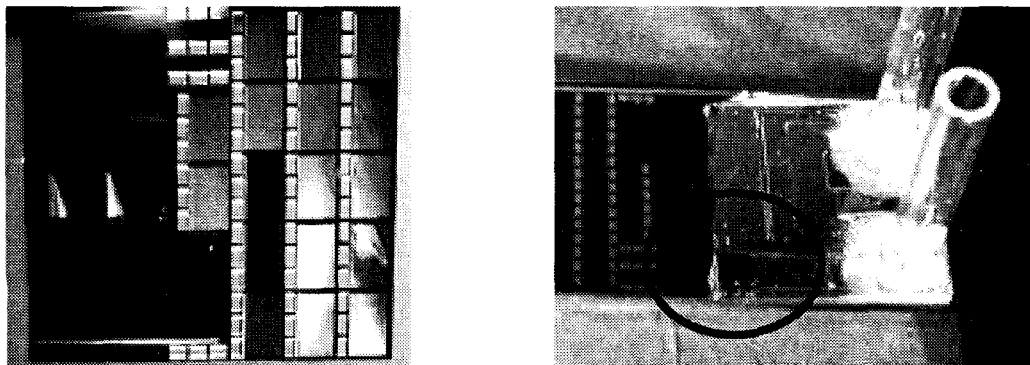


Figure 4-7: Glass interface die (R) bonded to a particle transportation chip (L).

4.4 First Generation Interface Experiments and Discussion

The first experiments with just the interface die bonded to glass proved to be difficult. The epoxy bonding step was problematic and decreased yield. Experiments were conducted by slowly increasing the flow rate until the meniscus broke down for various coatings (bare glass, HMDS, and the CHF_3 fluoro-polymer). As expected, uncoated interface channels only withstood flow rates on the order of 0.1-1 $\mu\text{L}/\text{min}$. The more hydrophobic the interface, the higher the flow rate achieved. For example, the silane coated dies attained flow rates on the order of 1-5 $\mu\text{L}/\text{min}$, and the CHF_3 Teflon dies could withstand flow rates of 50-100 $\mu\text{L}/\text{min}$. Observations showed that the fluid meniscus was only stable for ~ 30 min. Once the surface had been contaminated, the level of hydrophobicity decreased, the chip would fail. Furthermore, the position of the meniscus was hard to control. Nevertheless, the next step was to experiment with working electrodes and moving silica glass particles.

Experiments with the combined electrode and interface chips proved to be failures for two reasons. Firstly, particles transported in air on the electrodes could not travel past the liquid meniscus, and conglomerated at the boundary (Figure 4-8). Secondly, the high voltage required for particle transportation in air caused electrolysis of the water present on the electrodes - even though the electrodes were well insulated by LTO and Teflon. The bubbles in the water would form within minutes and destroy the electrodes. This result made it clear that during the high voltage, low frequency transportation, no water

could be present on the electrodes. The voltage required turned out to be an order of magnitude higher than the voltages demonstrated in prior work in this field (Table 4-1). 50V at 500Mhz were required to move the silica particles in water in our system.

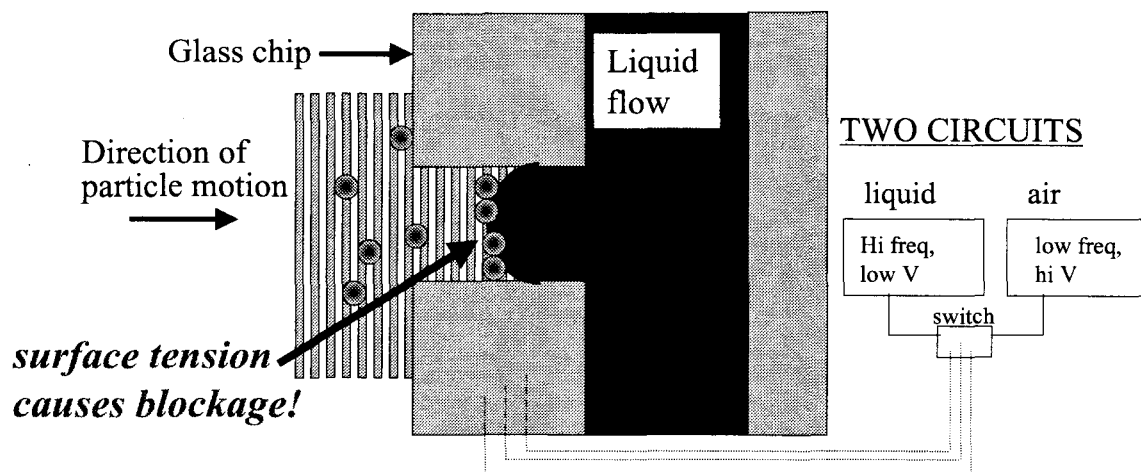


Figure 4-8: DEP force in air not enough to cross liquid meniscus.

Although this meniscus based interface design failed to work, valuable information on properties of surfaces, stability of air-liquid interface, and the performance envelope of the DEP force was acquired. The CHF_3 Teflon-like film was the most hydrophobic, and as expected, the highest flow rate ($100\mu\text{L}/\text{min}$) was achieved for the $15\mu\text{m} \times 1\text{mm}$ which was three times slower than for the idealized case (see Figure 4-3). Because of the rectangular channel, and unaccounted exact pressure drops in the outlet side of the chip, we expected this slower flow rate. On the other hand, the DEP scheme in both environments, air and water, on the same set of electrodes proved unfeasible. From the observations, it was clear that the water could not be exposed to the high voltage, low frequency scheme needed for particle transport in air. Moreover, even if the electrolysis problem could be solved, the DEP force was insufficient to force the particles through the fluid meniscus. A different solution was needed.

4.5 Second Generation Interface Design

Because of these two obstacles, a different approach was taken to transport the particles across the air-liquid interface. Since the DEP force was insufficient to provide the penetration force, the energy of a moving meniscus was used instead. Initial experiments using a water droplet to “capture” particles off the electrodes showed promise. The water droplet was attached to a fused silica capillary (150 μm ID) and positioned so that the droplet rested on the Teflon coated transportation chip (Figure 4-9). Because of the two dissimilar surfaces (the hydrophilic capillary tip and the hydrophobic chip surface), the droplet remained firmly attached to the capillary tip while the tip was “scanned” across the surface of the particle chip. Almost every particle that contacted the moving droplet was captured inside.

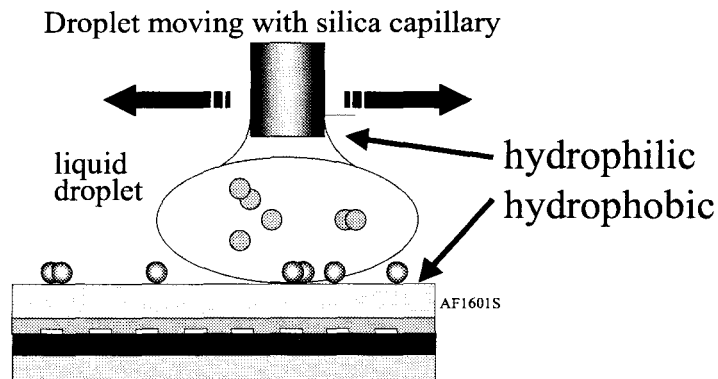


Figure 4-9: Particle collection experiment with a moving droplet

With success of this initial test, the 2nd generation interface was designed with a moving meniscus controlled by conventional pressure driven pumping and sucking. Unlike the original scheme, the particles are collected in a three-step mode shown in Figure 4-10. With this technique, the circuit (high voltage, low frequency) is turned on until particles are transported inside the interface channel. Then, the power is turned off, and the meniscus captures the particles in a back and forth motion. In step three, the meniscus is sucked back so that no liquid is present on the electrodes, and the electrode circuit is turned back on. This cycle is repeated. In the demonstration, here, the pumping and sucking was done manually to illustrate the concept; though in the future, one could envision integration with micro-pumps and valves. Furthermore, an active filter was integrated onto a section of the particle transportation chip to for demonstration purposes.

The active filter was a modification of the electrode fabrication process described previously but with backside wafer processing to realize the electrodes on a silicon filter membrane. Figure 4-11 shows a new transportation chip layout (1cm x 1cm) redesigned with large array of various electrodes and filter areas with their respective sizes. To increase collection efficiency (with respect to the linear arrays), the radial electrodes, depicted here, serve as particle concentrators – grouping the particles in one central area. The first number in the label (“R” or “P”) refers to the electrode width, and the second number refers to the space in between the electrodes.

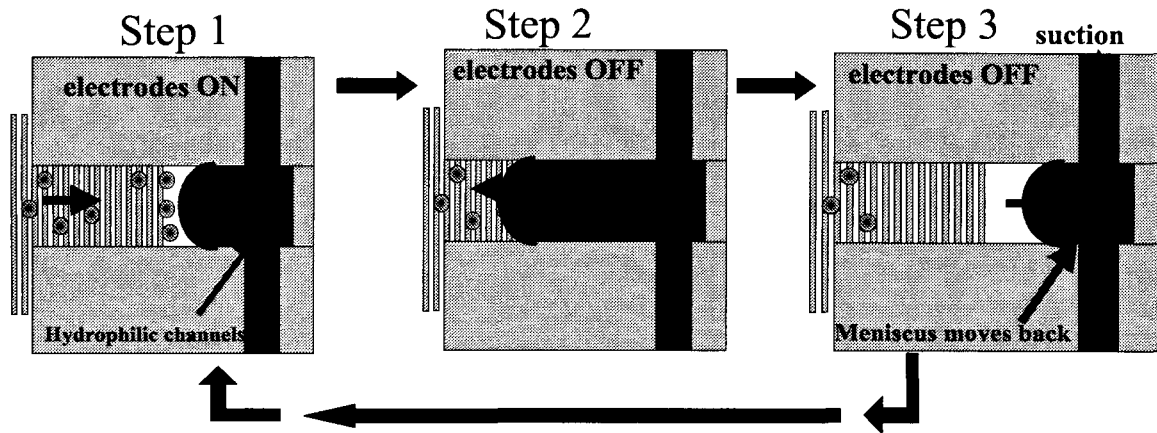


Figure 4-10: 2nd generation particle collection scheme

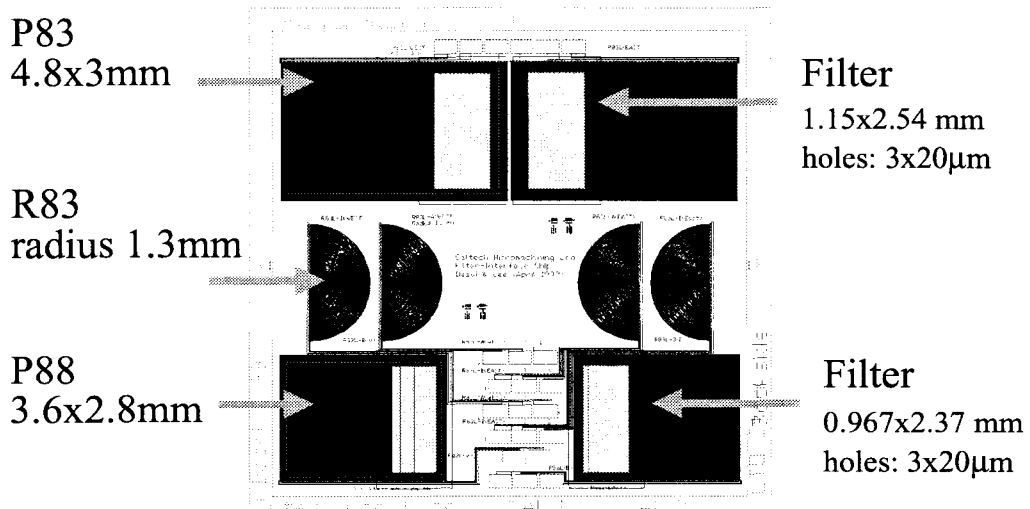


Figure 4-11: Integrated filter and particle transport layout (1cm x 1cm)

4.6 Silicone Elastomer – Sylgard[®] 184

In the past few years, silicones such as Sylgard[®] 184 (Dow Corning Corp.), commonly referred to as (polymethyldisiloxane) PDMS in literature [10], have become quite popular for lithographic molding, and other micromachining applications [11]. The PDMS backbone makes up the primary structure shown in Figure 4-12. This clear, naturally hydrophobic elastomer is cured by an organometallic crosslinking reaction which can be sped up with exposure to air and at elevated temperatures from 25 to 150°C. The hardness can be increased or decreased by 10% by increasing or lowering the amount of curing agent.

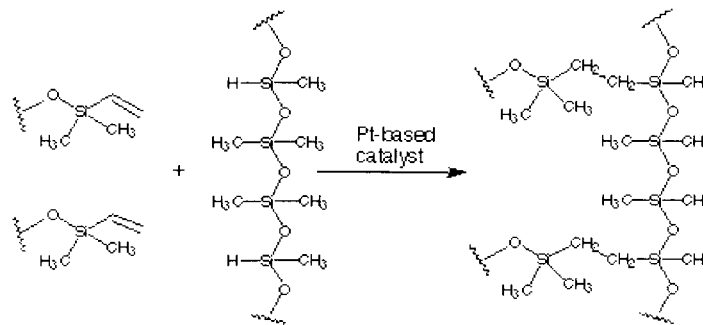


Figure 4-12: PDMS crosslinking reaction

Table 4-2: Properties of Sylgard[®] 184

Brittle point	-65°C
Dielectric strength	450 –600 V/mil
Durometer hardness	40 Shore A
Elongation	100%
Tear strength	2.6 kN/m
Tensile strength	6.20 MP
Thermal expansion coefficient	9.6% per 100°C
Water absorption	0.10% after 7 days

Because of its ability to seal over rough surfaces, its chemical resistance, and high dielectric strength, PDMS offers many advantages over the etched glass channels. For instance, the molding technique allows channel depths from 10µm to 5mm. Though

naturally hydrophobic, its surface can be made hydrophilic in O_2 plasma. Table 4-2 summarizes some of these properties of this elastomer.

The elastomer processing was fairly simple. The base and curing agent (in a 10:1 ratio) were mixed thoroughly and allowed to sit in a vacuum of 25 inches of mercury for 30 minutes. Next, the viscous solution was spun on the silicon wafer mold and cured at $130^\circ C$ for 3 hours. Cured thickness vs. spin rates are shown in Table 4-3. The $1\mu m$ of CHF_3 polymer was deposited on the silicon master as the release agent (Figure 4-13).

Table 4-3: Sylgard[®] 184 spin chart

Spin speed (krpm)	Cured thickness
0	2-3mm
0.12	1.5 mm
0.2	650 μm
4.0	100 μm



Figure 4-13: PDMS being released off the silicon wafer mold

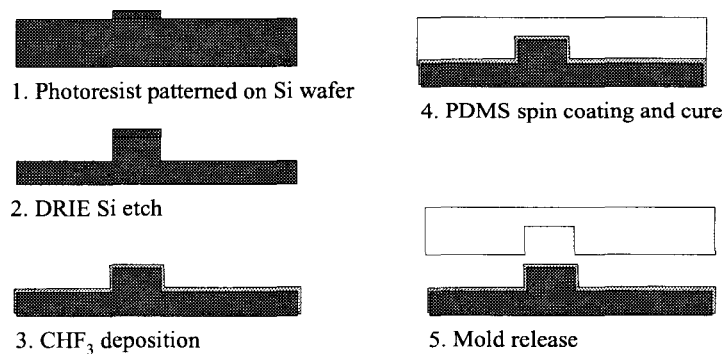


Figure 4-14: PDMS Channel fabrication steps

4.7 Second Generation Interface Fabrication

Combining the filter-plus-electrode structure, Figure 4-15, complicated bonding of the interface channels with the transportation chip because the spin-on AF1601S could not be used as the bonding material like before. Instead of the spin-on Teflon, the conformal CHF_3 polymer was deposited as the insulation spacer because of the filter holes. Because of the filter membrane, no spin on type processing could be done on the wafer. Details of this active filter fabrication can be found in work by Lee *et al.* [1] In any case, bonding to Teflon-like materials is generally troublesome; so the interface channel was molded with a flexible, transparent silicone elastomer, Sylgard[®] 184 (Dow Corning Corp.), and clamped down to the particle transportation chip. The fabrication steps for the PDMS channel are depicted in Figure 4-14. A schematic of the cross section and side view of the assembled device is illustrated in Figure 4-15. A video snapshot of a working prototype is shown in Figure 4-16. Much larger than the $\sim 50\mu\text{m}$ glass channels, the $500\mu\text{m}$ diameter PDMS channel allowed better control of the meniscus position.

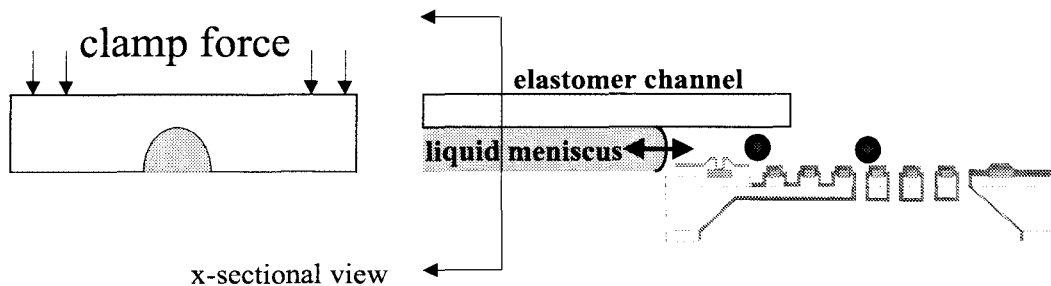


Figure 4-15: Moving meniscus concept integrated with an active filter region.

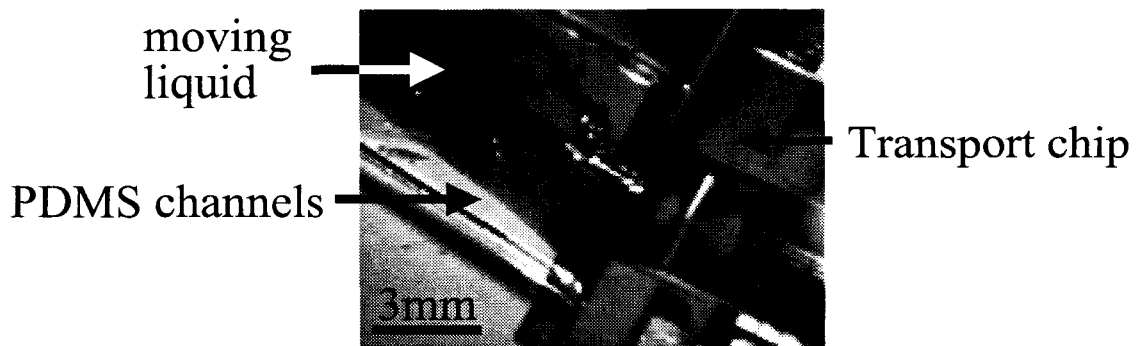


Figure 4-16: Video image of interface chip on radial transportation structure.

4.8 Second Generation Experiments

For the moving meniscus collection technique, experiments were successfully performed (see video) for the linear electrodes as well as for the radial structures (8 μm silica glass particles tested). A series of video snapshots of one experiment is depicted in Figure 4-17. The velocity of the oscillating meniscus ranged from 1-3 mm/s.

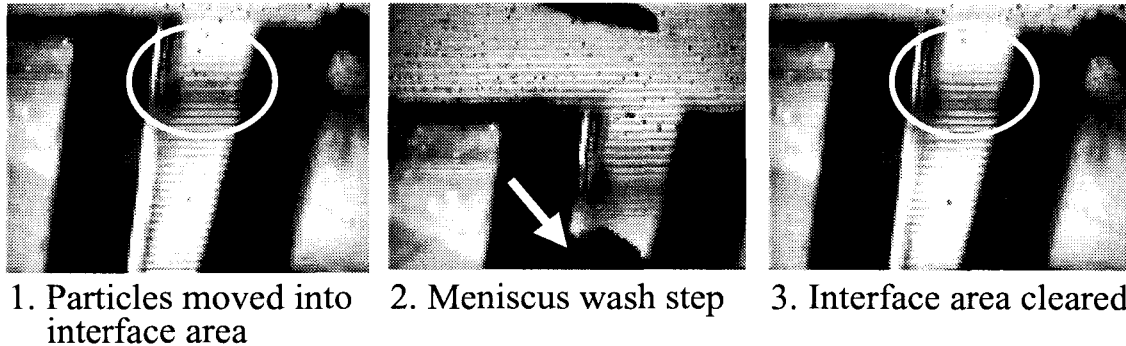


Figure 4-17: Snapshots of particles being captured from the air into the liquid meniscus

The collection efficiency was only about 5-10% because of three factors. First, there was a significant drop in efficiency due to the CHF_3 polymer coating. Secondly, the filter holes and structure also reduced efficiency from the normally observed 80-90% levels on the standard electrode grid. Finally, the particle contact with the liquid meniscus was limited by the interface opening width of 500 μm . The rest of the particles collected on the edges of the PDMS. Regarding this problem, the particle radial structures worked much better because particles which moved, moved toward the collection area (Figure 4-18).

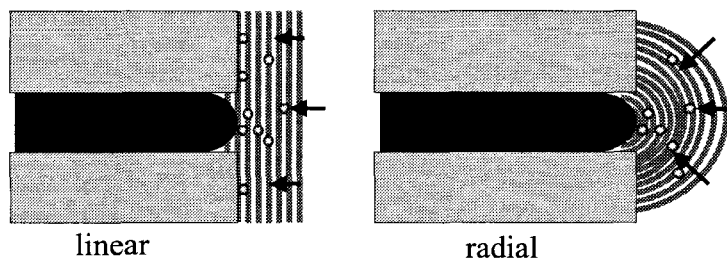


Figure 4-18: More particles moved near meniscus area with the radial design

One problem during testing was the long-term hydrophobicity of the plasma Teflon surface. After exposure to water, the Teflon surface started to retain micro-droplets of water ($<2\mu\text{m}$). This liquid residue affected the shape of the meniscus, and also reduced particle transportation efficiency in that area. In other words, particles would begin to get stuck just outside the travel of the meniscus. In addition, the whole experiment failed, if the liquid accidentally was pushed out beyond the interface channel onto the rest of the electrode grid. Some of the other design issues relate to the control of the liquid meniscus and the actual retention of the particles into the “flowing” part of the liquid system.

4.9 Conclusion

Two different particle air-to-liquid collection schemes were explored. The first type involved two regimes of voltages and frequencies but failed because the strength of the DEP force was too small to penetrate the liquid meniscus, and because of electrolysis of water on the electrodes. Successful collection was demonstrated through an entirely different type of technique- in which the liquid meniscus was moving and not the particles. With this method, the problems of the first type were circumvented. In addition, a membrane filter structure was integrated with the transportation technology and a new radial design demonstrated improved collection efficiency. In retrospect, although the solution for transporting particles from air to liquid in a micro-system may not be the most ideal because of complexity of assembly and lifetime issues, the knowledge gained here can be used to develop and understand more about stability of coatings and air-liquid interfaces. In fact, the initial droplet-on-a-capillary experiment shows great promise for the development of analyses and chemistries on arrays of liquid droplets.

References

1. P.K. Dasgupta, L. Ni, S.K. Poruthoor, and D.C. Hindes, "A Multiple Parallel Plate Wetted Screen Diffusion Denuder for High-Flow Air Sampling Applications," *Analytical Chemistry*, Vol. 69, 5018-5023.
2. S.W. Lee, J.M. Yang, Y.C. Tai, and C.M. Ho, "Electrostatically Active Microfilters For Automated Airborne Particle Collection," *Proceedings of Transducers '99, IEEE1999*.
3. G. Fuhr, T. Muller, Th. Schnelle, R. Hagedorn, A. Voigt, and S. Fiedler, "Radio Frequency Microtools for Particle and Live Cell Manipulation," *Natur Wissenschaften Aufsätze, Springer-Verlag*, 1994.
4. S.W. Lee, Y-W Kim, and Y-K Kim, "Determination of Dielectric Constant of Dielectric Particles Using Negative Dielectrophoresis," *Conference Proceedings on Electrical Insulation and Dielectric Phenomena*, San Francisco, October 20-23, 1996.
5. H. Morgan, N.G. Green, M. P. Hughes, and W. Monaghan, T.C. Tan, "Large-area travelling-wave dielectrophoresis particle separator," *Journal of Mechanics and Microengineering*, Vol. 7, Pg. 65-70, 1997.
6. F.M. White, *Viscous Fluid Flow*, McGraw Hill, New York, 1991.
7. Middleman, S., "Modeling Axisymmetric Flows: Dynamics of Films, Jets, and Drops," *Academic Press, San Diego*, 1995.
8. M. Kagan and W.V. Pinczewski, "NOTE Meniscus in a Narrow Slit," *Journal of Colloid and Interface Science*, Vol. 180, Pg. 293-295, 1996.
9. Wen Hsieh, personal communications, 1997.
10. S. Brittain, P. Kateri, Z. Xiao-Mei, and G. Whitesides, "Soft lithography and microfabrication" *Physics World*, May 1998.
11. X. Yang, C. Grosjean, Y. C. Tai, and C.M. Ho, "A MEMS Thermopneumatic Silicone Rubber Membrane Valve," *Sensors and Actuators A*, 64, pp.101-108, 1998.

Chapter 5

Electrospray Fundamentals

5.1 Introduction

Miniaturization of chemical analysis systems has been gaining popularity as MEMS technology has become more robust, feasible, and widely accepted as the technology for tomorrow's chip based chemical analysis systems. Over the past decade, several key steps have been taken in fabricating compact liquid chromatographs (LC) [1] and capillary electrophoresis chips (CE) [2]. There has been significant advancement in MEMS based chemical separation systems, but on-chip detection can be performed mainly by methods such as UV absorbance and electro-chemi-luminescence. These optical methods are not viable for most biomolecule (protein and peptide) detection; they are no match for the femtomole sensitivity, selectivity, and versatility (minimal liquid sample preparation) provided by a mass spectrometer (MS). The MS is an analytical instrument which can detect mass to charge (m/z) ratios of sample molecules. Further detail about MS is outlined in the next section.

Table 5-1: Mass spectrometer has superior sensitivity

Detection Method	Approximate Detection Limits
UV/visible absorbance	10^{-13} - 10^{-16} Moles
Fluorescence	10^{-15} - 10^{-17} Moles
Mass spectrometry	10^{-16}-10^{-17} Moles

Furthermore, because of this tremendous advantage in sensitivity, mass spectrometry is ideally suited for detection from small sample volumes. This femtomolar sensitivity, then, can be crucial for MEMS chemical systems where only small sample volumes are available. Therefore, these advantages compensate the drawbacks of the MS which are primarily cost and size. Thus, how to couple MEMS systems to an MS is the heart of the problem.

One method by which MEMS chemical systems can generate ions for MS analysis is with electrospray ionization (ESI) which was brought to light by Fenn *et al.* in 1989. A detailed explanation of the ESI method is presented in further detail in this chapter. Briefly, ESI is a simple method in which sample ions are produced in a fine stream from a liquid droplet in the presence of a strong electric field applied between the capillary tip and MS inlet. ESI has distinct advantages over other ionization strategies. Since it can generate multiply charged molecules (reducing the mass to charge (m/z) ratio), it makes it possible for mass spectrometer with small mass ranges to detect much larger molecules. Consequently, it can detect large molecules (theoretical limit $\sim 200,000$ Da, practical limit, $70,000$ Da) *directly* from the liquid sample. This capability is imperative for MEMS protein and peptide analysis where techniques like PCR amplification are futile. Other advantages include: the softest ionization (compared to other methods which makes it possible to observed biologically native non-covalent interactions), ease of use, and compatibility with liquid chromatography (LC) [3]. Therefore, ESI has been chosen to be the bridge between the MEMS device and the MS. This chapter includes a brief overview of MS, MS ionization methods, and an examination of electrospray ionization fundamentals.

5.2 Mass Spectrometry Overview

Mass spectrometry has been used for biomedical applications since the 1970's. Initially developed in the 1940's for the petroleum industry, it has now become standard equipment for biochemists. The MS is analogous to an optical prism that takes light as the input and separates it into different colors (wavelengths). In contrast to the prism, however, the MS takes ions as its input, and outputs a spectrum showing the number vs. ions mass to charge ratio. This operation is schematically shown in Figure 5-1.

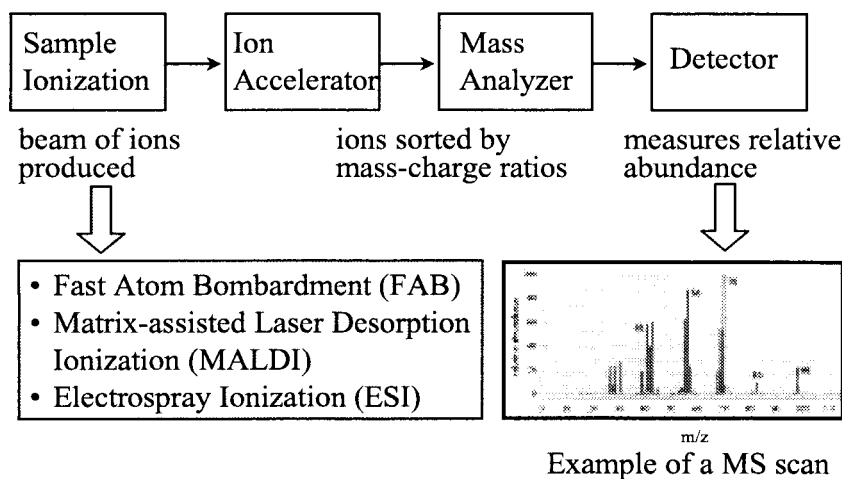


Figure 5-1: Parts of a mass spectrometry system

A complete MS system can be broken down into four main parts: a sample ionizer which produces a stream of sample ions, an ion accelerator, a mass analyzer which separates the ions according to their mass to charge (m/z) ratio, and a detector, to measure their relative abundance. The MS outputs a scanned spectrum showing a “fingerprint” of the sample which can be uniquely identified by spectrometrists. Except for the 1st stage, the sample ionizer, the rest of the parts are contained inside a typical benchtop MS. Our focus here lies in the sample ionization step in which the test biological liquid sample is introduced. The typical methods by which sample ions are generated and their advantages and disadvantages are shown in Table 5-1. From the table, we can see that ESI’s main advantage lies in its simplicity; it does not require much preparation. In fact, the liquid sample can be introduced in-line with high performance liquid chromatographic separations [HPLC] at flow rates up to 1 ml/min with a mass accuracy of $\pm 0.01\%$ [3]. On the other hand, Fast Atom Bombardment (FAB) and Matrix Assisted Laser Desorption Ionization (MALDI) require the sample be prepared in a matrix, which is unsuitable for liquid samples. The most distinct advantage of ESI over other ionization methods is that it can form a simple and direct way to interface MEMS device and mass spectrometers. All that is required on the MEMS chip is an electrospray nozzle which can be positioned in front of the MS inlet.

Table 5-2: Comparison of MS ionization methods

	FAB	MALDI	ESI
Sensitivity	nanomole	subpicomole	
Mass Limit (Da)	7,000	~300,000	~100,000
Preparation	Matrix	Matrix	None
Direct LC?	NO	NO	YES

Figure 5-2 shows a typical ESI source, a glass capillary packed with a filter and the MS inlet which operates at a few microliters per minute. Note that it is very important to have particle filters in the system to prevent clogging of the tip, which is typically on the order of 3-15 μm for micro-ES. In order to make this technique more compatible with conventional LC methods (requiring increased flow rates and reduced dependency on surface tension), various MS companies have developed pneumatically assisted spray tips (Perkin Elmer Sciex Inc.), heated metal capillary tubes (Finnigan MAT Inc.), and even tips with ultrasonic nebulizers (Analytica Inc.) [4]. These devices, using conventional production methods, cannot, however, be used in conjunction with the new MEMS LC or CE technology in which sample volumes are themselves on the order of *microliters* and require *nanoliter per minute* flow rates. Conventional ESI is done using glass capillaries creating large unnecessary dead volumes which require more of the sample fluid. Consequently, if MEMS bio-devices are interfaced using this conventional technique, the liquid sample must be piped out with conventional capillary tubing to the MS intake where the sample molecules are ionized and then detected. This increases in overall system dead volume, and in effect, compromises all the advantages gained in MEMS miniaturization of the liquid separation stage. What is needed then is a microfabricated on-chip interface that has the advantage of directly connecting the two systems together without these losses.

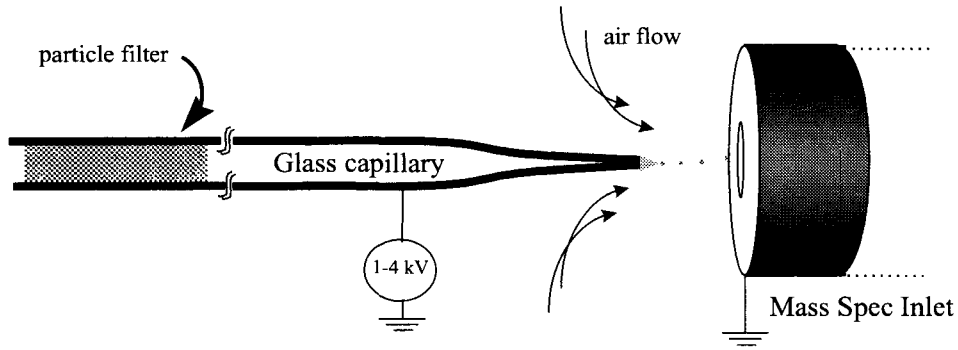


Figure 5-2: Typical electrospray configuration

5.3 Micro-Electrospray Ionization Fundamentals

In order to understand some of the MEMS design criteria for the ESI nozzle, we present here the fundamentals of the ESI phenomenon. Electrospray ionization (ESI) has become an important technique of generating ions for mass spectroscopic analysis of chemical and biological liquid samples [5, 6]. With its growing popularity, a lot of experimental data and understanding has been acquired by various groups such as Fenn (1985) and Wilm (1994); so today, ESI is an accepted technique for MS. ESI occurs when fluid in a capillary tip is subjected to a potential drop (1-4 kV) at atmospheric pressure. Because of the high electric field, the normal pendant shaped droplet turns into a sharp cone, referred to as the Taylor Cone, with charge induced on the surface. Spraying occurs at the Rayleigh limit when coulombic forces are large enough to overcome the surface tension forces. This Rayleigh limit [7] can be expressed as

$$\alpha = \frac{q^2}{3V\gamma\epsilon} \quad (5-1)$$

where

- q : charge on the drop
- V: volume of drop
- γ : surface tension
- ϵ : dielectric constant.

The limit is reached when α is greater than or equal to 4. Although significant work has been done in the past decades with liquids and electrostatics, much of the modeling is

limited to ideal approximations and geometries [7,8,9]. A brief derivation of the ideal Taylor Cone is presented here starting with the following assumptions: 1) the main forces acting on the liquid droplet are surface tension and electrostatic forces, 2) gravity is neglected, and 3) the fluid cone is static and conductive (so that electric field is orthogonal to the surface (Figure 5-3). From this derivation and its assumptions we can validate the benefits of scaling down from a conventional capillary ESI tip to a MEMS ESI structure. The final derived equation will show that with typical ESI conditions, the droplet radius is orders of magnitude smaller than the orifice diameter.

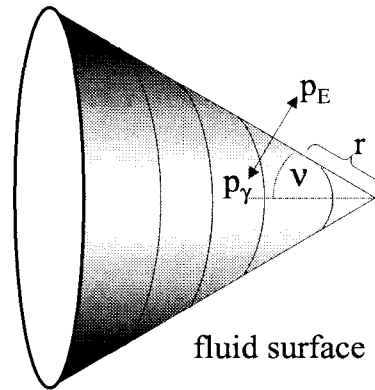


Figure 5-3: The Taylor Cone, where v is the cone angle, p_γ the surface tension pressure, and p_E the outward pressure from the electrical field. Note that the tip of the cone is an ellipsoid.

$$P_E = \frac{1}{2} \epsilon_0 E^2 \quad (5-2)$$

$$P_\gamma = \frac{\gamma}{r} \quad (5-3)$$

Equations 5-2 and 5-3 represent the two opposing pressures. P_E , the electrostatic pressure, is a function of the dielectric constant of the liquid and the field at the equipotential surface of the fluid. P_γ , the surface tension pressure is proportional to the surface tension divided by the radius of curvature, r . Converting these equations into a spherical coordinate system, we can express them in the following form [10]:

$$P_\gamma = \frac{\gamma \cos(v)}{r (1 - \cos^2(v))} \quad (5-4)$$

$$P_E = \frac{1}{2} \epsilon_0 \phi^2 r^{2(n-1)} \left[\frac{\partial}{\partial \theta} P_n \cos(\theta) \right]^2 \quad (5-5)$$

where v is the cone angle,
 ϕ_0 , the electrical potential constant
 P_n , the Legendre Polynomial of degree n
 n , the radius dependence of potential ϕ .

Setting Equations (5-4) and (5-5) equal to each other, we find that $n=0.5$ and $P_{1/2}(\cos \theta)=0$. This solution also implies that angle, v , must be 49.3° resulting in the classical Taylor Cone formula (Equation 5-6). When the liquid is spraying, this angle decreases with increasing flow rate.

$$\phi(r, \theta) = \phi_0 r^{0.5} P_{1/2}(\cos(\theta)) \quad (5-6)$$

By adding a perturbation term [11] to potential Equation (5-6), we approximate the change of the ellipsoid into a pointed cone (as shown in Figure 5-4 below) when the electrical field is increased above the threshold value.

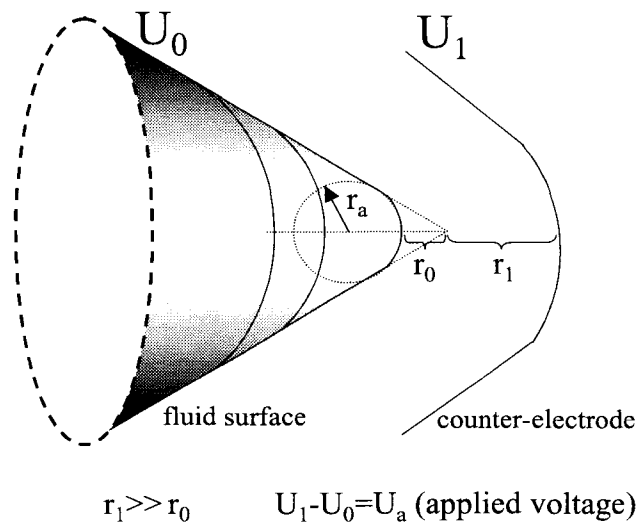


Figure 5-4: The liquid surface below threshold for cone generation [10].

From computer simulations, Wilm and Mann [10] have shown that $r_a \approx 7r_0$. With this step, they show that the pressure difference can be related to applied voltage in the following form:

$$P_\gamma - P_E = \frac{1}{r_a} \left(2\gamma - 2.68\epsilon_0 \frac{U_a^2}{r_1} \right) \quad (5-7)$$

Solving for U_a at the threshold point (left side of Equation (5-7) set to zero). We arrive at the equation for the threshold voltage, U_T :

$$U_T = 0.863 \left(\frac{\gamma r_1}{\epsilon_0} \right)^{\frac{1}{2}} \quad (5-8)$$

Substituting Equation 5-8 into Equation 5-7, we have a relation for pressure, p :

$$p = \frac{2\gamma}{r_a} \left(1 - \left[\frac{U_a}{U_T} \right]^2 \right) \quad (5-9)$$

Next the droplet radius can be calculated if the experimental conditions do not stray far from the static Taylor Cone. However, do note that for large flow rates, the cone becomes elongated and $\nu < 49.3^\circ$. The elongation is depicted in Figure 5-5 below.

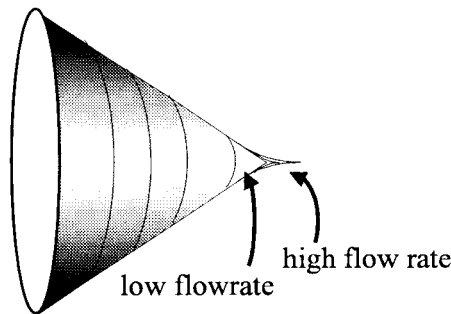


Figure 5-5: At higher flow rates of spray, cone angle deviates from 49.3° .

Consequently, for low flow rates we can assume that the emission diameter, r_e , approximates the droplet size. Also, by using the Bernoulli Equation (Equation 5-10), it is possible to approximate the radius at the apex of a spraying Taylor Cone.

$$\frac{1}{2} \rho v^2 + p = 0 \quad (5-10)$$

where ρ is the density of the fluid,

v , the velocity, and

p , the pressure.

The velocity of the fluid, dV/dt , is given by the relationship between the total flow rate divided by the cross-sectional area. In this case, we take this bounded area the radius, r_e .

$$v = \frac{dV/dt}{\pi r_e^2} \quad (5-11)$$

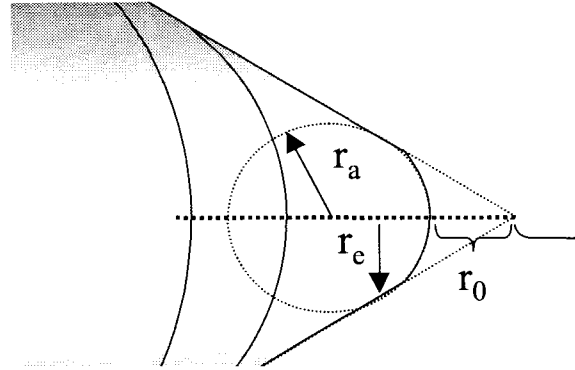


Figure 5-6: Magnified view of cone region

From the geometric correlation of the spraying Taylor cone and the curvature of the fluid sphere between the emission of two droplets [10], the relationship between r_a and r_e exists such that:

$$r_a = \frac{r_e}{\tan(\pi/2 - v)} \quad (5-12)$$

Substituting the relation for pressure (Equation 5-9), velocity (Equation 5-11), and r_a (Equation 5-12), we have the Wilm-Mann equation that gives us the radius of the emission region as a function of the following parameters:

$$r_e = \left(\frac{\rho}{4\pi^2 \gamma \left[\left(\frac{U_a}{U_t} \right)^2 - 1 \right] \tan\left(\frac{\pi}{2} - v\right)} \right)^{1/3} \cdot (dV/dt)^{2/3} \quad (5-13)$$

where:

r_e represents the radius of the emission region at the tip of the Taylor cone,

γ the surface tension of the liquid, ρ the density of the liquid,

U_a the applied voltage,

U_t the voltage at which the cone is formed,

ν the cone angle, and

dV/dt the flow rate.

This equation predicts that r_e , the emission radius, can be reduced with a reduction in flow rate. To see if MEMS type nozzles are compatible with this theoretical model, we can calculate the emission radius size for typical ESI conditions. Using the following: $\gamma = 0.03531 \text{ Nm}^{-1}$, $\rho = 896 \text{ kg m}^{-3}$, $U_a = 4000 \text{ V}$, $U_t = 1000 \text{ V}$, r_e is calculated as 33 nm . This result verifies that r_e is much smaller than $1 \mu\text{m}$, so MEMS nozzles do make sense. If r_e were larger than the normal MEMS sizes, then scaling down the nozzle might not have any merit.

5.4 MEMS for ESI?

From the calculation above, we see that the scaling of the ESI tip will not affect the size of the emitted droplets. Consequently, other advantages of microfabrication can be realized. Scientists working in the field of protein chemistry have shown that scaling down the ESI tip from typically $100 \mu\text{m}$ to $1 \mu\text{m}$ ID would result in significant improvements due to:

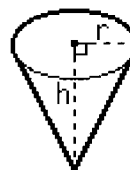
- 1) a smaller dead volume (minimum sample required for operation),
- 2) a more stable electrospray,
- 3) lower sample flow rates, and
- 4) lower voltages required for ionization [10].

A close-up photograph (Figure 5-7) of actual electrospray from a $370 \mu\text{m}$ OD ($160 \mu\text{m}$ ID) capillary illustrates the possible savings in dead volume with a smaller ES tip. The potential is 1250 V , and the sample fluid (1:1 methanol solution: water) is being pumped at $\sim 1 \mu\text{L}/\text{min}$. For a $400 \mu\text{m}$ OD capillary, we estimate *only* the Taylor cone volume as 10 nL . The calculation is shown below.

$$r = 200 \cdot 10^{-6} \cdot \text{m} \quad h = 250 \cdot 10^{-6} \cdot \text{m}$$

$$\text{Volume} = \frac{1}{3} \cdot \pi \cdot r^2 \cdot h$$

$$\text{Volume} = 1.047 \cdot 10^{-8} \cdot \text{liter}$$



However, for a $4\mu\text{m}$ diameter cone the dead volume would be reduced to 10fL ! Moreover, since this scaling down also reduces the cylindrical volume (inside the large capillary) behind the cone, the effective diameter of this cylindrical volume also decreases by two orders of magnitude with MEMS size scales.

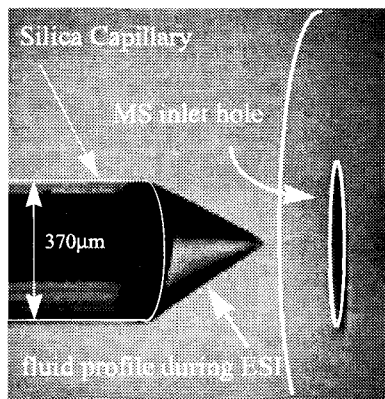


Figure 5-7: Electro spray from a capillary

With this trend toward smaller ESI tips, the conventional way of fabricating these $1\text{-}3\mu\text{m}$ diameter tips becomes difficult even with a micro-capillary puller. In addition to being time consuming, the major problem of this technique is to yield reproducible tip geometries. Finally, particle filters have to be inserted manually to prevent the tiny capillaries from clogging with debris. Figure 5-8 below shows a schematic of the various sizes of fused silica capillaries that have to be manually mated together to create the in-line filter [12].

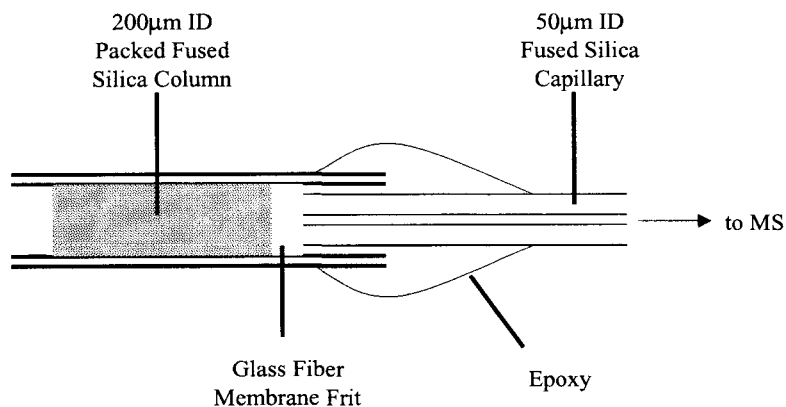


Figure 5-8: By careful manual packing, in-line filters are constructed

Many of these problems now can be taken care of simultaneously with MEMS technology. The capability to fabricate micron-sized tips with micromachining is advantageous in many ways:

- 1) the shape and finish of the tip can be reproducible from chip to chip,
- 2) complex MEMS filter structures can be constructed inside the micromachined liquid channel in order to filter out debris, and
- 3) mass production is available due to batch processing.

5.5 Conclusion

MEMS technology appears to be suited for the mass spectrometry field in the form of an ESI nozzle. We have discussed the various types of MS ionization schemes and the advantages of ESI. Furthermore, electrospray physics show that properties of the spray are not compromised when orifice geometries are scaled down to micron sizes. With MEMS technology various handling problems such as clogging and inconsistent tip structure can be addressed. Lastly, integration of other microfabricated elements such as filters, separation channels, electrophoresis electrodes, pumps, and valves becomes possible. The next chapters detail the development of a micromachined silicon nitride electrospray nozzle.

References

1. A. Manz, N. Graber, and H.M. Widmer, "Miniaturized Total Chemical Analysis Systems; A Novel Concept for Chemical Sensing," *Sensors and Actuators B*, B1, 244-248, 1990.
2. A. Manz, J. Harrison, E. Verpoorte, and H. Widmer, *Adv. Chromatography*, 1993, 33.1.
3. Siuzdak, Gary, *Mass Spectrometry for Biotechnology*, Academic Press Inc., 1996
4. L. Voress, "Electrospray MS Charging Full Stream Ahead," *Anal. Chem.*, 1994, Vol. 66, No. 8.
5. M. Yamashita and J.B. Fenn, "Electrospray Ion Source. Another variation on a Free-Jet Theme," *J. Phys. Chem.* 1984.
6. C.M. Whitehouse, R.N. Dreyer, M. Yamashita, and J.B. Fenn, "*Electrospray Interface for Liquid Chromatographs and Mass Spectrometers*," *Anal. Chem.* 1985.
7. M. Dole, L.L. Mack, R. L. Hines, R. C. Mobley, L.D. Ferguson, and M. B. Alice, "Molecular Beams of Macroions," *Journal of Chemical Physics*, 1963, Vol. 49, No. 5.
8. J. Fernandez de la Mora, "The effect of charge emission from electrified liquid cones," *Journal of Fluid Mechanics*, 1992, Vol. 243.
9. W. Balachandran, W. Machowski, and C.N. Ahmad, "Electrostatic Atomization of Conducting Liquids Using AC Superimposed on DC Fields," *IEEE Transactions on Industry Applications*, 1994, Vol. 30, No. 4.
10. M. Wilm and M. Mann, "Electrospray and Taylor Cone theory, Dole's beam of macromolecules at last?" *Intl. J. Of Mass Spectr. & Ion Proc.* 1994, 167-180.
11. R. Gomer, *Appl Phys.*, 19 (1979) 365.
12. M.T. Davis, D.C. Stahl, K.M. Swiderek, T.D. Lee, "Capillary Liquid Chromatography/Mass Spectrometry for Peptide and Protein Characterization," *METHODS: A Companion to Methods in Enzymology* 1994, Vol. 6, 304-314.

Chapter 6

First Generation Silicon Nitride Nozzles

6.1 Introduction

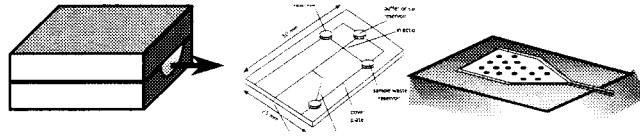
To realize this bridge between MEMS chemical devices and MS, the first few generations of the nozzle were designed primarily using silicon nitride and phosphosilicate glass (PSG) sacrificial layer technology. Other groups have demonstrated flat-edged glass channels for ESI, but their technology has significant limitations with respect to surface micromachined silicon nitride/PSG technology. This work is not alone in developing MEMS overhanging structures; Talbot and Pisano [1] demonstrated a two-wafer polymolding process to make polysilicon microcapillary, but in our case it is not easy to integrate these needles with microchannels and other microfluidic components on chip. Similarly, Papaustky *et al.* [2] reported a low temperature process to fabricate surface micromachined overhanging metallic microchannels. Unfortunately, the metallic structure material makes it difficult to perform many of the on-chip separation techniques (such as electrophoresis), and to visualize the liquid flow in the channels.

First, an overview of this PSG sacrificial layer technology is given. This overview is followed by the design and fabrication, and the testing and results of this 1st generation. Next, the advantages and drawbacks of further generations of silicon nitride nozzles are discussed. For example, on the second generation, effort was made to study the feasibility of different inlet-outlet geometries, on-chip grooves to attach silica capillaries, and longer nozzle overhang lengths. Finally, the benefits of polysilicon sacrificial layer technology for mm-long overhanging structures will be discussed, as well as the various thin film stress problems encountered.

6.2 Design Requirements

From the knowledge gained in conventional fused silica capillary (FSC) ESI, there are important criteria for a working MEMS ESI interface. Firstly, the device must have an

overhanging or protruding orifice so that the electric field can be better concentrated to induce electrospray for a given voltage. Secondly, the orifice geometry must be controllable at the micron-scale. Finally, incorporation of filter structures is necessary for $<10\mu\text{m}$ tips. Many of these requirements cannot be met with the glass channel type devices. Recently, Xue [3] and Ramsey [4] have both developed micro-ESI devices by interfacing flat-edged glass microchannels with cross sections of $10\mu\text{m}$ deep by $60\mu\text{m}$ wide to a MS and demonstrating electrospray (ES). The 1st generation device structure developed here is very different from Xue's and Ramsey's. Instead of employing a "blunt" orifice, we have fabricated an overhanging silicon nitride micro-channel $1\mu\text{m}$ high by $2\mu\text{m}$ wide, which dramatically reduces wetted surface area at the ES tip. Reduction of this orifice diameter and tip surface area reduces the size of the fluid cone during electrospray, thus reducing dead volume as discussed in the previous chapter. In addition to reducing dead volume, our nozzle design also included an important feature of integrated particle filter structures, which minimize clogging of this MEMS ESI tip. Figure 6-1 illustrates and compares the various ESI schemes.



	Xue et al.	Ramsey et al.	1st Generation Nozzles
Structure	GLASS	GLASS	Si, Si _x N _y
Orifice size	25 x 60 μm	10 x 60 μm	1 x 2 μm
Filters	NO	NO	YES
Nozzle	NO	NO	YES
Stability	30 min.	4.5+ min	40+ min

Figure 6-1: Related work on microfabricated ESI devices

The top figure shows the designed features and dimensions of the MEMS ESI interface. The silicon micromachined nozzle consists of a "sandwich" of $1\mu\text{m}$ phosphosilicate glass (PSG) enclosed by two silicon nitride layers each $1\mu\text{m}$ thick on a $500\mu\text{m}$ silicon substrate. The silicon nitride layers form the overhanging channel after the wafer is

etched in a potassium hydroxide (KOH) solution at 58°C. For testing, a 600µm OD silica capillary is epoxied into the trapezoidal backside inlet as shown in Figure 6-2 (right).

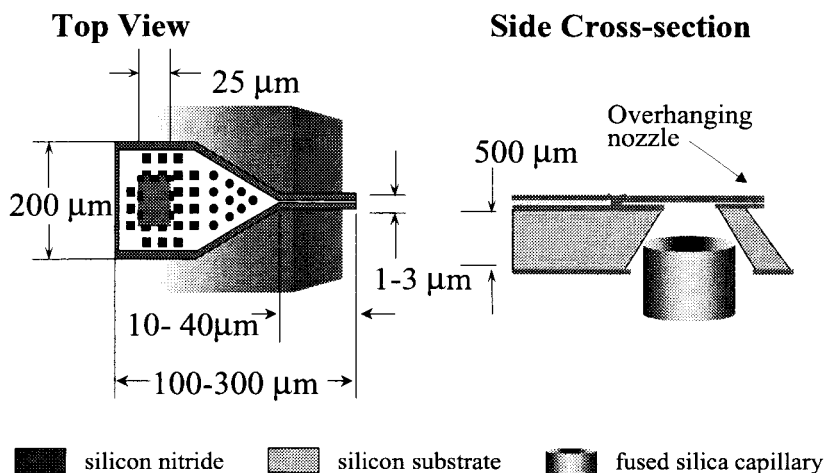


Figure 6-2: 1st generation nozzle design

The tiny black squares in the top view are filter structures, which prevent debris from moving forward and clogging the tip outlet. Electrical connection to the sample fluid is made with an in-line platinum fitting on the silica capillary.

6.3 Fabrication

The ESI nozzle fabrication involves using PSG sacrificial etch developed in the 1980's by researchers at Berkeley [5]. The key to this fabrication technique is the selectivity of the etchant to the sacrificial material vs. the structural material. Originally, the structures were created out of low pressure vapor deposited (LPCVD) polysilicon using PSG as the sacrificial layer and hydrofluoric (HF) acid as the etchant. Since HF etches PSG about a 1000 times faster [6], simple cantilever beams and channels can be easily fabricated. The main steps are shown in Figure 6-3 below. The sacrificial layer is first deposited and patterned in the shape of the micro-channel or cavity. Then, the structural material is deposited and etching windows are opened to allow the HF acid inside. After this liquid etch and DI water rinse, a microchannel with an inlet and outlet is formed. In this same way, silicon nitride can also be used instead of polysilicon [7]. Liu in our group demonstrated the feasibility and the use of silicon nitride micro-channels for gas pressure measurement and transport [8].

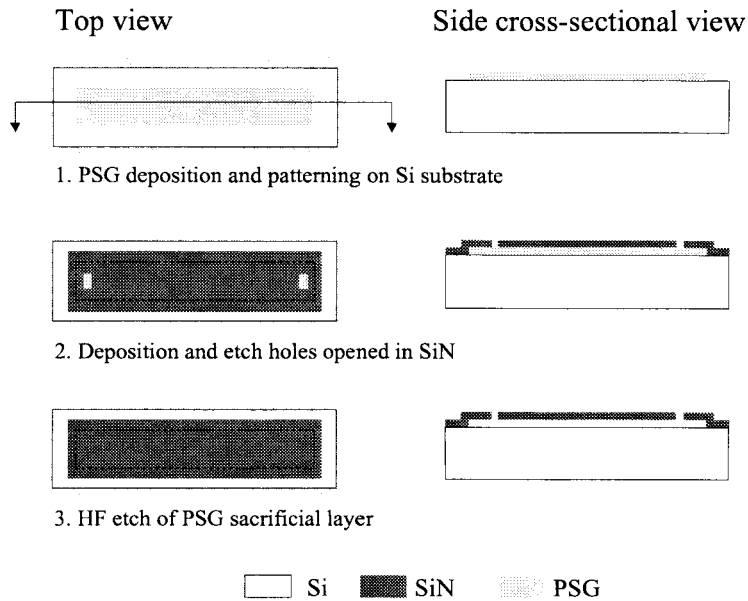


Figure 6-3: Typical steps for micro-channel fabrication

The etching of micro-channels is diffusion limited and has been studied and modeled by several groups [9]. Most importantly, as the channel length increases, the etch rate decreases such that only a certain maximum channel etch (200-300 μm) length is practical. Otherwise, the HF starts attacking the structural layer and increasing susceptibility for the layer to crack.

The fabrication sequence began with a 1 μm deposition of low stress LPCVD silicon nitride (850 $^{\circ}\text{C}$, $\text{SiH}_2\text{Cl}_2:\text{NH}_3$ ratio 4:1) [10]. Next, the silicon nitride was patterned with SF_6/O_2 plasma. This step exposed inlet holes so that access to the channel was permitted after the backside KOH etch. After patterning the silicon nitride, a 1 μm layer of PSG was deposited (450 $^{\circ}\text{C}$, $\text{PH}_3:\text{SiH}_4:\text{O}_2$ 1:2:6) and patterned with buffered HF. The PSG acted as the sacrificial layer for the micro-channel. In addition to forming the channel, the patterning of the rectangles into the PSG served to strengthen the inlet roof as well as create particle filter structures inside the channel.

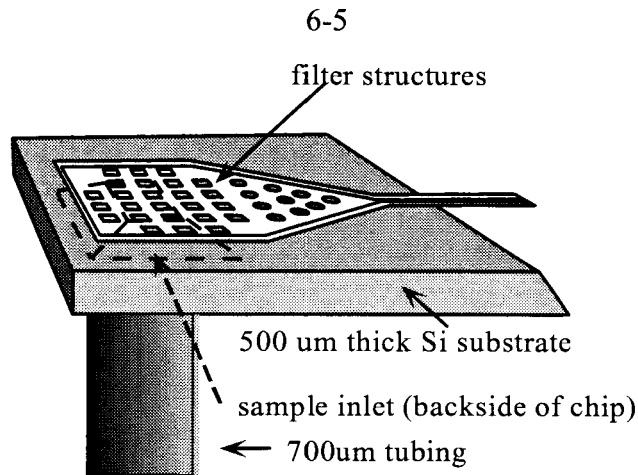


Figure 6-4: 3-d view of ES Nozzle

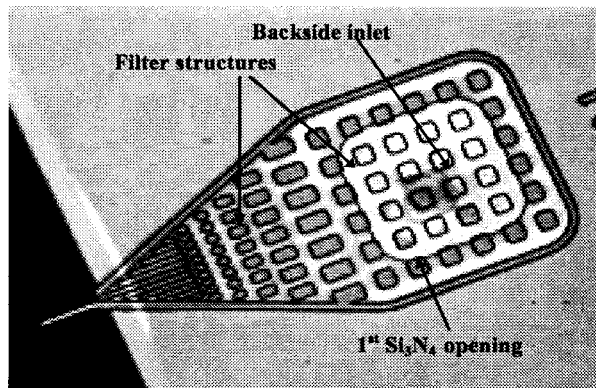


Figure 6-5: Nozzle top view showing backside inlet hole and filter structures.

To complete the “sandwich,” one more layer of 1 μ m silicon nitride was deposited and patterned. When this nitride layer was deposited on PSG, it became the roof of the channel, and in the areas where the PSG had been etched, this second nitride contacted the first nitride, the channel floor. Next, square backside windows were patterned into the wafer for the subsequent KOH bulk-etching step. The bulk etching was designed to occur from the front and backside simultaneously. From the front side, the KOH etch removed the silicon under the channel, thus defining the nozzle tip, and on the backside the wafer was etched until the nitride inlet holes had been reached. Keep in mind that to control size of the inlet opening at the top, the mask design had to be tailored to a specific wafer thickness. Figure 6-6 shows how each 1cm x 1cm die contains multiple nozzle design variations perched on the front-side cavities.

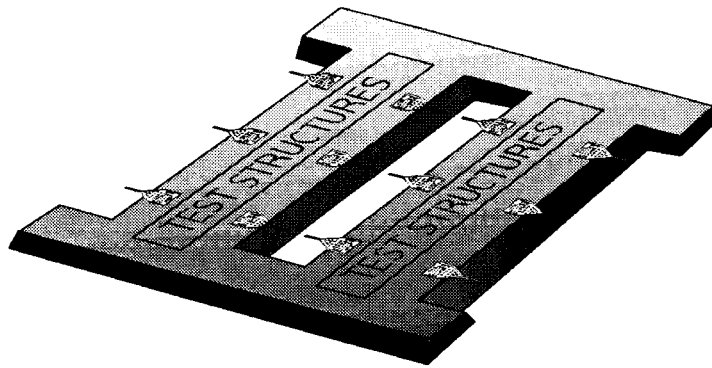


Figure 6-6: 1cm x 1cm die layout with overhanging ESI nozzles.

After rising the KOH off, the dies are etched for approximately 40 minutes in 49% HF to remove the sacrificial PSG inside the channel. The chips are subsequently rinsed in DI water overnight and baked dry. For testing, the connection was made by gluing a 700 μ m OD fused silica capillary to the backside inlet (Figure 6-4). The major fabrication process steps are shown in two cross-sectional views in Figure 6-7.

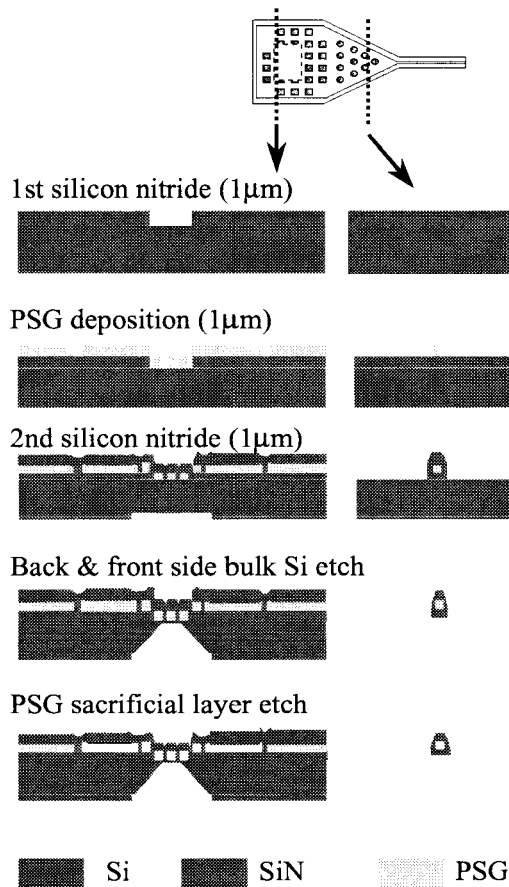


Figure 6-7: 1st generation major fabrication steps

6.4 Testing and Results

Fabricated nozzles were first extensively tested for structural rigidity and channel blockage by injection of DI water into the inlet. Many of the $1\mu\text{m}$ nozzles were prone to clogging at the very tip. Contamination from the sacrificial etch and crystallization of particles in the drying process were believed to be the cause of this clogging. This clogging problem was greatly reduced by a 24+ hour rinse in DI water, and a tip burn-in with an ethanol lamp. During fluidic testing, the liquid meniscus was monitored visually through a microscope as it traveled out to the tip. From video footage of this moving meniscus in the $2\mu\text{m}$ channel, we estimated a flow rate of 3.6 nL/min . Although the pressure drop of the fluid as it traveled through the nozzle channel was not measured, the reduction of the overall channel from $\sim 200\mu\text{m}$ to a micron size posed no significant back pressure when the channels were not clogged. A close-up of the nozzle orifice is shown in Figure 6-8. The $1\mu\text{m}$ channel height and particle filters ensured that no particulate matter was deposited at the nozzle tips from the sample fluid.

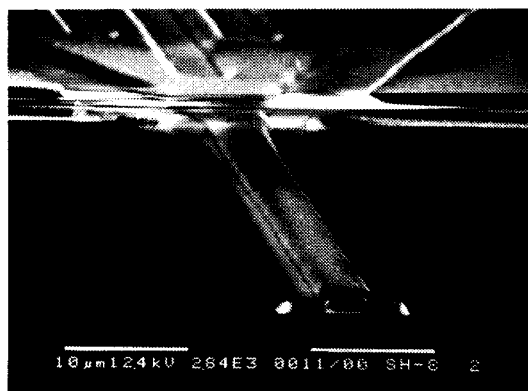


Figure 6-8: SEM photograph

For MS testing, the pyramidal liquid port on the back of the micromachined chip was converted to a tubular configuration by the addition of a short section of $740\mu\text{m OD} \times 530\mu\text{m ID}$ Fused Silica Capillary (FSC)(Polymicro Technologies, Phoenix, AZ). The FSC extension was positioned within the liquid port using a crude micro-manipulator

with visual confirmation of joint alignment from a Leica X 1000 stereo microscope. The extension was secured using a standard two-part epoxy resin. Once cured, the extension was cut to a final length of one cm. Liquid connection to the chip interface was achieved using a multi-laminate fused silica transfer line constructed as follows. The running length of transfer line (10-15 cm) was constructed from 150 μm OD x 25 μm ID FSC. Each end of the transfer line was inserted into a 2-3 cm section of 350 μm OD x 155 μm ID FSC until flush and then sealed with epoxy resin. Upon drying, one end of the butted transferline was inserted into the 530 μm ID FSC extension and sealed in the same manner.

Chip performance was analyzed using a standardized solution of Gramicidin S. The test sample was dissolved in 50:50 MeOH:Water, 1% HOAc (by volume) at a final concentration of 4 pmole/ μl . A Harvard Apparatus model 44 syringe pump fitted with a 50 μl gastight syringe (Hamilton, Reno, NV) was used to deliver the test compound to the nozzle via a separate 75 cm length of 350 μm OD x 75 μm ID FSC transfer line. A 2.5 cm section of 22 gauge Platinum tubing (Hamilton) was fitted to the end of the transfer line to provide the necessary liquid-metal contact for sample ionization. Final connection to the transfer line was through a Supelco Capillary Butt connector using a 0.4-mm to 0.8-mm ID dual sided Vespel ferrule (Supelco Inc., Bellefonte, PA).

The standard ESI interface to the Finnigan Mat LCQ Ion Trap mass spectrometer was replaced with a custom polyacrylic platform upon which an XYZ micropositioning translational stage had been mounted. The nozzle chip was secured to the XYZ stage using a modified micro-clamp (clothes pin) and precisely positioned under a high-power stereomicroscope (Zeiss, STEMI SV8, 200mm lens, 25x ocular). A fiber optic cold light source (Schott, model KL1500) was used for illumination. The high voltage lead from the mass spectrometer was modified to terminate in a small alligator clamp to facilitate the connection to the Platinum electrode. The nozzle was centered in front of the heated capillary inlet of the mass spectrometer at a distance of 0.25 mm to 0.4 mm.

The Finnigan Mat LCQ Ion Trap mass spectrometer was operated under manual control through the "Tune Plus" view over a scan range from 500 to 1200 AMU. The maximum

injection time was 500 ms with an AQC setting of 1.0×10^8 for full mass range analysis. A 4 kV potential was applied to the platinum electrode for sample ionization. Figure 6-9 shows a mass spectrum analysis of gramicidin S. The group of doubly charged ions (m/z ratios 571.3-572.3) characteristic of Gramicidin S have been clearly detected above the background ions. The additional peaks (background noise) in the spectrum seem to have come from epoxy residue. Although epoxy contamination remains an important issue when the nozzle is used by itself, on-chip integration with other separation devices should eliminate this problem. The sensitivity of this MS analysis was comparable to conventional analyses using ESI sources.

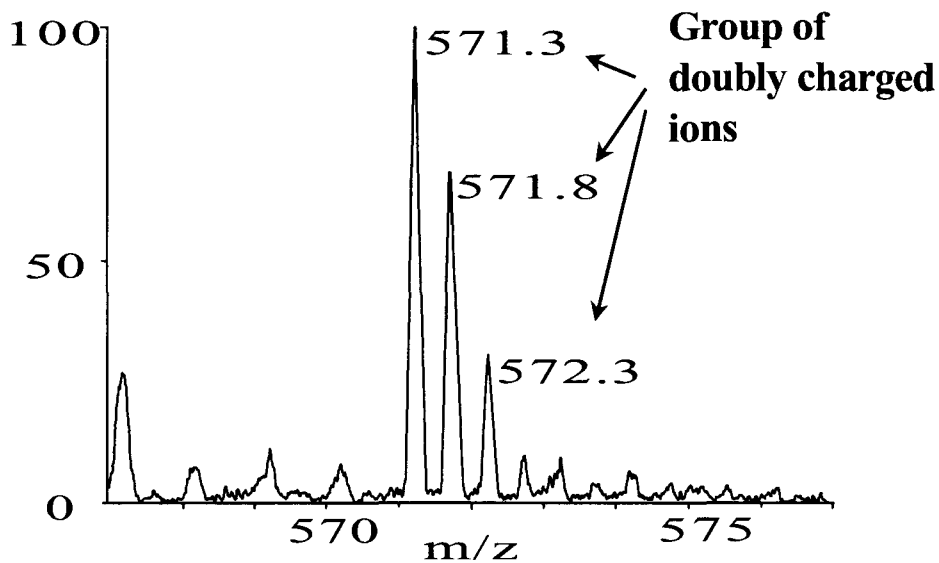


Figure 6-9: MS scan of Gramicidin S using MEMS nozzle

6.5 1st Generation Problems

Though the concept of MEMS ESI had been demonstrated, there were several limitations imposed on the design of the nozzle because of the HF/PSG process. Firstly, the channel length (distance from inlet to outlet) was limited to $<300\mu\text{m}$ because of the diffusion controlled HF etching technique. From HF/PSG etching data from [9] we saw that it took approximately 20min to etch the B-type structures and <5 min for the A-types. However, doubling the nozzle dimension lengthwise required etch times of more than 2 hours! Prolonged time in the etchant etched the silicon nitride channel walls and resulted

in cracking. Yield was also limited by high pinhole density in the 2nd silicon nitride layer.

Furthermore, this 300 μm length limit of the channel coupled with undercut of the $\langle 111 \rangle$ silicon plane resulted in a fragile front wall of the backside inlet window. Figure 6-10 below clearly shows the problem. The large inlet hole also caused many of the structures to burst during testing, and the filter structures, which were supposed to act as posts, were ineffective. Non-uniformity of during the sacrificial etch was created by the hydrophobic silicon sidewalls (freshly etched in KOH). Their hydrophobic nature did not allow the HF to enter the backside inlet hole. Although this problem was solved by manual probing and “breaking” of the air bubble, it was a tedious serial process. The smaller the inlet hole, the harder it was to remove this bubble (see surface tension discussion in Chapter 3) (Figure 6-11)

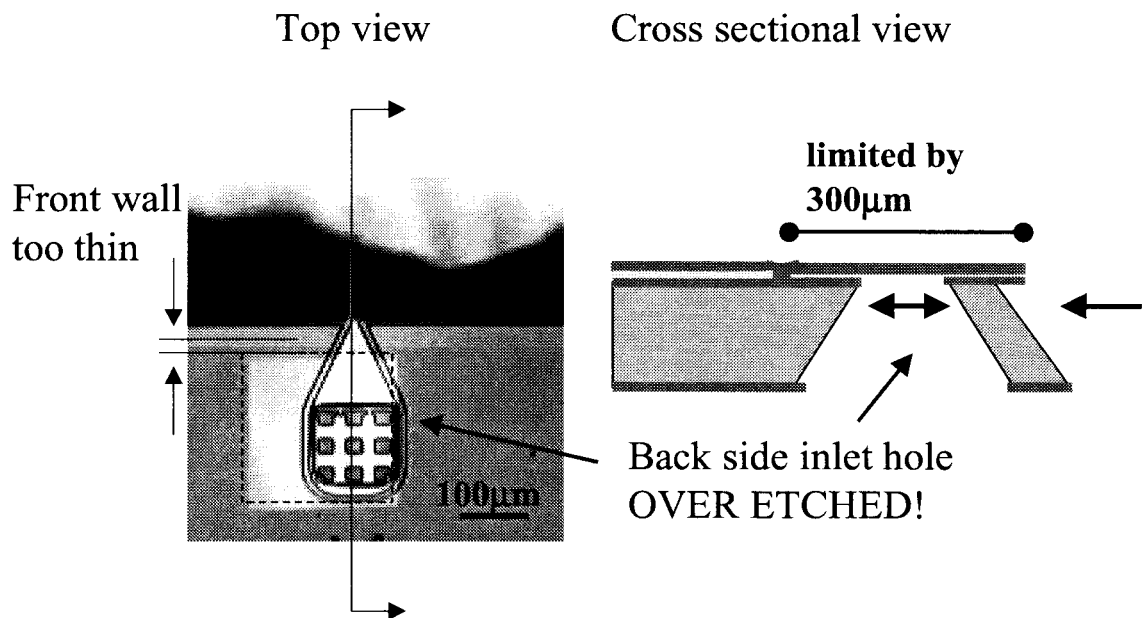


Figure 6-10: Backside inlet hole enlargement results in weak front wall

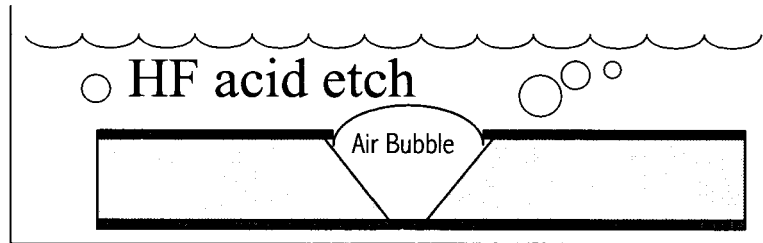


Figure 6-11: Formation of air bubble in backside inlet holes on wafer.

As an artifact of the plasma etching process, initial prototypes also had a silicon nitride “tongue.” The “tongue,” circled in Figure 6-12 below, formed during the plasma etching of the 2nd silicon nitride layer. During the etch, the PSG layer acted as a mask for the 1st nitride layer. This problem was eliminated by an intermediate HF dip after the SF₆/O₂ plasma had etched the 1st nitride, and then continuing to plasma etch the bottom nitride layer.

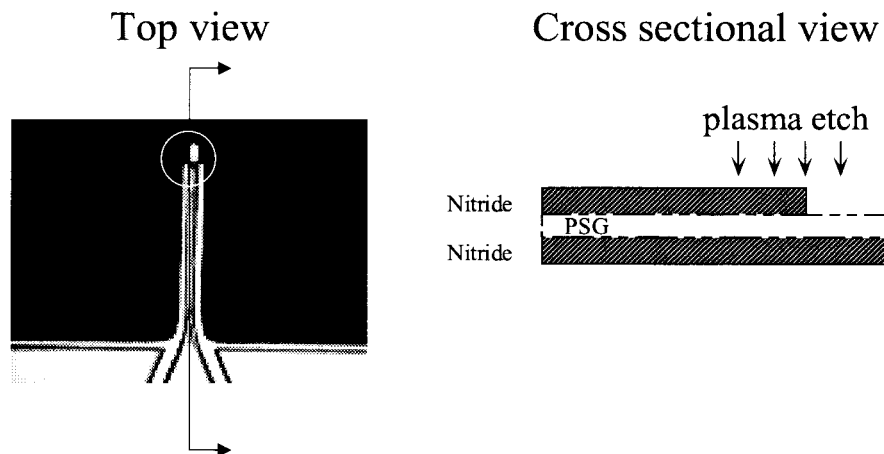


Figure 6-12: Picture of silicon nitride “tongue” at the nozzle outlet because of PSG layer masking.

In addition to these fabrication problems, the attachment of the FSC proved to be a daunting and tedious task. The gluing had to be performed at the right moment with the Dupont 5 Minute epoxy - when the epoxy was viscous enough not to flow into the backside cavity and seal the device, but still uncured enough to position the capillary. Over 50% of the working devices were destroyed during this gluing process which had to be done under a stereo microscope.

References

1. N.H. Talbot and A.P. Pisano, "Polymolding: Two wafer polysilicon micromolding of closed-Flow Passages for microcapillaries and microfluidic devices". Solid-State Sensor and Actuator Workshop, 1998.
2. I. Papautsky, A.B. Frazier, and H. Swerdlow, "A low temperature IC compatible process for fabricating surface micromachined metallic microchannels." *MEMS '97*.
3. Q. Xue, F. Foret, Y. Dunayevskiy, P. Zavracky, N. McGruer, and B. Karger, "Multichannel Microchip Electrospray Mass Spectrometry," *Anal. Chem.* 1997, 69, 426-430.
4. R. Ramsey and J. Ramsey, "Generating Electrospray from Microchip Devices Using Electroosmotic Pumping," *Anal. Chem.* 1997, 69, 1174-1178.
5. R.T. Howe and R.S. Muller, "Polycrystalline Silicon Micromechanical Beams," *Journal of Electrochemical Society*, Vol. 130, pp. 1420-1423, 1983.
6. K. Williams and R.S. Muller, "Etch Rates for Micromachining Processing," *Journal of Microelectromechanical Systems*, Vol. 5, No. 4, 1996.
7. C. Mastrangelo, Y.C. Tai and R. S. Muller, "Thermophysical properties of low-residual stress, silicon-rich, LPCVD silicon nitride films," *Sensors Actuators A (Phys.)*, Vol. A57, no. 2, pp.103-110, November 1996.
8. J.Q. Liu, *Integrated Micro Devices for Small Scale Gaseous Flow Study*, Ph.D. Thesis, California Institute of Technology, 1995.
9. J.Q. Liu, Y.C. Tai, J. Lee, K.C. Pong, Y. Zohar, and C.M. Ho, "In Situ Monitoring and Universal Modeling of Sacrificial PSG Etching Using Hydrofluoric Acid," *Proceedings of IEEE Workshop on Micro Electro Mechanical Systems (MEMS '93)*, pp. 71-76, Fort Lauderdale, USA, February 1993.
10. M. Sekimoto, H. Yoshihara, and T. Ohkubo, "Silicon Nitride Single-Layer 6-Ray Mask," *Journal of Vacuum Science and Technology*, Vol. 21(4), pp.1017-1021, November/December 1982
11. A. Desai, Y.C. Tai, M. T. Davis, and T. D. Lee, "A MEMS Electrospray Nozzle for Mass Spectroscopy," *1997 International Conference on Solid-State Sensors and Actuators (Transducers '97)*, May 1997.

Chapter 7

Further Generations of Si_xN_y Nozzles

7.1 Introduction

From the previous chapter, there were many features that could be improved and other which could be added. This chapter discusses the advantages and drawbacks of further generations of silicon nitride nozzles. For example, on the second generation, effort was made to study the feasibility of different inlet-outlet geometries, on-chip grooves to attach silica capillaries, and longer nozzle overhang lengths. Furthermore, rationale is given for the various substrate sidewall designs through electrostatic simulation. In addition, the benefits of polysilicon sacrificial layer technology for mm-long overhanging structures will be discussed, as well as the various thin film stress problems encountered. For the first time, MEMS ESI flow visualization was performed validating some of the theoretical assumptions of the Taylor Cone, and bringing to light some new aspects of this phenomenon.

7.2 2nd Generation Nozzle Design

To address many of the problems of the 1st generation, a second fabrication of the nozzles was done. The process and design of these ESI nozzles was significantly different from the previous run. In this design, the sacrificial layer was switched from PSG to polysilicon in the hope of increasing the overall length of the nozzle. There are many benefits of using polysilicon as the sacrificial layer instead of PSG. The most important is that the etch rate is linear [1], and not parabolic like HF-PSG etching. This feature allows channel lengths of 1000 μm with only the inlet and outlet as the etch holes. Furthermore, the polysilicon is etched using tetramethylammonium hydroxide (TMAH) solution which is much more selective, and almost does not attack the silicon nitride [2]. On the other hand, concentrated HF (48%) etches silicon nitride at 50-100 $\text{\AA}/\text{min}$.

The use of the polysilicon offers other advantages as well. The polysilicon can be locally oxidized, and thus true post-type filter structures can be fabricated reducing stress concentrations in the silicon nitride. The stress concentration in the silicon nitride (demonstrated by [3,4]) can be reduced by keeping the top silicon nitride flat on the boundary of the channel. Further details on the fabrication technique are provided in the next section. Figure 7-1 shows the difference between the first and the second generation.

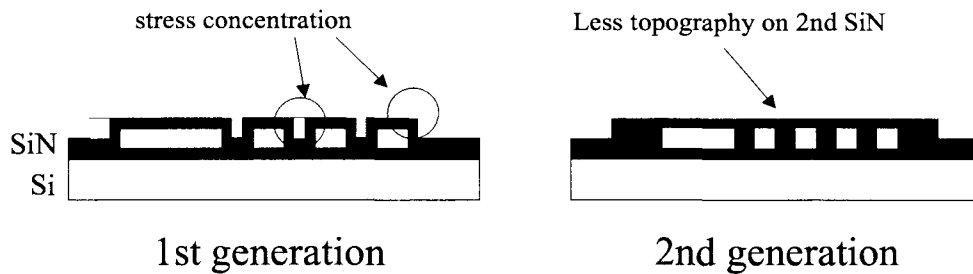


Figure 7-1: Polysilicon/oxide posts can be used to create flatter, stronger channel roofs.

Though the first prototype demonstrated sustainable ESI from the tip, electrostatic simulations clearly quantified the benefits of having an outlet that projected far beyond the (conductive) substrate sidewall. Simulations were accomplished using the 2-D MAXWELL electrostatic simulator [5]. In reality, the MS inlet is more like a thick walled pipe, but the simulation serves as a point of reference (relative) in comparing the different nozzle-silicon substrate profiles with each other. The conductivity of the fluid was assumed to be 5 S/m at a potential of 1000V. The silicon substrate was also set to the same high potential since the sample fluid contacted the backside substrate. From the simulation, it was apparent that the silicon substrate shape and nozzle overhang length affected the electric field concentration at the tip. Results of the simulations of the various substrate profiles are tabulated below (Table 7-1).

Table 7-1: Electric field concentration at the nozzle tip for various overhang profiles

	Structure description (overhang length)	Schematic	Electric field magnitude at tip (V/m)
1.	Short-slant-forward (30 μ m)		2×10^6
2.	Short-slant-back (30 μ m) (proposed 2 nd generation)		4×10^6
3.	Long (1.5mm)		5×10^6

From the table, most of the field concentration increase comes from keeping the silicon substrate away from the nozzle tip. There is a 100% increase from structure type 1 to 2 but only 50% from structure 2 to 3. This simulation also suggests that getting rid of the silicon could be very beneficial. Contour plots of the three simulations above are shown in Figures 7-2, 7-3, and 7-4 below. Note that each contour plot scaling is slightly different for color and e-field magnitude.



Figure 7-2: Type 1- Short-slant-forward, maximum field concentration, 2×10^6 V/m

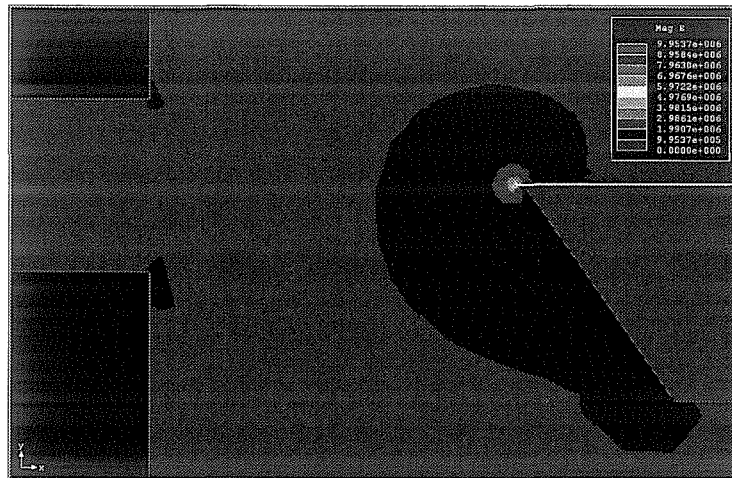


Figure 7-3: Type 2 – Short-slant-back, maximum field concentration, 4×10^6 V/m

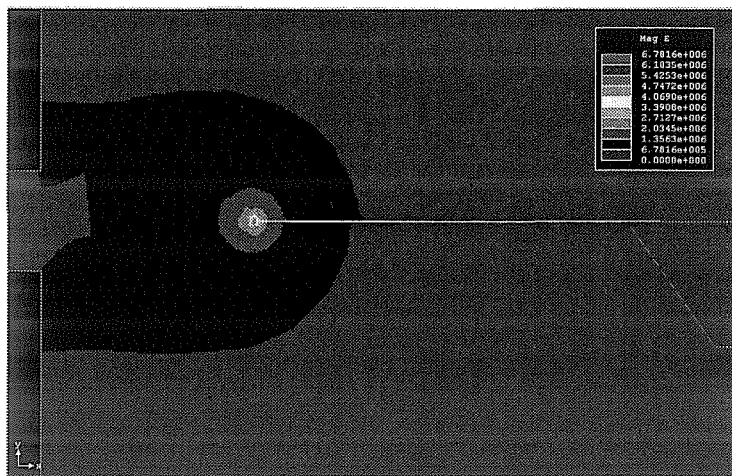


Figure 7-4: Type 3 – Long, maximum field concentration, 5×10^6 V/m

Other modifications and improvements included the following: a) front side grooves for easier capillary connections, b) inward sloping side-wall and larger overhang lengths, and c) gold line to tip for electrical connection to sample fluid (Figure 7-5). Demonstration of polysilicon as sacrificial layer for these 800 μ m long structures was the object of this nozzle design.

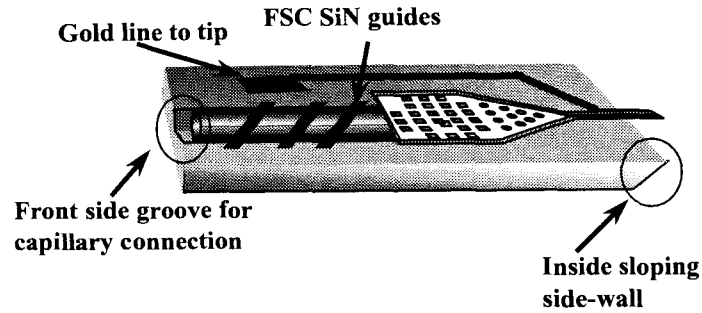


Figure 7-5: 2nd generation modifications

7.3 2nd Generation Nozzle Fabrication

The 2nd generation fabrication steps, in general, were quite similar to the first nozzle process. On a <100> Si wafer, 4000Å of PSG was deposited and patterned to define the frontside grooves. Next, 1µm of silicon nitride was deposited and patterned with SF₆:O₂ plasma. Instead of the PSG sacrificial layer, here, 1µm of LPCVD polysilicon was deposited at 620°C. The poly was dry oxidized at 900°C for 45 minutes to form 1000Å of oxide. After patterning the polysilicon, another 1000Å of silicon nitride was deposited and patterned. The next critical step was to partially wet etch 6000Å of polysilicon with HNA (HNO₃ (70%), H₂O, NH₄F (40%)). Control of this etch determined the flatness of the final silicon nitride deposition for the channel roof. The thin (1000Å) nitride layer acted as the oxidation mask allowing oxidation only on exposed poly areas. The 4000Å of remaining polysilicon was converted into ~1µm SiO₂ posts (Step 5, Figure 7-6). 1µm silicon nitride was deposited to create the roof of the channel. After a 5 minute TMAH dip (90°C 10% TMAH concentration), 100Å of chrome and 700Å of gold were thermally evaporated and patterned to form electrodes to connect the tip. Finally, the wafer was etched in TMAH in two steps. The first etch for seven hours to etch the channels, and the second etch to open up the grooves on the front side and the inward slanting slope from the backside. Typical polysilicon etch rate in TMAH was 90µm/hr. Figure 7-7 shows an SEM picture of a released nozzle (structure A).

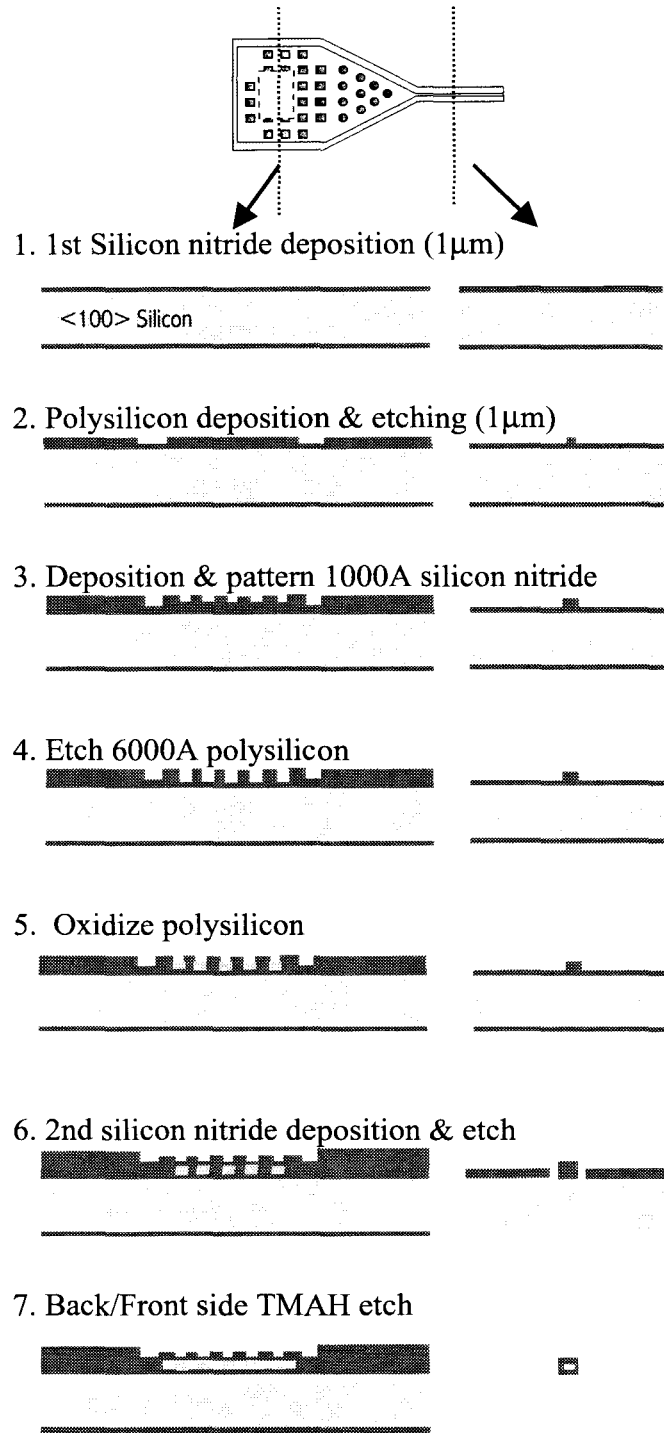


Figure 7-6: Major fabrication steps for the polysilicon sacrificial layer process

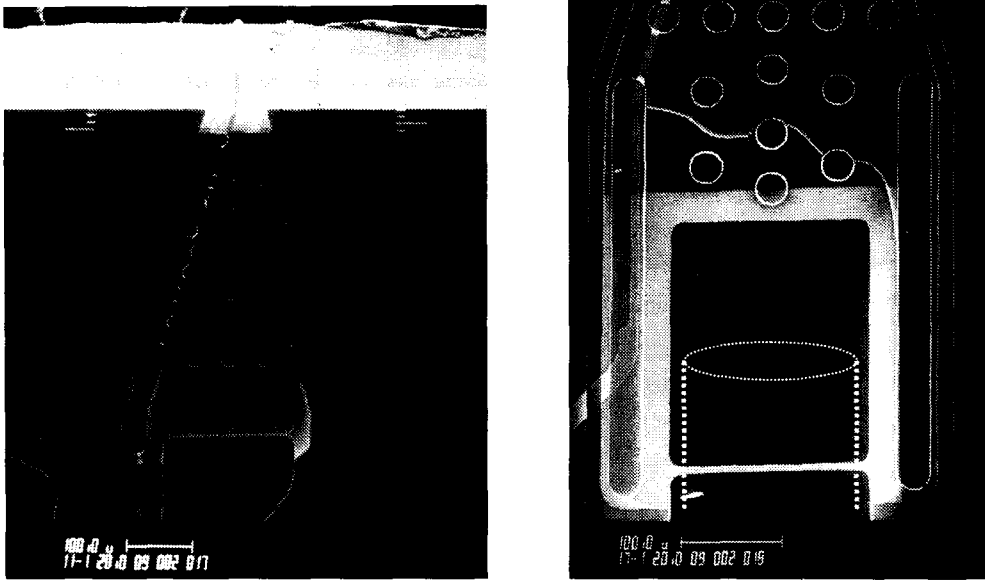


Figure 7-7: 2nd generation nozzles

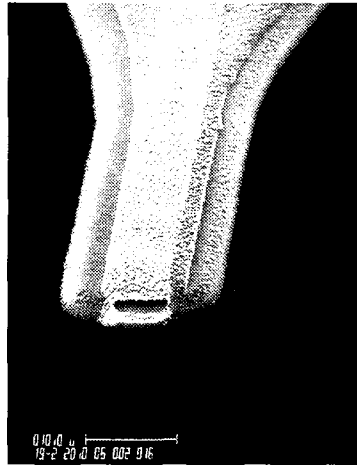


Figure 7-8: Detail of evaporated gold line over nozzle tip.

7.4 2nd Generation Fabrication Issues

The polysilicon sacrificial layer fabrication technique was clearly successful and the two advantages of utilizing polysilicon as a sacrificial layer were established. Channel structures as long as 800 μm were released with only two etch holes – an inlet and outlet. Large silicon nitride membranes (50 μm x 225 μm) over the inlet cavity could be fabricated although there was significant bubble generation during etching. Test membrane structures showed that the upper limit before cracking was about 200 μm x

200 μm . Membranes larger than this dimension required internal supporting structures such as posts or walls.

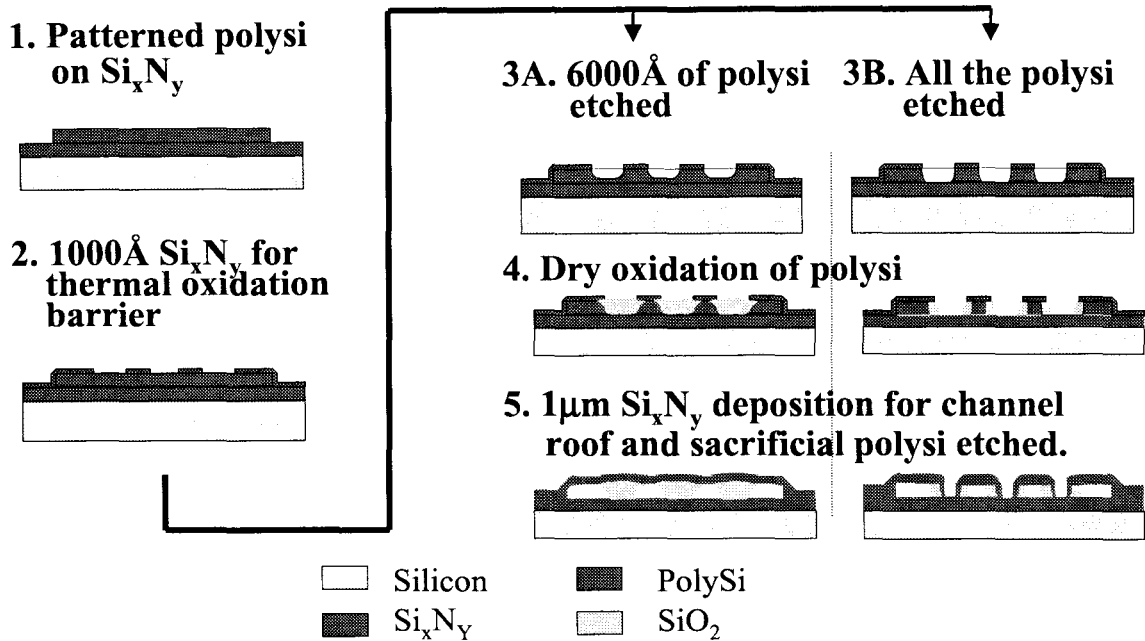


Figure 7-9: Same fabrication process resulted in two different filter/post structures due to overetch.

Two types of flat channel roof-post techniques were demonstrated. The first method pictured in Figure 7-9 is shown in further detail in Figure 7-10 below. This method relies on the delicate etch-back of polysilicon (poly) to a predetermined level. In our case, 1 μm of poly is etched back leaving 4000 Å. Due to the silicon dioxide-silicon consumption ratio (~ 1.6), these “vias” are converted to posts which are approximately at the same height to the original polysilicon thickness (Step 4, left). Thus, instead of a corrugated type channel roof structure, the top silicon nitride profile is flatter thus stronger. Figure 7-10 below shows the bird’s beak effect (“donuts”) and the elimination of a corrugated channel roof.

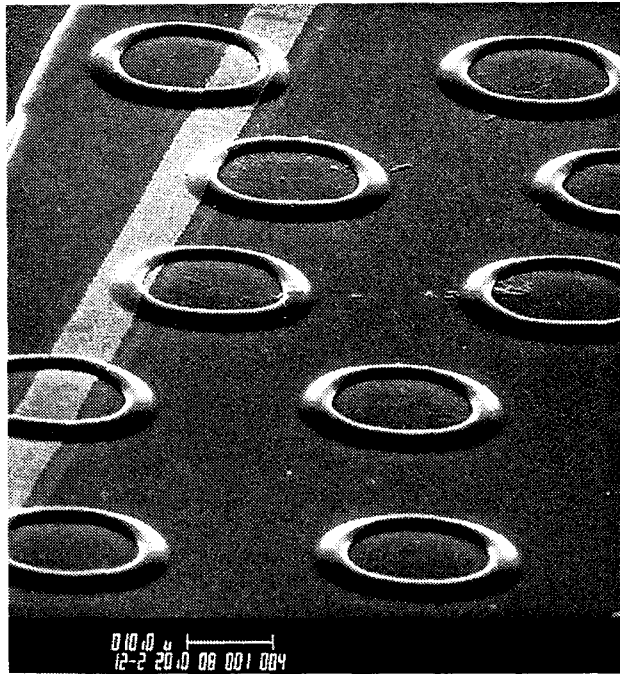


Figure 7-10: The “donuts” are boundaries of the post/filter structures.

Though this technique eliminates the corrugated type structure, it is difficult to control the HNA etch since the etch rate can vary from 1500 to 3000Å/min. In Step 3B of figure 7-9, all of the polysilicon was etched, leaving exposed poly on the sidewalls which could be readily converted to SiO₂ in Step 4. In this case, the oxidation occurs *laterally* and the corrugated silicon nitride stress concentrations are strengthened with oxide “rings.” Figure 7-11 shows close-ups of this type of structure. Since there is a 1μm step at every post structure, the gold line had to be rerouted around the filter structures to avoid step coverage problem such as the one shown in Figure 7-12.

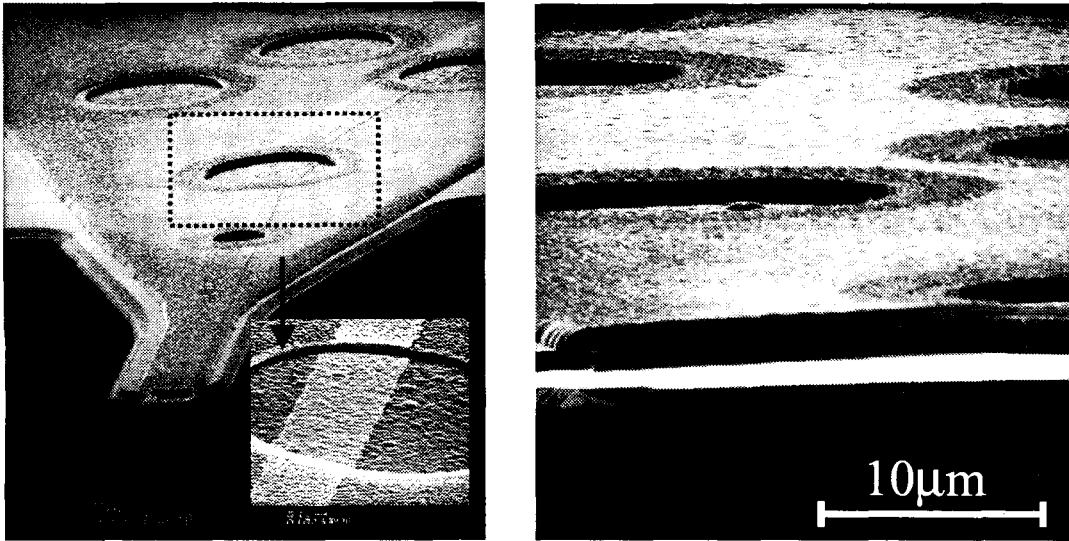


Figure 7-11: Flat silicon nitride channel roof achieved with ringed oxide post structures.

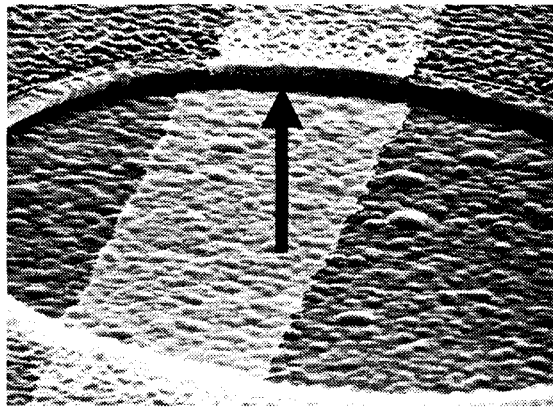


Figure 7-12: 1-2 μ m step causes discontinuity in evaporated gold line to tip.

In terms of practical usage, the grooves with the top nitride membrane support for the silica capillaries were fragile. Despite the fact that with delicate stereoscopic manipulation insertion of the FSC was possible, sealing of the inlet was prone to failure. The epoxy wicked its way into the 1 μ m channel structure. Furthermore, MS testing revealed epoxy contamination. In conclusion, the feasibility of TMAH etching for long channel lengths paved the way for a third generation of nozzles with 2.0 mm-long overhangs and 10.0 cm-long T-channels. This third process is described below.

7.5 3rd Generation Nozzle Design and Fabrication

The design of the 3rd generation nozzle included a 2.0 mm long overhang, and a 15 mm separation channel so that separation experiments could be performed. A schematic of the design is shown below (Figure 7-13).

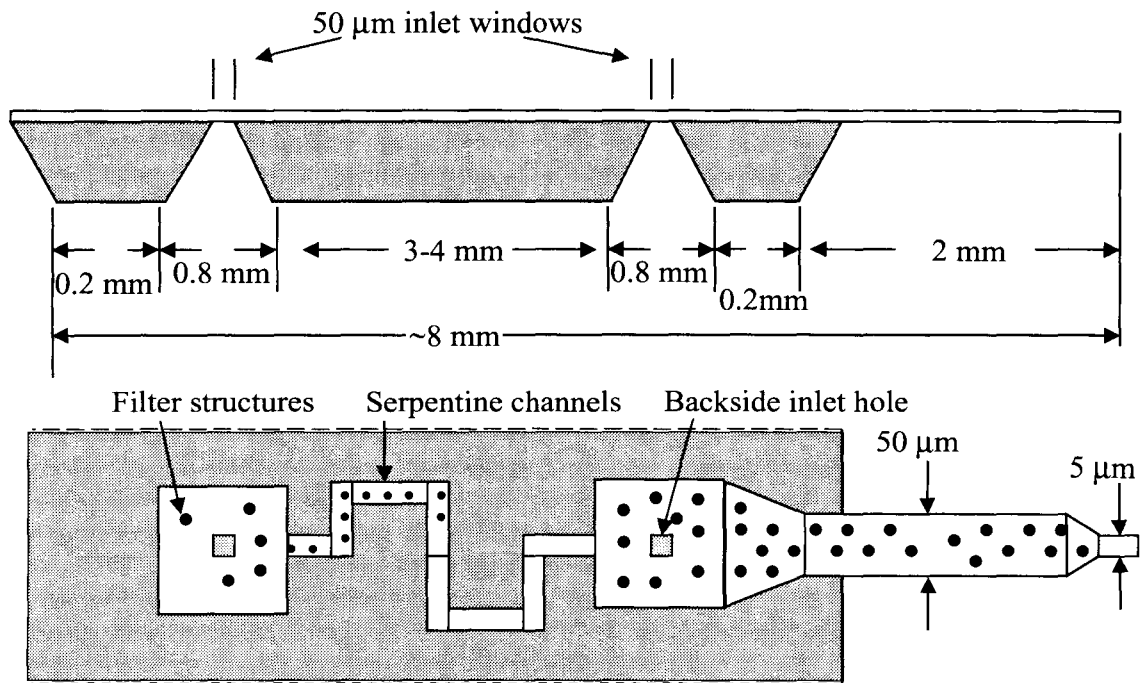


Figure 7-13: 3rd generation MS nozzle with separation channel, 2mm overhang, and additional inlet

As shown, this nozzle version was much more complex – containing an additional inlet for the separation channel. The fabrication process incorporated many of the results learned in the 2nd generation, but because of the massive length of the channels, the etching holes and additional sealing steps had to be included. The spacing between these etch holes was 600 μm requiring a 3 hr TMAH sacrificial etch time. Photographs of the completed structures are shown in Figure 7-14.

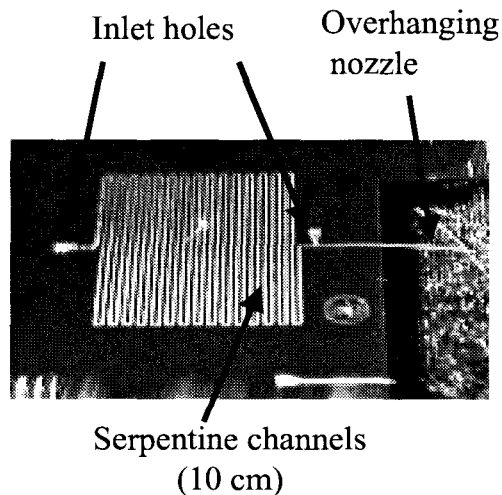


Figure 7-14: Completed 3rd generation structure with freestanding mm-long silicon nitride nozzle.

Although the silicon nitride sacrificial polysilicon process demonstrated free standing mm-long freestanding structures, this type of process required very good control of LPCVD thin film stress. Because of such long freestanding structures, any stress gradients between the various silicon nitride depositions produced curling and bowing of nozzle. A wonderful example (unfortunately) of how these stress gradients (typically 200MPa for LPCVD Si_xN_y) can affect the geometry of the structure has been photographed below (Figure 7-15).

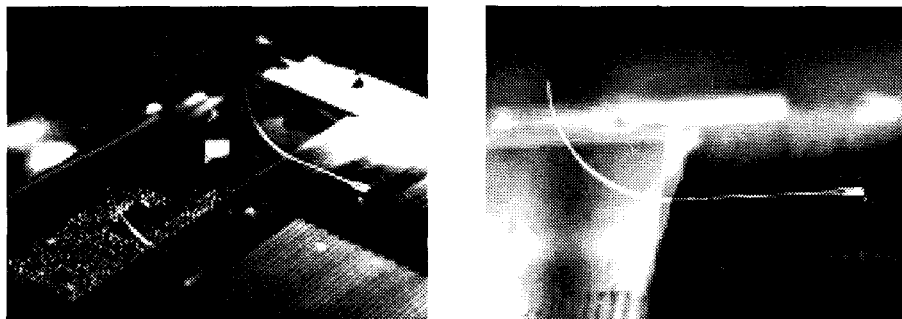


Figure 7-15: Upward curling of nozzle structures due to stress gradients in silicon nitride.

To achieve channels longer than a few hundred microns long, etching and sealing of holes on Si_xN_y channels had to be performed after sacrificial layer etching. These etch holes not only complicated the process, but the resulting stress concentration around the etching holes caused the released microchannels to crack as shown in Figure 7-16. Cracking of the channel was thought to be due to the release of built-up stress during the

sacrificial layer etch [6]. The crack is generally initiated at or near an a stress concentration.

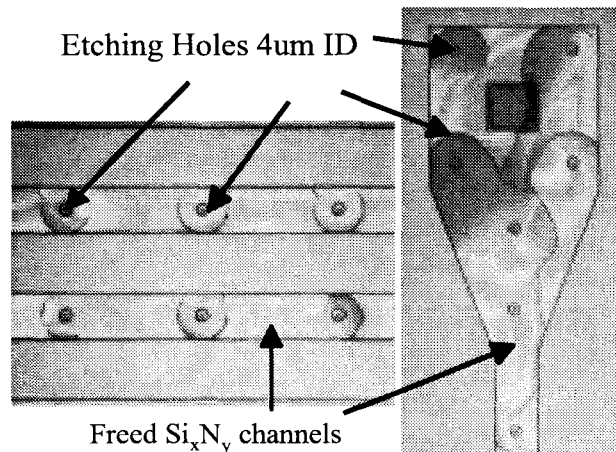


Figure 7-16: Cracking due to stress in Si_xN_y micro-channels after sacrificial layer etch (same chip as in previous figure).

Although several methods such as filleting and posts do improve yields, this type of process is contingent upon the thin film deposited stress. Stress measurement of silicon nitride LPCVD was performed on wafers with $0.7\mu\text{m} - 1.0\mu\text{m}$ silicon nitride, a Cannon Flatness Gauge, and the Stoney [7] formula. The nitride stress for one deposition was $\sim 300\text{MPa}$. 100 to 200MPa is typically acceptable for most MEMS structures, but in our case, because of the extremely long freestanding length and the number of silicon nitride depositions, this stress level proved to be disastrous. Furthermore, although we have demonstrated that ESI can be performed successfully with silicon nitride structures, their practicality was very questionable. The fragile silicon nitride capillaries shattered with the slightest contact with mass spectrometer inlet during handling. What was desired, then, was another type of MEMS nozzle material that could be fabricated into a similar nozzle type structure, but without the drawbacks of this complex surface micromachined process.

7.6 Taylor Cone Visualization

The ability to fabricate precise micrometer-sized tip geometries introduces further opportunities to examine micro-electrospray phenomena. Flow visualization experiments were conducted for two purposes: 1) to confirm proper operation of the micro-channels

and the ESI at the tip and 2) to investigate the Taylor Cone properties at the tip. In fact, current literature lacks adequate flow visualization of this phenomenon especially at the micron scale. Photographing a clear fluid droplet that is only $10\mu\text{m}$ in size becomes very difficult due to lack of adequate light into the microscope objective, depth of field, and the transparent nature of the liquid. The nm-sized fluid stream of droplets emanating from the cone are virtually impossible to observe with conventional methods. Attempts were made with fluorescein, a fluorescent dye, and a red laser but without success. Nonetheless, visualization of the $10\mu\text{m}$ cone on Parylene tip showed that, indeed, the droplet base dimension could be controlled by the nozzle orifice size and was stable over a wide range of distances and sample conditions. The imaging done, here, was done using novel polymer nozzles using Parylene technology developed by Wang *et al.* [8]. More details on this technology can be found in Wang's thesis [9].

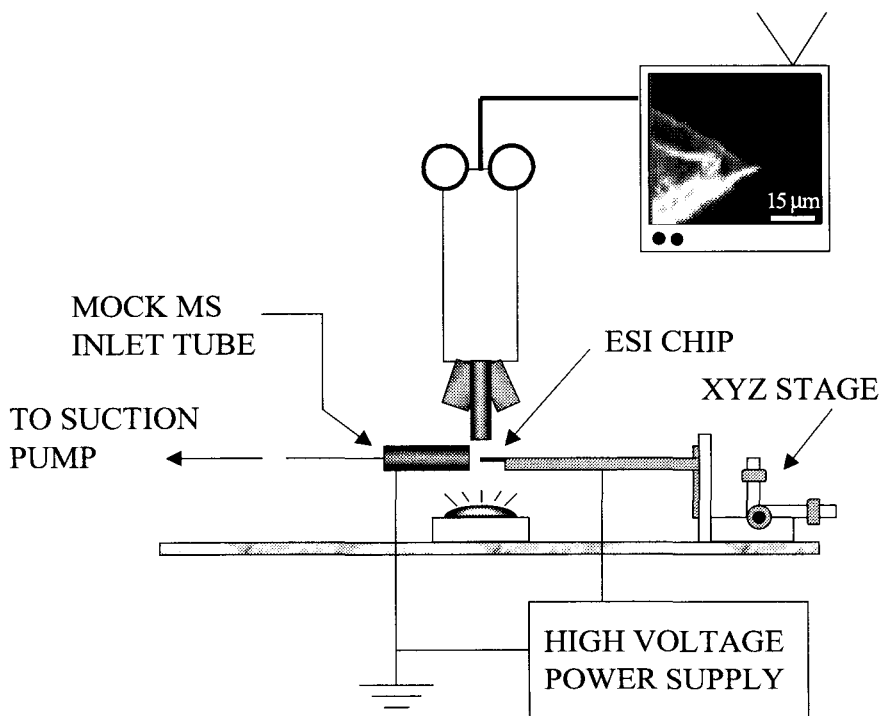


Figure 7-17: Taylor Cone visualization set-up.

The visualization was done with a standard video camera connected to a Microzoom probestation microscope. To simulate conditions similar to the inlet of a real mass spectrometer, an actual MS inlet tube was utilized. However, instead of ion focusing lenses and high vacuum, the other end of the tube, as shown in Figure 7-17, was

connected to a simple suction pump. The suction pump was needed to ensure that excess sample would not collect on the MS inlet tube and short out the power supply. The cone was observed with and without the suction pump on to make sure that the air flow was not creating a “fake” Taylor Cone effect. With the MS inlet tube at ground potential, the MEMS ESI chip was mounted in a custom Plexiglas chip holder which eliminated the tedious backside gluing required to connect the previous MEMS ESI chips to the “macro” world. Figure 7-18 shows the 3 x 3cm Plexiglas jig which allows multiple chips to be tested without the typical epoxy connection. The seal is made by tiny O-rings which are just slightly larger than the backside inlet holes on the ESI chip.

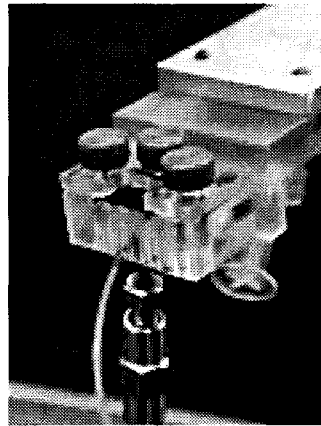
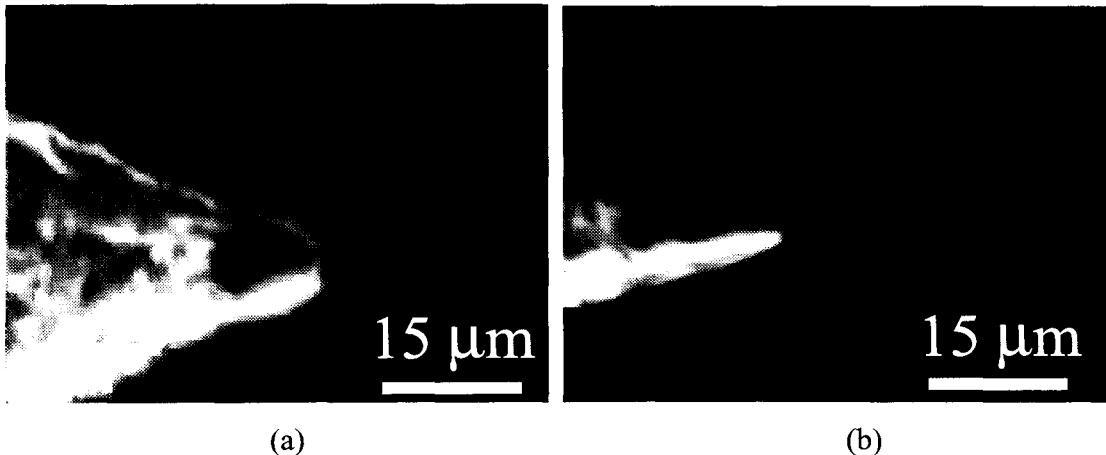


Figure 7-18: Chip holder connected to XYZ stage for ESI visualization.



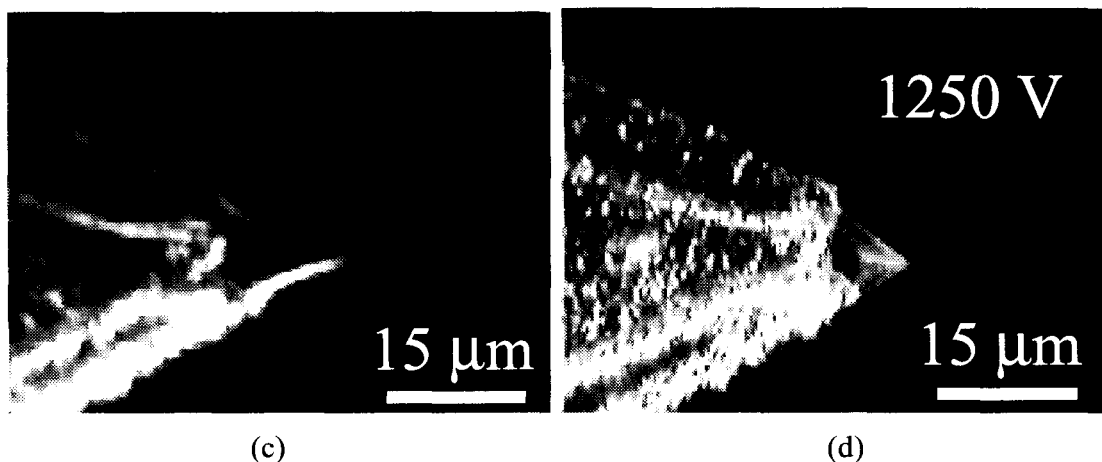


Figure 7-19: Video snapshots of formation of Taylor Cone on microcapillary as voltage is increased from 800 V to 1250 V (alphabetical order).

With a high magnification lens (Leica 1000x), the Taylor Cone formation at the orifice of the polymer micro-capillaries was video taped. The test solution consisted of 1% acetic acid (by volume) added to 1:1 MeOH:Water. The sequence of snapshots above clearly indicates how the base size of the Taylor Cone is governed by the Parylene tip orifice geometry, and the formation of the cone is governed by electrical potential. Although there was no wetting of the Parylene surface behind the outlet, the outer periphery of the nozzle does wet. This is good news because with micromachining this wall thickness can be thinned down even further. Figure 7-19 shows four different freeze frame shots of the creation of the Taylor Cone as the electrical potential is increased from 500V to 1250V. The Parylene surface looks rough because of the silicon roughening step early in the fabrication process, but the internal channel walls are quite smooth. In frames (a) and (b), we note that although the electric field was applied, the meniscus forces were strong enough to create the curvature. Subsequently, as the potential was increased to 1250V, a sharp and stable cone appeared (Figure 7-19 (d)). The distance from the tip to the inlet was roughly 500 μm . No plume was visible from the point of the cone, because droplet size was likely to be below 100nm as discussed in Chapter 5. It is also important to note that the view of the ESI was taken from a top view through a microscope, and that the “cone” is not circular but flattened in the vertical dimension because the tip orifice is rectangular. In fact, the cone size and shape are also related to flow rate and the distance between the tip and MS inlet. Furthermore, initial measurements of the cone angle show

significant deviation from the 49° Taylor Cone (Figure 7-19, (d)) from that derived in the previous chapter.

7.7 Electrostatic Simulation

In Chapter 6, electrical field simulations showed the benefits of extending the tip and reducing the silicon sidewall profile. With the new Parylene technology [10], structures on other non-conductive substrates like glass or plastic also become feasible. To insulate the silicon substrate from the sample fluid in the current design is difficult due to the large backside silicon wall area, which has to be insulated without any pinholes. In any case, this task of isolating the substrate becomes feasible as micromachinists expand beyond the standard silicon substrates to glass and plastic substrates.

As before, simulations were done using the 2-D MAXWELL electrostatic simulator. The conductivity of the fluid was assumed to be 5 S/m at a potential of 1000V. In this case, however, the silicon substrate was left electrically floating (i.e., completely insulated from the charged sample fluid). The improvements are compared in Table 7-2 below and contour plots of the new simulations are shown in Figures 7-20, 7-21, and 7-22.

Table 7-2: Electric field concentration at the nozzle tip for various overhang profiles

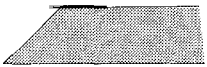
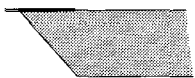
	Structure description (overhang length)	Schematic	Tip electric field (V/m)	
			<i>Non-insulated</i> (Si & fluid at 1KV)	<i>Insulated</i> (fluid at 1KV)
1.	Short-slant-forward (30 μ m)		2×10^6	4×10^6
2.	Short-slant-back (30 μ m) (proposed 2 nd generation)		4×10^6	7×10^6
3.	Long (1.5mm)		5×10^6	9×10^6



Figure 7-20: Type 1 - Si insulated, maximum field concentration, 4×10^6 V/m



Figure 7-21: Type 2 - Short-slant-back, maximum field concentration, 7×10^6 V/m

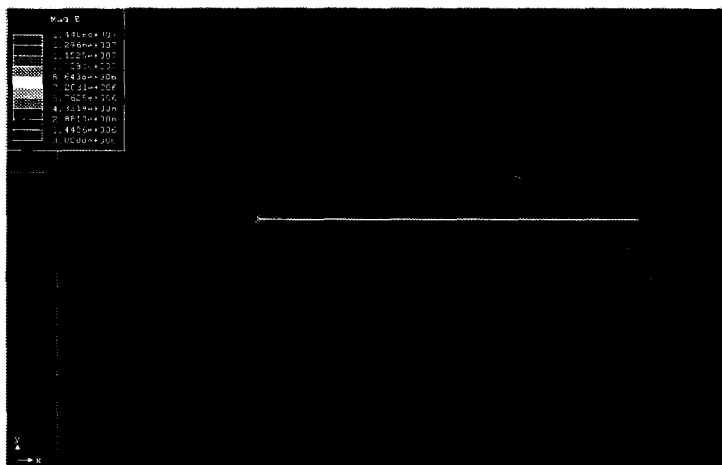


Figure 7-22: Type 3 - Short-slant-forward, maximum field concentration, 9×10^6 V/m

7.8 Conclusion

To sum up, a new area of MEMS applications has been investigated. The feasibility of MEMS devices for MS ESI interface has been demonstrated by repeatable MS scans of Gramicidin S. A MEMS overhanging nozzle structure has been developed using typical semiconductor fabrication steps, and multiple methods of fabricating *mm-long* surface micromachined structures have been studied. The advantages of polysilicon sacrificial layer technology for mm-long structures has been demonstrated. Two methods of designing micro-channel post-filter structures were utilized and three generations of the basic nozzle design were systematically fabricated; each new run incorporated knowledge gained from the previous generations' experiments. In addition, fluid visualization of the Taylor Cone formation from our tips unearthed new issues in the study of electrospray phenomena. Furthermore, the complex integration of backside grooves and frontside cavities with the silicon nitride overhanging structures demonstrated (with low yields) the viability of this process in an academic laboratory. Certainly better results could be achieved in an industrial VLSI facility where tight process control over thin film stress and etch uniformity are the norm.

References

1. O. Tabata, H. Funabashi, K. Shimaoka, R. Asahi, and S. Sugiyama, "Surface Micromachining using Polysilicon Sacrificial Layer," Proceedings of International Symposium on Micromachine and Human Science, pp. 163-172, Nagoya, Japan, Oct. 1991.
2. O. Tabata, R. Asahi, H. Funabashi, K. Shimaoka, and S. Sugiyama, "Anisotropic Etching of Silicon in TMAH Solutions," Sensors and Actuators (A:Physical), Vol. 34, pp. 51-57, 1992.
3. L.V. Ngo, P. Nelson, and C.J. Kim, "Surface-Micromachined Beams Without Spring Effect of Anchor Step-up," Technical Digest, Solid State Sensor and Actuator Workshop (Hilton Head '96), pp.140-143, Hilton Head Island, South Carolina, USA, June 1996.
4. X. Yang and Y.C. Tai, "Improved Boundary Conditions of Surface Micromachined Diaphragms," Micromachining Workshop III, Southern California Chapter of American Vacuum Society, Anaheim, California, USA, Sep. 1996.
5. Ansoft Corp., PA, USA.
6. Xing Yang, *Micromachined Silicone Rubber Valves for Fluidic Applications*, Ph.D. Thesis, California Institute of Technology, 1999.
- 7 Nancy A. Winfree, Wen H. Hsieh, Ren Wu, and Yu-Chong Tai, "The Effects of Boundary Conditions on Implementing the Stoney Formula for Stress Measurements." TRANSDUCERS '93 The 7th International Conference on Solid-State Sensors and Actuators, 1993.
8. X.Q. Wang, Q. Lin, and Y.C Tai. "A Parylene Micro Check Valve." The Twelfth Annual International Workshop on Micro Electro Mechanical Systems (MEMS '99), Jan 1999.
9. Xuan-Qi Wang, Ph.D. dissertation, California Institute of Technology, 2000.
10. X. Q. Wang, A. Desai, and Y. C. Tai, "Polymer Based Electrospray Chips for Mass Spectrometry." The Twelfth Annual International Workshop on Micro Electro Mechanical Systems (MEMS '99), Jan 1999.

Chapter 8

Fast Mixers for Reaction Kinetics

8.1 Introduction

Fluidic mixing has become an important issue in the study of microfluidic devices and their applications. The length scales (for liquids) in micromachined devices range from 10 to 1000 μm and the fluid flows associated with them are typically below Reynolds number of 2000. Consequently, MEMS devices such as polymerase chain reaction (PCR) chips [1], DNA detection chips [2], and other chip-based biochemical protocols all involve and depend on mixing. Therefore, to speed up and optimize many of these processes, understanding and developing ways of measuring micro-mixing at MEMS length scales is vital.

The impetus for these fast mixers has also been the area of liquid-phase reaction kinetics, where much of the chemistry occurs in sub-millisecond time-scales. For example, many biological processes such as cell activation, enzyme reactions, and protein folding demand sub-millisecond analysis if one wants to investigate intermediate states formed during the reaction. These biochemical processes inevitably involve mixing of certain reactants (i.e., A and B) to initiate the reaction. The schematic below depicts a practical means of investigating intermediate states of a fast liquid-phase reaction. The lines represent fluid channels and the “M” represent mixing points. As an example, assume A and B react to form product C.

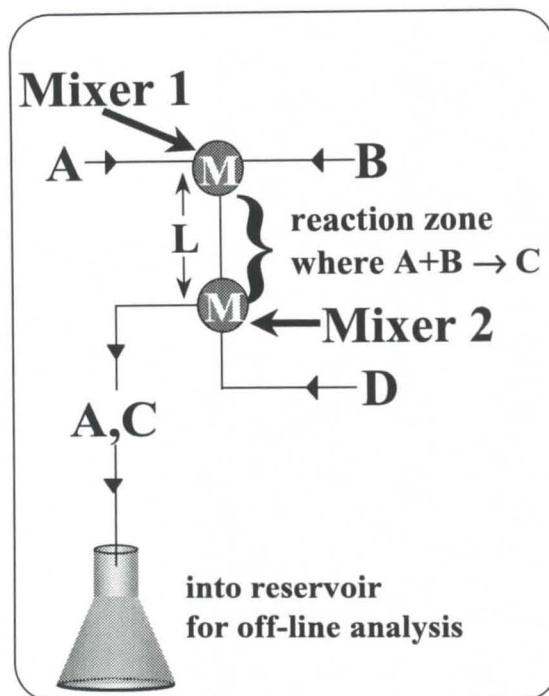


Figure 8-1: Mixer schematic

We would like to be able to *instantaneously* mix liquids A and B together at mixer 1, control the reaction time by varying the delay (the traveling time between two mixers), and then again be able to *instantaneously* mix D, a reaction inhibitor, at mixer (Figure 8-1). The collected products can then be collected continuously with a desired volume. The ability to perform this series of high speed mixing steps, therefore, is crucial to the study of chemical reactions which can be analyzed in this fashion. Practically, it is crucial to have fast mixers (short mixing time) and short delay (reaction) time if the reaction is fast. The mixing time must also be reasonably shorter than the intended reaction time.

8.2 Past Mixers

Commercial machines capable of performing this series of fast mixing steps are available today but are limited in several ways. For example, the best available in the market, the BioLogic SFM4/Q Quenchflow, uses series of Berger ball mixers [3]. These larger ball mixers (1 in x ½ in x ½ in), however, only allow reaction delay times as short as 3 ms. Any significant delay shorter than 3 ms cannot be studied using these ball mixers because the mixers are not integrated, but rather composed of two separate units assembled

together. Figure 8-2 shows the internal cross section of this mixer, which works by employing the turbulent wake behind the sphere. A picture of this common phenomenon is depicted in a wind tunnel experiment in Figure 8-3.

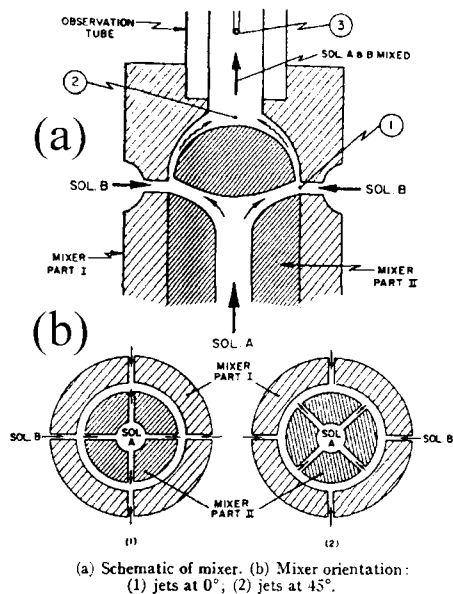


Figure 8-2: Schematic of the Berger Ball mixer developed in 1968 still used today.

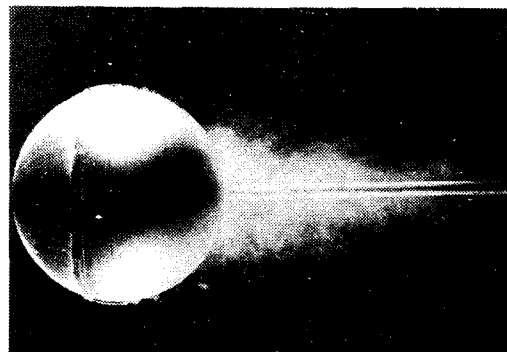


Figure 8-3: Turbulent wake behind a sphere [4].

In the field of biochemistry, although chemists like Moskowitz [5] and Takahashi [6] have demonstrated μs mixing using multicapillaries and free jet mixing respectively, these methods have very limited use because a second quench cannot be performed after the first jet mixing. A second quench or subsequent mixing steps is key to stopping the reaction and thus “freezing” the chemical state of the reactants in time. Table 8-1 summarizes designs of previous liquid mixers and their shortcomings.

Table 8-1: Brief overview of liquid mixers

Date	Author	Technique	Mixing time	Problem
1966	Moskowitz <i>et al.</i>	Multi-capillary	$\sim 30\mu\text{s}$	Quench step not possible
1968	Berger <i>et al.</i>	Turbulent wake	$\sim 200\mu\text{s}$	Delay time 3+ms
1993	Miyake <i>et al.</i> [7]	Micro-nozzles	$\sim 1\text{s}$	Mixing not fast enough
1995	Takahashi <i>et al.</i>	Free jet	$\sim 20\mu\text{s}$	Quench step not possible
1997	This work	Turbulent flow	$\sim 50\mu\text{s}$	-
1998	Knight <i>et al.</i> [8]	Fluid dynamic focusing	$\sim 5\mu\text{s}$	Single mixing stage, no offline analysis

With micromachining, short delay length is obviously available and, more importantly, several mixers can be integrated on one chip and several mixing events in series or parallel can be initiated. Decreasing the reaction volume and the distances between the mixing chambers combined with high flow velocities enabled us to achieve greatly reduced dead times as well as large volumes of samples for examination with continuous operation.

8.3 Design, Fabrication, and Experiments

Although the mixing of fluids is fundamentally governed by molecular diffusion, turbulence in the flow can enhance mixing by many orders of magnitude [9]. It is well known that turbulence in the flow field ($Re > 2000$) will increase reactant area and reduce reaction times. Accordingly, we designed our mixers to be used in the high Reynolds number regime to minimize mixing time.

The design of the mixing chip was similar to the schematic shown previously. The semi-vertical and rough profile of anisotropically etched $\langle 110 \rangle$ Si wafers was used to create channels through which high speed fluids could be injected. $\langle 110 \rangle$ orientation silicon wafers were chosen instead of the common $\langle 100 \rangle$ ones for two reasons: 1) to have a “rectangular” reaction zone channel cross section rather than the characteristic 54.7° trapezoid and 2) to be able control the etching dimensions in convex corners (at every

turn in the channel). Knowing the dimensions of the delay channel was key to determination of reaction products, and thus, key to mixer calibration. Consequently, most recent generations of the chip designs were fabricated using the Deep Reactive Ion Etching (DRIE) technique [10]. With DRIE channel geometries could be better controlled and features were limited to being aligned with the Si etch planes. We fabricated “T” mixers with various delay lengths per chip (Table 8-2). The silicon mixer (Figure 8-4) was fabricated using <110> Si wafers, KOH etching, and anodic glass bonding [11]. Using thermal oxide as a mask, the mixer channels, 150 μ m deep and 408 μ m wide, were etched in 70°C KOH for 2.2 hrs. An exit hole (750 μ m diameter) was drilled into the silicon chip before anodically bonding [12] the Pyrex 7740 glass, which also had three similarly sized machine drilled holes(750 μ m). The anodic bonding process is detailed in the Appendix. 1cm x 1cm mixer chips with delay lengths of 5.33 mm, and 20.33 mm, respectively, without the glass cover are shown below in Figure 8-4.

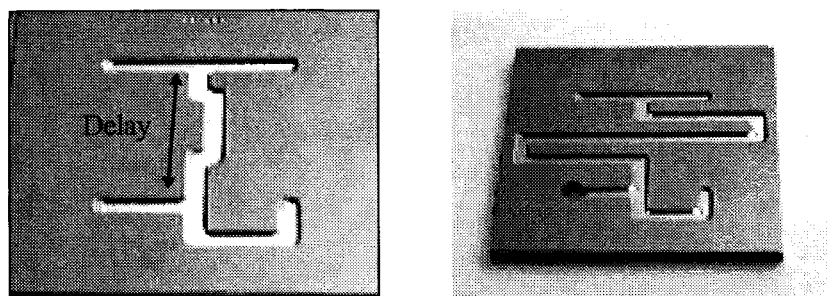


Figure 8-4: Two mixers with delay lengths of 5.33mm(L) and 20.33mm(R).

Table 8-2: Fabricated mixer delay lengths and their respective volumes

	Delay Length (mm)	Delay Volume (μL)	
	2.66	0.27	
	5.33	0.53	
	10.66	1.0	
	21.33	1.97	

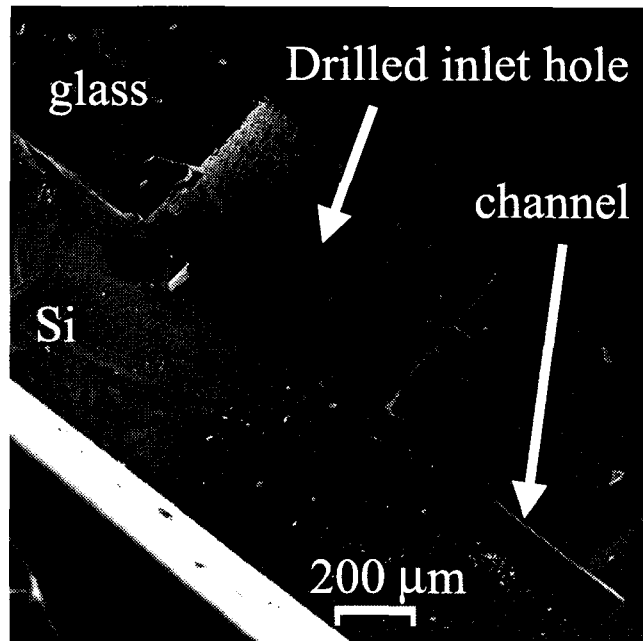


Figure 8-5: Cleaved chip showing the seamless glass-Si anodic bond.

The chip and a holder was designed so that they could be exactly substituted for the ball mixer provided with a commercial quenched flow apparatus, BioLogic SFM4/Q (Figure 8-6) [13]. The machine, equipped with 5 and 20mL Kel-F syringes, delay lines from 17 to 190μL and a diverting exit valve could accurately control input flow rates.

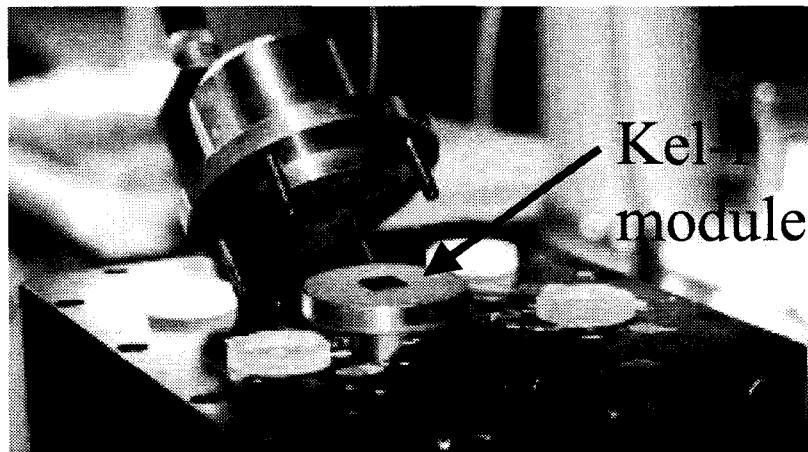


Figure 8-6: Biologic machine with 1cm x 1cm mixer chip before clamping.

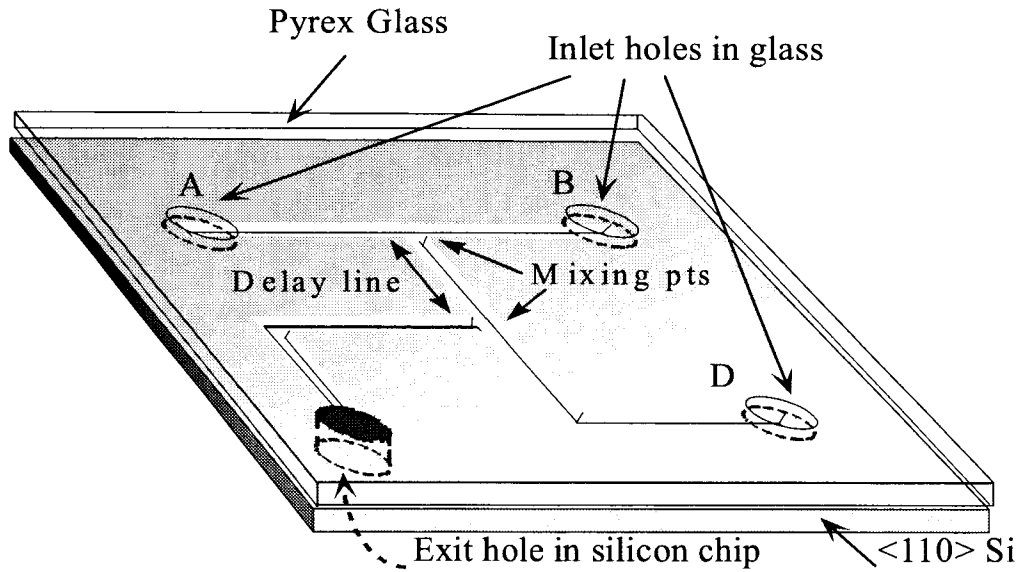


Figure 8-7: 3-D view of fabricated mixer chip

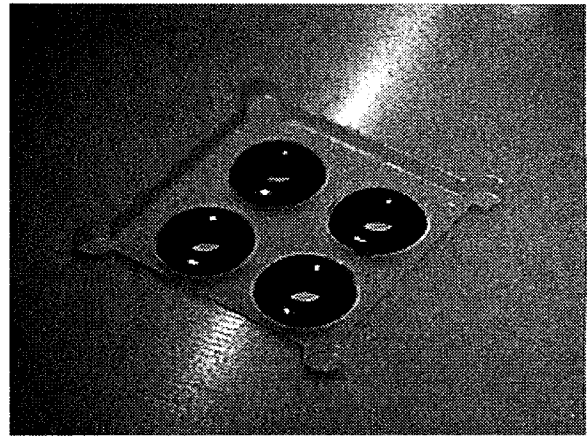
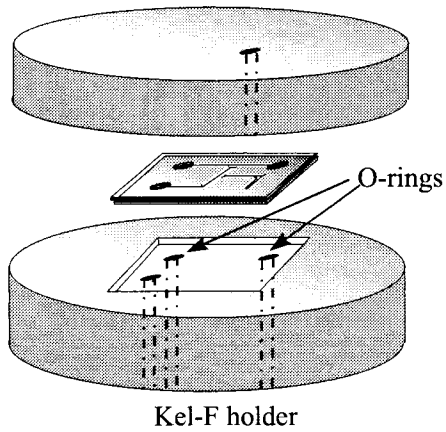


Figure 8-8: Mixer interface to Biologic machine (left) and close-up of chip Kel-f holder (right)

In order to simplify calibration of the mixer, we designed the mixer chip so that it could be substituted for the BioLogic mixer and use the BioLogic machine to accurately control the input flow rates. The chip was interfaced to the Biologic machine using the Kel-F holder and O-rings shown in Figure 8-8. Clamping the two holders together sealed the chip. Fluids at precisely controllable flow rates up to 1.5 ml/s could be injected into the three inlets and ejected from the top. The mechanics of the mixer chip operation are graphically portrayed in Figure 8-7. The two fluids to be mixed were first injected in

ports A and B, and the two mixing steps occurred at the 1st and 2nd mixing point shown. Between these two mixing points, the two fluids were allowed to react in the delay length. Since the dimensions of the channel are known, by controlling the flow rates the reaction time could be controlled. Furthermore, by using a well-calibrated chemical reaction, the actual delay between the two mixing steps could be confirmed.

8.4 Chemical Calibration Method and Theory

The mixer was calibrated with two pseudo 1st order reactions. The first reaction, the hydrolysis of DNPA (2,4 dinitrophenylacetate), is a well studied reaction specifically suitable for fast mixing [14]. Mixer calibration relied on the fact that as the DNPA was hydrolyzed by a base, sodium hydroxide, it was converted into DNP (dinitrophenol) (Eq. 1, & 2).

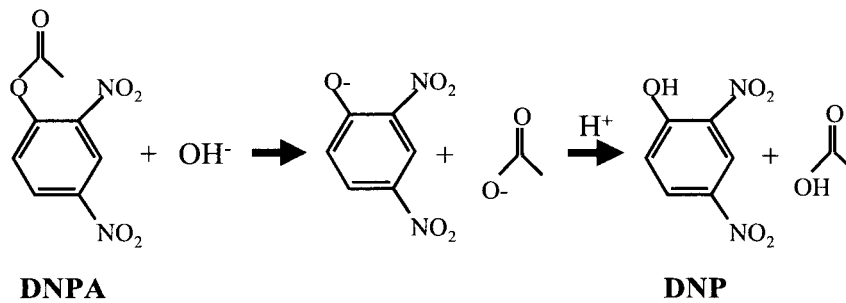
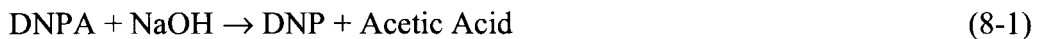


Figure 8-9: DNPA hydrolysis reaction [15]



$$-\frac{dC_{\text{DNPA}}(t)}{dt} \cong k' \cdot C_{\text{DNPA}}(t) \quad (8-2)$$

$$\text{where } k' = k \cdot [\text{OH}^-] \quad (8-3)$$

k is the rate constant of this reaction, and $[\text{OH}^-]$ represents the hydroxide concentration. This reaction is pseudo 1st order with a time constant, $\tau = 1/k'$, if $[\text{DNPA}] \ll [\text{OH}^-]$, i.e.,

$$C_{\text{DNPA}}(t) = C_{\text{DNPA}}(0) \cdot e^{-t/\tau} \quad (8-4)$$

Experimentally, this reaction was quenched at mixer 2 with HCl which neutralized the NaOH. We used mixer chips with different delay lengths to collect fluids with the corresponding reaction times. Then, the UV absorbance of these fluids was measured to determine concentration of unreacted DNPA. This is possible because the reactant, DNPA, and its reacted product, DNP, have different sensitivities at a wavelength of 320 nm. Spectroscopic data were collected using a Shimadzu UV 1601 spectrophotometer with a 16-cell changer. Mathematically, the absorption dependency to concentration of DNPA and DNP can be described in Equation 8-5, where a and b are absorption coefficients of DNPA and DNP respectively.

$$A(t) = a \cdot C_{\text{DNPA}}(t) + b \cdot C_{\text{DNP}}(t) \quad (8-5)$$

Since the chemical reaction is 1 to 1, we also have the following relationship:

$$M - C_{\text{DNPA}}(t) = C_{\text{DNP}}(t) \quad (8-6)$$

where the constant, M , represents the concentration of DNPA at $t=0$ and the concentration of DNP at $t=\infty$. We can also define the following absorbance constants from the equations above:

$$A_0 = a C_{\text{DNPA}}(0) = a M \quad (8-7)$$

$$A_\infty = b C_{\text{DNP}}(\infty) = b M \quad (8-8)$$

Combining the two equations (Equation 8-7 and 8-8) and two unknowns, we arrive at the relationship between concentration and absorbance.

$$\frac{C_{\text{DNPA}}(t)}{C_{\text{DNP}}(0)} = \frac{A_\infty - A_t}{A_\infty - A_0} \quad (8-9)$$

Substituting Equation 8-9 into Equation 8-4 yields the 1st order exponential function relating absorbance change as the reaction progresses:

$$A_t = (A_0 - A_\infty) \cdot e^{-t/\tau} + A_\infty \quad (8-10)$$

where $\tau = 1/k' = 1/(k [\text{OH}^-])$.

For the DNPA reaction, we have the rate constant to be $56\text{M}^{-1}\text{s}^{-1}$ (at 20°C) and the hydroxide concentration was 2M. With these numbers, the time constant of the reaction was determined to be 0.0089s or $\sim 10\text{ms}$. Therefore, by measuring the absorbance change of the quenched products and calculating the experimentally measured reaction rate constant, we can observe if the mixers were working. Theory predicts that all the experimental data should coalesce together showing the same rate constant even if different chips with different delay lengths and at different flow speeds are used. The linearized expression that the experimental data was compared against is shown below.

$$-\ln\left[\frac{A_\infty - A_t}{A_\infty - A_0}\right] = \frac{t}{\tau} \quad (8-11)$$

8.4.1 Experimental Procedure - DNPA

The experimental protocol involved four major steps – preparation of the base and acid, programming the SFM-4/Q, determining the reaction end points, and collecting the time points from various mixer chips. The strong acid and base solutions were prepared several hours prior to the experiment since time is required for the solutions to re-equilibrate to room temperature. 500mL of 4.5M HCl and 4.0M NaOH were prepared. 10mgs of DNPA was dissolved in 100mL of 2mM HCl and stirred for 1hour. This solution was then filtered through a $0.45\mu\text{M}$ filter. The DNPA solution was finally diluted with more 2mM HCl so that the OD was 1.2. This solution must be used within 3-6 hours. The SFM-4/Q syringes were typically programmed as in Table 8-3. This particular program sequence used a flow rate of 2mL/sec/syringe.

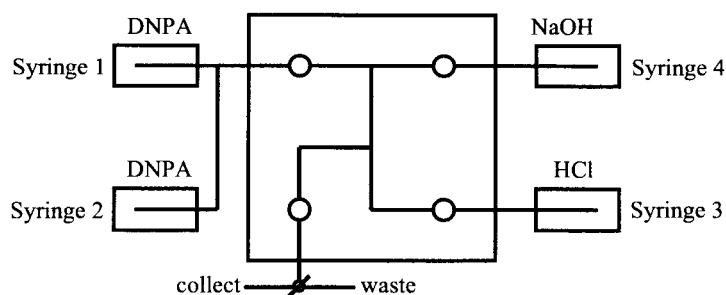


Figure 8-10: BioLogic and chip connection schematic

Table 8-3: Syringe sequence steps for the Biologic quenched flow machine

	Fluid	Step1	Step 2	Step 3
Time (ms)	-	75ms	240ms	100ms
Syringe 1 (μL)	DNPA	150 μL	0	
Syringe 2 (μL)	DNPA	150 μL	480 μL	0
Syringe 3 (μL)	HCl	150 μL	480 μL	0
Syringe 4 (μL)	NaOH	150 μL	480 μL	0
Valve		Waste	Collect	Waste

Equal volumes of DNPA, HCl, and NaOH were used. Note that Syringe 1 was filled with extra DNPA to fill the lines so that no air bubbles were present. With the commercial mixers, the contents of syringe 3 and 4 were reversed due to the different inlet geometry. The absorbances at the reaction endpoints, t_0 and t_∞ , were determined with the following procedures in Tables 8-4. Finally, using various syringe programs like the one shown previously, many reaction time points were collected. Four experiments were done for each speed (flow rate). Furthermore, to check for problems, end points were re-determined using the procedure shown above.

Table 8-4: Absorbance procedure

For t_0, absorbance of each of the following mixtures was measured twice:
1. 480 μ L DNPA, 960 μ L 2mM HCl
2. 480 μ L DNPA, 960 μ L 2mM HCl, 480 μ L 4.5M HCl
3. 1 st mix 480 μ L 4M NaOH and 480 μ L 4.5M HCl, wait 5 min and add 480 μ L DNPA
For t_∞, absorbance of the following mixtures was measured 6 times:
1. 480 μ L NaOH, 480 μ L DNPA, wait 5 min and add 480 μ L 4.5 HCl

8.4.2 DNPA Results

Numerous experiments were done using silicon mixers with reaction delay lengths from 2.66 mm to 20.66 mm and flow rates from 100 μ L/s to 1000 μ L/s. By varying the flow rates of DNPA and NaOH, we were able to collect data of absorbance vs. reaction time. Figure 8-11 shows an example where 2M NaOH was reacted with DNPA for reaction intervals from 3ms to 12ms. This base concentration corresponded to a published rate constant of $56\text{M}^{-1}\text{s}^{-1}$ [14] and a reaction time constant, τ , of 10 ms [14].

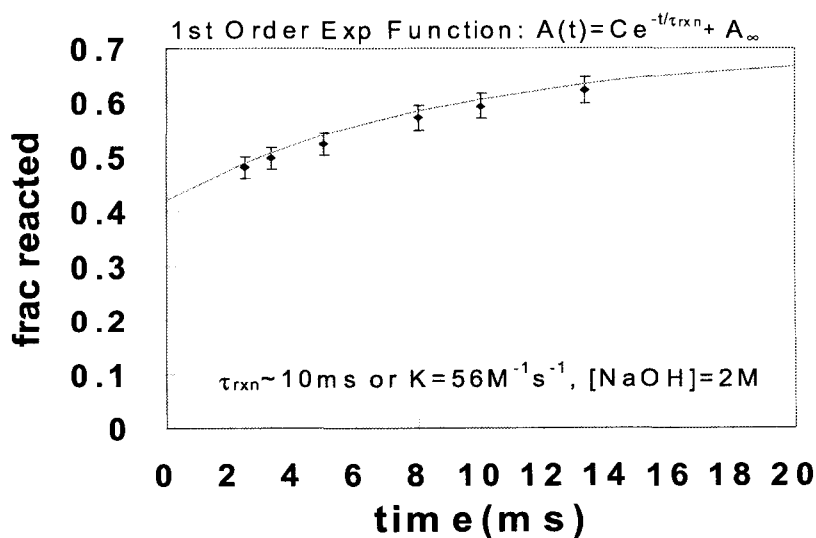


Figure 8-11: DNPA Absorbance vs. Time Plot

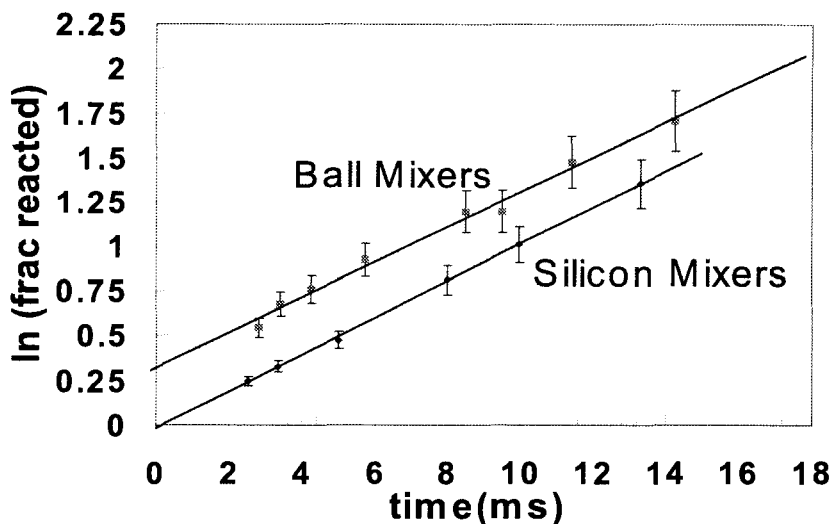


Figure 8-12: Linearized DNPA data

Figure 8-12, then, shows a series of experiments done with both the commercial and silicon mixers for comparison. Linear fits of these experiments produced rate constants of $51\text{M}^{-1}\text{s}^{-1}$ and $46\text{M}^{-1}\text{s}^{-1}$ for the silicon and commercial mixers, respectively, which agreed well with the published figure of $56\text{M}^{-1}\text{s}^{-1}$ for DNPA hydrolysis. The good agreement with the published rate constant illustrated that the reaction delay length on the chip authenticated the 1st order reaction model. This fact was important because it demonstrated mixing time was negligible compared to the reaction delay time. The experimental data also shows a vertical offset in the straight line fit. In the ideal case of instantaneous mixing, the linear fits should intersect the origin. In other words, at time zero there should be no products (no change in $A(t)$). Due to the design of the Berger ball mixers, it is likely that there may be some reaction occurring in the mixer stage itself which causes this upward shift of the data. There was also a similar shift associated with the silicon mixers, but the value was on the order of the experimental error ($\sim\pm 100\mu\text{s}$).

8.4.3 PCA Reaction For Faster Kinetics

As we had designed our mixers to be used in the sub-ms regime, we were unable to utilize the DNPA reaction experiment to investigate shorter delay times. In order to test

8.4.4 Experimental Procedure - PCA

Unlike the established DNPA hydrolysis reaction, the PCA hydrolysis rate constant had to be experimentally determined. The rate constant, $444\text{M}^{-1}\text{s}^{-1}$, fit well with other similar hydrolysis reactions [16]. After the rate constant was determined, only then could we use this to calibrate our mixer chips. Fourteen experiments were conducted and the rate constant, $430 \pm 47.6 \text{ M}^{-1}\text{s}^{-1}$ with a dead time of $120 \mu\text{s} \pm 100\mu\text{s}$ (measured with the silicon mixers (Fig. 8)), agreed quite well with chemical kinetic theory. More importantly, Figure 8-14 revealed the achievement of reaction times as short as $110\mu\text{s}$. Note that the rate constant derived from silicon mixer PCA experiments differ from the commercial mixer by 20% ($362\text{M}^{-1}\text{s}^{-1}$); a similar trend was noted in the DNPA experiments. The commercial mixers consistently seemed to predict a rate constant that was 20% lower from the actual value.

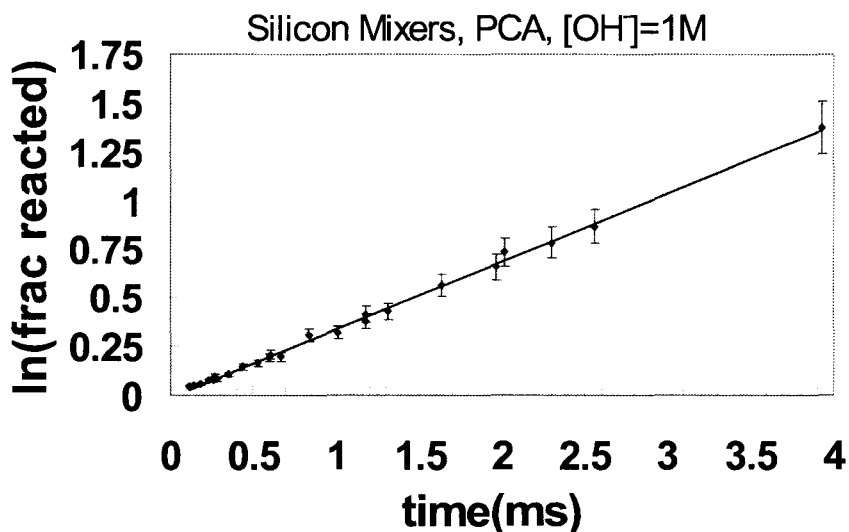


Figure 8-14: Plot of silicon mixers with PCA reaction

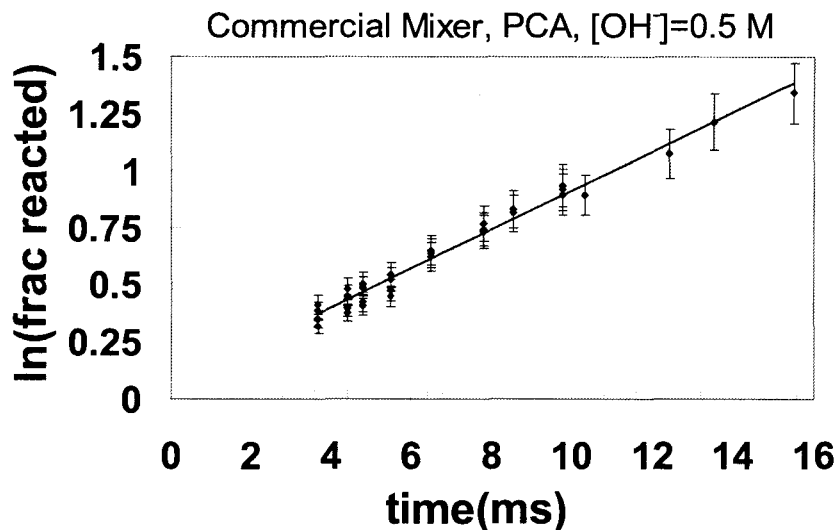


Figure 8-15: Plot of commercial mixers with PCA reaction

It should be emphasized that 10% to 20% error in the experimental data is considered very good in these types of quench flow experiments where there are a number of sources of error such as manual pipetting of collected solution, time delay in measurements, and a shift in NaOH concentrations over time. Nevertheless, one drawback of the PCA reaction is background hydrolysis. The fast PCA reaction was so sensitive that it slowly hydrolyzed by itself. To minimize this background hydrolysis, the PCA solution and its reacted samples used in our experiment are kept chilled in ice, but it may still contribute errors for some of the shortest reaction time points. Overall, though, the silicon mixers have demonstrated a superb performance which was unavailable from the commercial state-of-the-art instrument.

8.5 Flow Visualization

Here, we then report our work on using flow visualization to confirm the performance of our silicon mixers. One primary goal of the visualization was to justify why mixer chips failed below certain flow velocities. Also, we wanted to check for cavitation effects. Fortunately, because of the continuous quench flow mixer configuration in the chip, we were able to visually observe this microsecond mixing without the use of high speed

imaging equipment. In the past, others such as Li [17] and Bourne [18] have performed flow visualization experiments using acid-base indicators and reactions in millimeter (2-5 mm diameter) sized pipes. No other group has used similar techniques on these size scales to date. Consequently, to further correlate some of the mixing trends in our silicon mixers, extensive flow visualization experiments were conducted first by mixing of dyes and then a more sophisticated and accurate method, the color change of an acid-base indicator, bromothymol blue. A new chip holder, similar to the Kel-F one, had to be fabricated so that the whole fluidic pathway could be seen during the experiment. In addition, the mixer chip holes had to be shifted from the glass to the silicon. Figure 8-16 shows the glass-Plexiglas flow visualization jig with PEEK tubes attached at the back. Any leaks could be spotted instantly with the clear material. The PEEK tubes were affixed to the Biologic machine so that the same computer-controlled fluid delivery was possible.

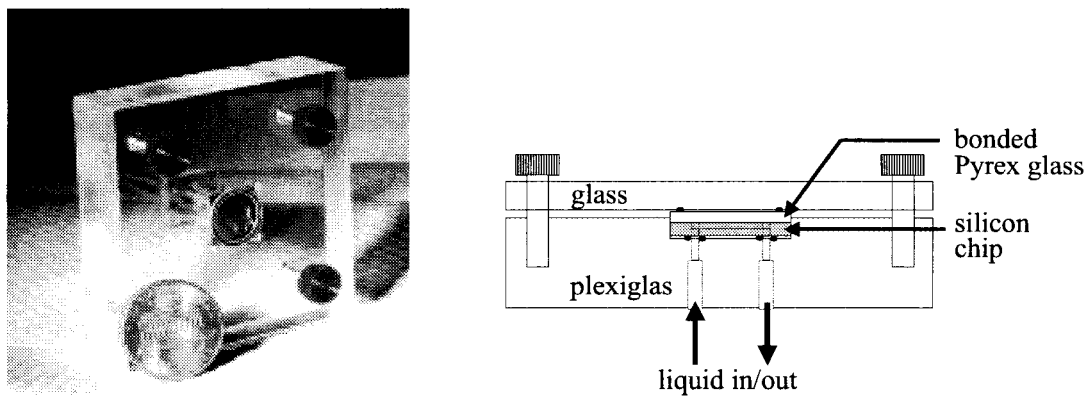


Figure 8-16: Flow visualization jig, cross-sectional view right

At first, dyes (food coloring) were used to observe mixing event, but this technique had many flaws. Figure 8-17 is an example of the dye visualization showing the improved mixing at 1000 $\mu\text{L/s}$ vs. 100 $\mu\text{L/s}$. The images were converted to greyscale to show the interface between the two colored fluid streams. Even with high concentration of different colored dyes, the image intensity was not sufficient. Furthermore, the mixer chip had two mixers, and with this dye technique, only a single mixer could be studied at any time because mixing of more than two dyes resulted in a darkened fluid stream without any discernable interface (greyscale conversion in the picture fails to show this).

To solve these problems and to really observe the two mixers during a chemical reaction, an acid-base indicator technique was employed.

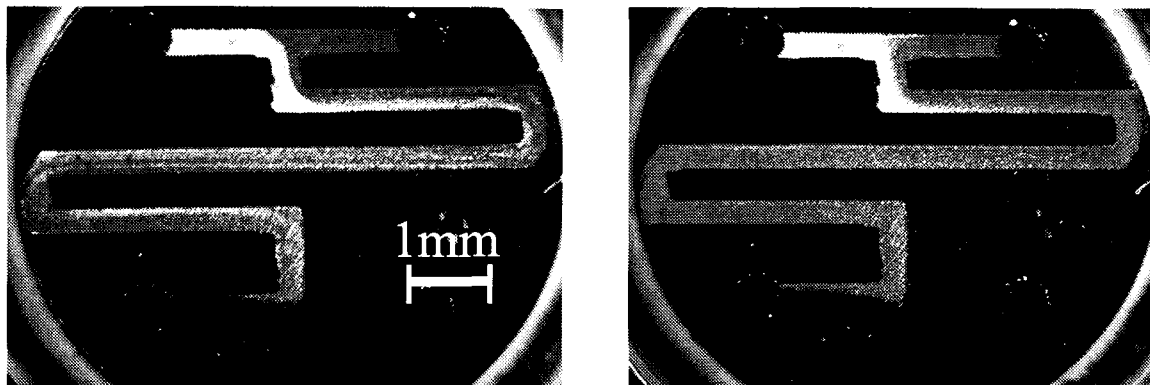
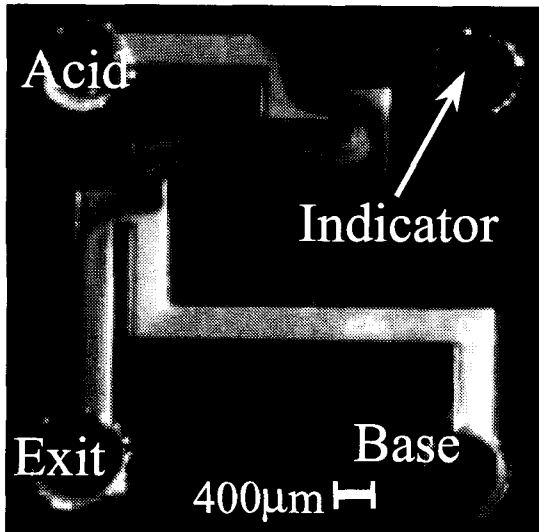


Figure 8-17: Dyes, 100 μ L/s (left) and 1000 μ L/s (right)

Bromothymol blue was determined to be the indicator with the best optical change for both the acid and base mixing step. The indicator worked in the following fashion. Bromothymol blue remained dark green between pH 6.0 - 7.6, but turned yellow in the presence of acid and blue in the presence of base. By injecting acid into inlet A (Figure 8-7), the indicator solution into inlet B, and base into inlet D, three color changes, green to yellow to blue, of the indicator were observed. Photographs of mixer chips with delay lengths of 2.66 mm, 5.33 mm, 10.66 mm, and 20.33 mm while varying flow rates (in the delay channel) from 100 μ L/s to 2000 μ L/s were taken (Figure 8-18). Two significant trends were observed. First, at low flow rates, a clearly visible interface between the two streams could be seen; at higher velocities such a boundary could not be discerned. This observation agreed quite well with chemical reaction calibration data. For example, it was noted that consistent reaction data was produced only at flow rates corresponding to flow rates above \sim 250 μ L/s.

Reynolds No.:500

Reaction time: 2 ms



Reynolds No.:2800

Reaction time: 540 μs

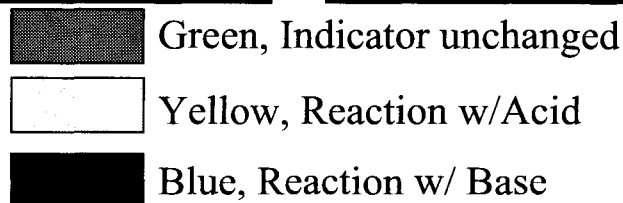
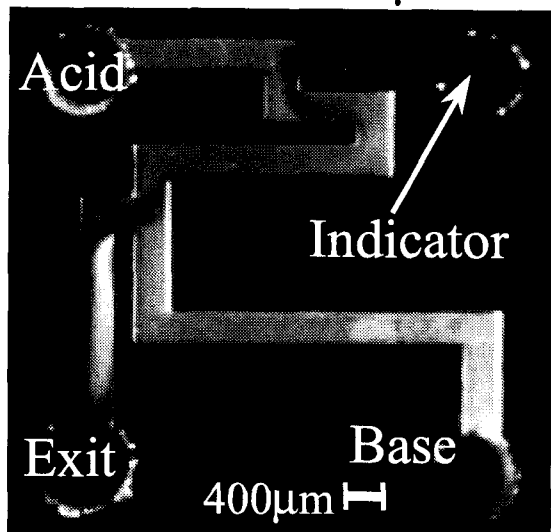


Figure 8-18: Comparison of mixing quality with different flow regimes. (Color plate in Appendix)

Flow rates below this point resulted in scattered data points (data not shown) below the linear fit. Second, the visualization showed that there were finite mixing delays after the first and second mixing points at all flow rates. These mixing distances, in effect, shifted the actual reaction zone without substantially affecting the reaction delay time for the longer delays (Figure 8-19). The photograph below was taken at a flow velocity of $750\mu\text{L/s}$ (Re 2800). An estimation of mixing time from the distance marked below reveals a mixing time of 50 to $100\mu\text{s}$! Otherwise, our chemical calibration could not have been successful.

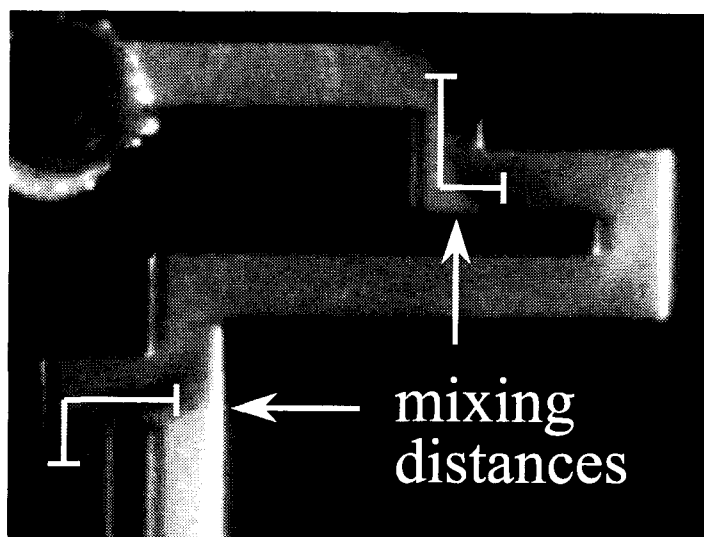


Figure 8-19: Visual estimation of mixing time is 50 to 100 μ s

8.6 Further Optimization of the Mixer Chip

The flow visualization experiments were very useful in identifying which features enhanced mixing, and if those features could be optimized. For example, another series of acid-base indicator experiments were undertaken to examine two mixer chips (with the same reaction delay length) but one with a “straight” path and the other with extra sharp 90° turns. The series of pictures shown on the next page are arranged as follows: the left and the right column show the “straight” (S) and the “extra turn” (ET) mixers, respectively. Three different flow rates (or Reynolds numbers) are depicted from top to bottom in increasing order (200-1666 μ L/s). Comparing the top row, we can see that at this low flow rate both the chips are at the lower end of the mixing envelope. However, the ET mixer at 200 μ L/s is performing better. Unlike the S mixer chip, a solid yellow zone can be seen. As the fluid speeds were increased, the effect of the turns seemed less differentiable; although qualitatively speaking, the ET mixers seemed to show a shorter mixing length. In other words at high speeds (>750 μ L/s), the mixing length remained at a stable minimum, whereas in the “S” mixer chip, this length was still decreasing. Since the turns are simply additional sharp corners, this trend demonstrated validity in adding sharp structures directly into the T-mixing zone to enhance mixing. Two other minor effects that were noted at the high speed range of all the experiments were the evidence

of stagnation or recirculation zone and possible cavitation. The recirculation can be seen in pictures (c) in (Figure 8-21) near the upstream wall at the entrance of the first and second mixer. In the first mixer, a tiny triangular area of yellow and in the second mixer, a similarly shape blue area. Though a minor effect, this could be eliminated by giving the silicon wall in that area a convex curve. Finally, the photographs at high speed suggest that there might be cavitation or creation of very high turbulence because of two observations. First, the appearance of the whitish plume after the second mixer in the blue zone (pictures (c)). Second, while conducting the experiment at this speed, a high pitched noise was also heard consistently when this plume was observed. Further investigation needs to be done to identify the nature of this plume. In any case, a final generation of mixer chips was fabricated incorporating the knowledge from these experiments. An SEM picture of the two types of mixers featuring additional sharp structures at the mixers and outward wall profiles near the stagnation areas are shown in Figure 8-20.

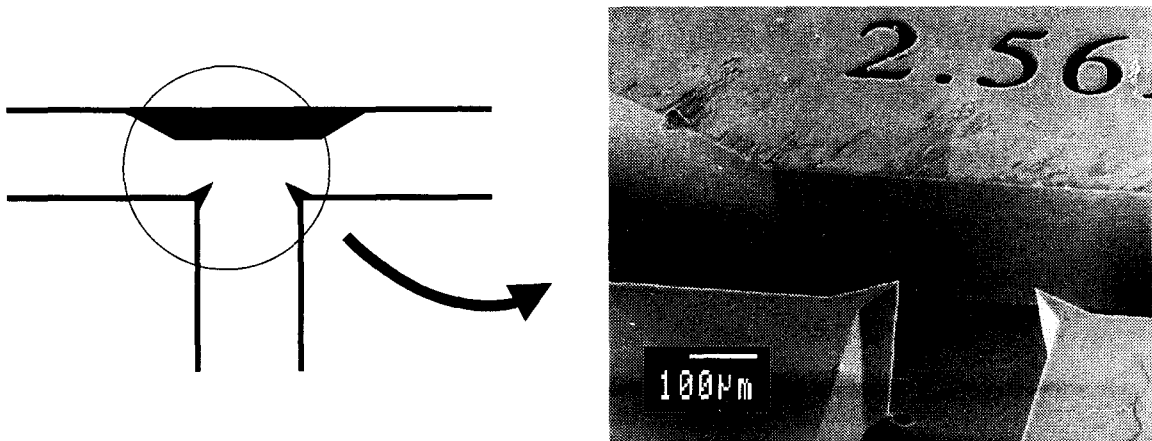


Figure 8-20: Mixer designed with sharp wedges and a convex trapezoid to eliminate the recirculation zone.

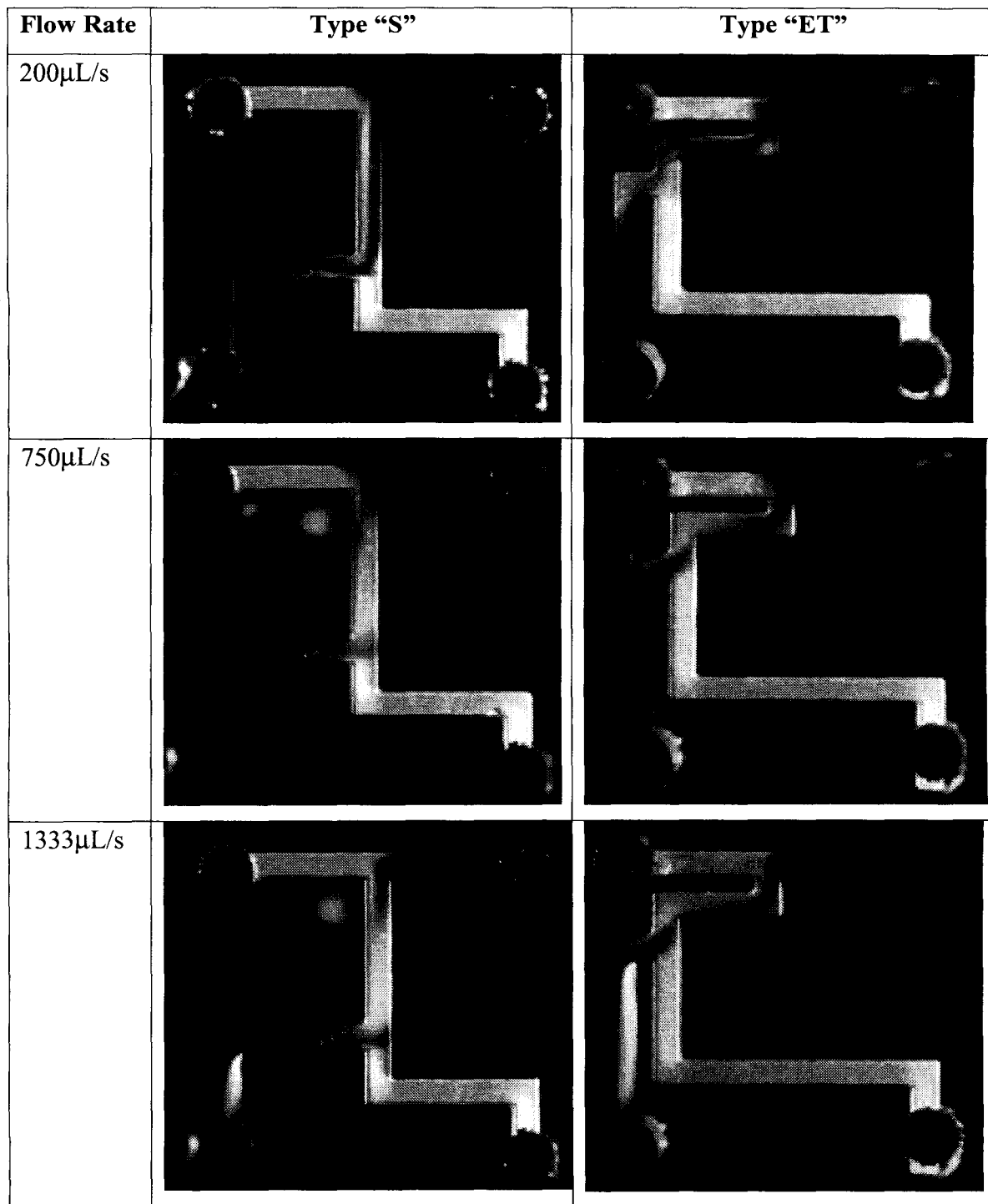


Figure 8-21: Comparison of two mixer chips with identical reaction lengths (2.66mm) at various flow rates. Mixing quality and mixing length decreases with increasing flow rates (top to bottom). Channel width is 400 μ m. (color plate in Appendix)

8.7 Conclusion

As a first demonstration, this project has spawned the fastest sub-millisecond quench flow type mixers available to chemists. In contrast, the best quench flow mixer commercially available today boasts ~ 3 ms as the minimum reaction time. This is a significant leap considering the fact that the best device available today has had little improvement since 1968 [3]. Further optimization of these devices, then, has the possibility of controlling liquid-phase reactions at scales never possible before. Moreover, a chemical reaction technique to calibrate these micromachined mixers has been proven, and verified through flow visualization. This visualization technique can be applied to other MEMS mixers, and reaction times constants can be increased or decreased (by controlling base concentration) depending on the operating regime of the particular device. The design of these mixers allows not only the two mixers shown here but the possibility of studying more complex reactions with multiple reactants mixing at precise intervals.

References

1. M.U. Kopp, M.B. Luechinger, and A. Manz, "Continuous Flow PCR on a Chip," Proc. Micro TAS Workshop, Banff, Canada, Oct. 1998.
2. M. A. Burns, C. H. Mastrangelo, T. s. Sammarco, P.F. Man, J.R. Webster, B.N. Johnson, B. Foerster, D.K. Jones, Y. Fields, A. r. Kaiser, D. T. Burke, "Microfabricated Structures for integrated DNA Analysis," Proc. National Academy of Sciences, USA, vol. 93, pp.5556-5561, 1996.
3. R. L. Berger, Bohdan Balko, and H.F. Chapman, "High Resolution Mixer for the Study of the Kinetics of Rapid Reactions in Solution," Rev. Of Scientific Instr., 1968, V. 39, No. 4.
4. Anderson, John D., *Fundamentals of Aerodynamics*, McGraw Hill Inc., New York, 1991.
5. G.W. Moskowitz and R.L. Bowman, "Multicapillary Mixer of Solutions," Science, 153, 1966, 428.
6. S. Takahashi, Y. Ching, J. Wang and D.L. Rousseau, "Microsecond Generation of Oxygen Bound c Oxidase by Rapid Solution Mixing," J. Of Biological Chemistry, 270,1995, 8405-8407.
7. R. Miyake, T.S. Lammerink, M. Elwenspoek and J. Fluitman, "Micro Mixer with Fast Diffusion," MEMS 1993.
8. Knight JB, Vishwanath A, Brody JP, and Austin RH, "Hydrodynamic focusing on a silicon chip: Mixing nanoliters in microseconds," Physical Review Letters, Vol. 80: (17) 3863-3866 April 27, 1998.
9. L. Forney and G. Gray, Optimum Design of a Tee Mixer for Fast Reactions," AIChE Journal, Nov. 1990, Vol 36.
10. F. Larmer and P. Schilp, "Method of anisotropically etching silicon," German Patent DE 4,241,045, 1994.
11. Y. Kanda, K. Matsuda, C. Murayama and J. Sugaya, "The mechanism of field-assisted silicon-glass bonding," Sensors and Actuators, vols. A21-A23, p. 939, 1990.

12. W. H. Ko, J. T. Suminto, and G. J. Yeh, "Bonding Techniques for Microsensors," *Micromachining and Micropackaging of Transducers*, Elsevier Science Publishers B. V., Amsterdam, 1985.
13. Molecular Kinetics Inc., Pullman, WA.
14. D.J. Cash and G.P. Hess, "Quenched Flow Technique with Plasma Membrane Vesicles: Acetylcholine Receptor-Mediated Transmembrane Ion Flux," *Anal. Biochem.*, 112, 39-51, 1981.
15. Elaine Marzluff, notes 1995.
16. D. Bökenkamp, A. Desai, X. Yang, Y.C. Tai, E. Marzluff, and S. Mayo, "Microfabricated Silicon Mixers for Submillisecond Quench-Flow Analysis," *Anal. Chem.* January 15, 1998, Vol. 70, No. 2, pp. 232-236.
17. K. Li and H. Toor, "Chemical Indicators as Mixing Probes. A Possible Way to Measure Micromixing Simply," *Ind. Eng. Chem. Fundam.* 1986, 25, 719-723.
18. J. Bourne and H. Maire, "Micromixing and Fast Chemical Reactions in Static Mixers," *Chem. Eng. Process.*, 30 (1991) 23-30.
19. A. Desai, D. Bokenkamp, X. Yang, E. Marzluff, Y.C.Tai, and S. Mayo. *Microfluidic Sub-millisecond Mixers for the Study of Chemical Reaction Kinetics*. 1997 International Conference on Solid-State Sensors and Actuators (Transducers '97), May 1997.

Chapter 9

Conclusion and Future Work

As MEMS microfluidic and bio-analysis devices continue to improve, the viability of handheld, automated microsystems for air sampling, and environmental monitoring, become a reality. This thesis has presented specific micromachined solutions in this area -- airborne particle transport, particle collection from air to liquid, an electrospray interface for a mass spectrometer, and creation of fast mixers for study of liquid reactions.

It has been shown that particles of 5-10 μm size range can be efficiently manipulated electrostatically with voltages below 200V in a standard room environment. Because of the interrelationship of the image force, the DEP force, friction, electrode geometry, and particle charge, we see that simulation of all the particle forces is complex. Thus, many of these critical parameters are difficult to measure. In our case, by performing a multitude of experiments designed to isolate and investigate the different types of particle to surface forces, we have determined that particle charging is a significant cause of adhesion on our MEMS transportation system. The work presented here is a catalyst for further research into better stiction free coatings and three-dimensional electrode geometries.

With this knowledge of the transportation characteristics, integration with active filters and liquid interfaces were demonstrated. Two different particle air-to-liquid collection schemes were explored. The first type involved two regimes of voltages and frequencies but failed because the strength of the DEP force was too small to penetrate the liquid meniscus, and because of electrolysis of water on the electrodes. Successful collection was demonstrated through an entirely different type of technique in which the liquid meniscus was moving and not the particles. In addition, a membrane filter structure was integrated with the transportation technology and a new radial design demonstrated

improved collection efficiency. In retrospect, although the solution for transporting particles from air to liquid in a micro-system may not be the most ideal because of complexity of assembly and lifetime issues, the knowledge gained here can be used to develop and understand more about stability of coatings and air-liquid interfaces. In fact, the initial droplet-on-a-capillary experiment shows great promise for the development of analyses and chemistries on arrays of liquid droplets.

Bio-particles in liquid require sensitive detection techniques. One method explored here was an electrospray ionization interface for mass spectrometry. Several generations of silicon nitride ES nozzles were designed, fabricated, and tested. Attempts to further optimize the surface micromachined nozzle process were plagued by silicon nitride thin film stress. It was noted that although feasibility of on-chip ES was validated, different nozzle materials would be required for a more robust device. A next step would be to develop an integrated packed separation column behind the MS nozzle. This would involve study of biocompatible gels and new protocols to enable these gels to be implemented via thin film deposition techniques. For example, column packings that are capable of being spun on and photo-patternable would be key. A move towards glass substrates instead of silicon might enable ESI at lower voltages, and also enable capillary electrophoresis separations on-chip with MS analysis.

Finally, as a first demonstration, this project has spawned the fastest sub-millisecond quench flow type mixers available to chemists. In contrast, the best quench flow mixer commercially available today boasts ~3 ms as the minimum reaction time. Moreover, a chemical reaction technique to calibrate these micromachined mixers has been proven, and verified through flow visualization. This visualization technique can be applied to other MEMS mixers, and reaction time constants can be increased or decreased (by controlling base concentration) depending on the operating regime of the particular device. The design of these mixers allows not only the two mixers shown here but the possibility of studying more complex reactions (protein folding) with multiple reactants mixing at precise intervals.

Without question, the promise of “lab-on-a-chip” has fueled the growth of MEMS microfluidic research. Although much work needs to be done in integration, the fabrication technology developed here paves the way for future research into the world of bio-MEMS.